Master's thesis

NTNU
Norwegian University of Science and Technology
Faculty of Engineering
Department of Marine Technology

Emil Eikrem Rindarøy

Mooring Concepts for Floating Wind Turbines

Numerical Simulations of Innovative Solutions

Master's thesis in Subsea Technology
Supervisor: Kjell Larsen
June 2020

NTNU
Norwegian University of
Science and Technology

Emil Eikrem Rindarøy

Mooring Concepts for Floating Wind Turbines

Numerical Simulations of Innovative Solutions

Master's thesis in Subsea Technology
Supervisor: Kjell Larsen
June 2020

Norwegian University of Science and Technology
Faculty of Engineering
Department of Marine Technology

NTNU
Norwegian University of
Science and Technology

NTNU Trondheim
Norges teknisk-naturvitenskapelige universitet
Institutt for marin teknikk

MASTER THESIS SPRING 2020

for

Stud. tech. Emil Eikrem Rindarøy

Mooring Concepts for Floating Wind Turbines - numerical simulations of innovative solutions

Forankringssystemer for flytende vindturbiner – numeriske beregninger av nye konsepter

Background

In the development of floating wind turbines (FWTs) for utilizing the offshore wind resource, various technologies from the offshore oil and gas (O&G) industry have been adopted, including mooring system solutions. The purpose of the mooring system is to keep the floating wind turbine safely at a required position. It normally consists of three mooring lines of chain. Compared to O&G installations, FWTs tend to be significantly smaller. The external loads are characterized with large mean loads (due to the rotor thrust) in moderate wave conditions and high wave motions in extreme wave conditions.

The importance of the mooring system for a floating wind turbine is crucial. The moorings must be reliable enough to prevent any free drift where cable rupture and collisions are typical consequences and the cost of mooring must be as low as possible in order to make such developments profitable. Optimization of the mooring system is therefore an important task. The industry is currently evaluating new concepts based on the use of synthetic fiber ropes.

The overall objective of this thesis is to learn about floating wind turbines and mooring system design. This includes mooring system concepts and building blocks as well as design methods and requirements stated in rules and regulations.

Scope of Work

1) Review relevant literature and give an overview of state-of-art of floating wind turbines. Describe present state-of-art mooring system for the FWT “Hywind” concept. Focus on station keeping principles and main hardware components.

2) Describe the mechanical behavior and available models for tension-elongation of synthetic mooring materials.

3) Give an overview of the design limit states for mooring systems of floating wind turbines with corresponding acceptance criteria outlined in the recent updates of rules and regulations (use DNVGL-ST-0119).

4) Describe the time-domain analysis methods for mooring systems and how extreme wind turbine motions and line tension can be estimated. Theory to be based on the SIMO/SIMA software suite and respective theory and user manuals.

5) Familiarize with and improve an existing, simplified SIMA model of a CSC 10MW FWT, with the objective of performing numerical time-domain simulations of wind turbine motions and mooring line tensions. Include a mooring system relevant for a FWT on "Hywind Tampen" and perform pull-out and decay tests do document the dynamic system. Numerical simulations to document the ULS compliance of the selected "Hywind Tampen" mooring system shall also be included.

6) Assess if the selected mooring system can be improved by use of synthetic components and/or clump weight and buoys. In particular, an assessment of "low-stiffness" synthetic ropes for a typical taut mooring concept shall be documented. The extent of this activity to be agreed with supervisor.

7) Conclusions and recommendations for further work.

General information

All necessary input data for the simulation case is assumed to be provided by NTNU/Equinor. The work scope may prove to be larger than initially anticipated. Subject to approval from the supervisor, topics may be reduced in extent.
In the thesis report, the candidate shall present his personal contribution to the resolution of problems within the scope of work.
Theories and conclusions should be based on mathematical derivations and/or logic reasoning identifying the various steps in the deduction.
The candidate should utilise the existing possibilities for obtaining relevant literature.

Report/Delivery
The thesis report should be organised in a rational manner to give a clear exposition of results, assessments, and conclusions. The text should be brief and to the point, with a clear language. Telegraphic language should be avoided.

The report shall be written in English and edited as a research report including literature survey, description of relevant mathematical models together with numerical simulation results, discussion, conclusions and proposal for further work. List of symbols and acronyms, references and (optional) appendices shall also be included. All figures, tables and equations shall be numerated.

The original contribution of the candidate and material taken from other sources shall be clearly defined. Work from other sources shall be properly referenced using an acknowledged referencing system.

The report shall be submitted in Inspera, as specified by the department of Marine Technology. In addition, an electronic copy (pdf) to be sent to the supervisor.

Ownership
NTNU has according to the present rules the ownership of the thesis results. Any use of the thesis results has to be approved by NTNU (or external partner when this applies). The department has the right to use the results as if the work was carried out by a NTNU employee, if nothing else has been agreed in advance.

Thesis supervisor**:**
Prof. II Kjell Larsen, NTNU/Equinor

Deadline: June 10th, 2020

Trondheim, January 31st, 2020

Kjell Larsen (sign)

Emil Eikrem Rindarøy (sign)

Preface

This Master's Thesis concludes my master's degree in Marine Subsea Technology. This thesis has been written at the Department of Marine Technology (IMT) at the Norwegian University of Science and Technology (NTNU) during the spring of 2020 in Trondheim, Norway.

The topic of this thesis is innovative mooring concepts for floating wind turbines, where numerical simulations have been performed to assess their capabilities. The thesis is written under the supervision of Professor II Kjell Larsen. Parts of this thesis builds on the work done in the Specialisation Project in the autumn of 2019.

During the process of writing this thesis I have gained new knowledge about the state-of-art mooring systems used in the industry and how to implement theory in modelling of mooring systems in the simulation software SIMA.

Trondheim, June 10, 2020

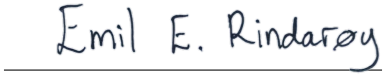

Emil E. Rindarøy

Acknowledgements

First, I would like to express my gratitude to my supervisor Kjell Larsen. The close follow-up through the whole semester has been very valuable to me in the process of writing this thesis. His patience and pedagogical methods have given me valuable knowledge on the subject.

Furthermore, I would like to thank Professor Erin Bachynski for providing the first order wave load transfer functions for the CSC substructure. I am also grateful for her willingness to help me through challenges in this project.

I would also thank PhD candidate Erling Neerland Lone for valuable help with the software SIMA during the COVID-19 lock-down.

I would also like to thank my fellow students who over the past 5 years in Trondheim and Bergen has made these years some of the best of my life. I am forever thankful.

Abstract

Offshore wind energy is considered to be one of the most promising renewable energy sources in present day. Due to large water depths, one of the main objectives of building floating wind turbines (FWT) is to expand the areas of where the wind turbines can be installed. Oil and gas (O&G) industry have for centuries had moored structures offshore and this industry has acquired a great knowledge and experience in these kinds of operations. One of the main challenges for offshore wind is the cost of energy produced compared to carbon based energy sources, and the mooring system of a FWT is one of the main cost drivers.

This thesis designs and simulate six different mooring concepts which can be used for a FWT. Five of these mooring concepts use synthetic fibre rope as mooring lines. Synthetic mooring lines are somewhat new and the mechanical properties and their capabilities are not well documented. This thesis will model both polyester and nylon mooring lines and use the state-of-art concepts to properly model them in a well known simulation software developed by Sintef called SIMA.

To have an underlying understanding of how the FWT and mooring system will behave, the underlying wave theory, equations of motion and how the software implements the theory are presented.

A reference mooring concept using well known chains and steel rope is modelled. Three different polyester mooring lines concepts are modelled; one polyester system is modelled by a linear stiffness model in a taut mooring system, the second polyester system also uses the linear stiffness model but it includes a buoy and a clump weight attached to the mooring line, and the third system uses the same buoy and clump weight system but a non-linear stiffness model is used to model the polyester lines. Lastly, two taut mooring concepts using nylon is proposed. Both are modelled with a linear stiffness model, but with different values of the stiffness.

The mooring concepts which use a buoy and clump weight show great promise for being used as mooring lines to a FWT. Both systems have low mooring line tensions, and have reasonably low stiffness which is an advantage for a mooring system. The taut mooring systems also show promise, but the leeward mooring line goes slack during the

most severe weather condition. As synthetic fibre ropes have a low resistance to seabed friction, it is unacceptable for the mooring line to go slack. A possible solution to the taut systems would be to add a buoy at the lower end of the synthetic fibre rope to prevent it from sinking down to the seabed.

Sammendrag

Vindturbiner til havs er per dags dato sett på som en av de mest lovende fornybare energikildene. Havet består av store vanndyp hvor bunnfaste konstruksjoner ikke kan installeres. Ved å utvikle flytende havvind vil et langt større område på havet være tilgjengelig for å kunne installere vindturbiner. Olje og gass industrien har i flere tiår forankret store flytende konstruksjoner langt til havs, og dermed har denne industrien skaffet seg stor kunnskap og erfaringer om hvordan dette kan gjøres på en trygg måte. En av de største utfordringene til flytende vindturbiner er kostnaden av produsert energi sammenlignet med karbonbaserte energikilder, og forankringssystemet til en flytende vindturbin er en av de store kostnadsdriverne.

Denne oppgaven designer og simulerer seks forskjellige forankringskonsepter som kan bli brukt på en flytende vindturbin. Fem av disse forankringskonseptene bruker syntetiske forankringsliner. Syntetiske forankringsliner har historisk sett vært lite brukt på konstruksjoner som skal være stasjonær i mange år, derfor er de mekaniske egenskapene og dets tåleevne lite dokumentert. Denne oppgaven bruker både polyester tau og nylon tau som forankringsliner i de forskjellige konseptene. Simuleringene er gjennomført i programvaren SIMA, utviklet av Sintef for simuleringer av marine operasjoner.

Den underliggende teorien om kreftene og responsen til en flytende konstruksjon og dens forankringssystem er viktig å etablere for å kunne analysere resultatene på en god måte. Derfor vil værlaster, bevegelsesligninger og hvordan SIMA inkluderer teorien bli beskrevet i denne oppgaven.

Et forankringssystem som bruker kjetting og ståltau som forankringsliner er modellert og brukt som referansesystem for de andre konseptene. Tre forskjellige forankringskonsepter som bruker polyestertau som forankringsliner er modellert. Et polyestersystem er et stramt forankringssystem hvor stivheten til polyesterlinene er modellert basert på en lineær stivhetsmodell. Det andre polyestersystemet bruker den samme lineære stivhetemodellene som den forrige, men en oppdriftsbøye og en klumpvekt er festet til forankringslinene. Det tredje polyestersystemet bruker de samme oppdriftsbøyene og klumpvektene, men en ikke-lineær stivhetsmodell er brukt for å modellere stivheten til polyesterlinene. Til slutt blir to stramme forankringssystemer med nylon som for-

ankringsliner modellert. Disse forankringslinene av nylon har samme dimensjon, begge bruker en lineær stivhetsmodell for å modellere stivheten til linene, men de har forskjellige stivhetsverdier.

Forankringskonseptene hvor oppdriftsbøye og klumpvekt er festet på linene viste gode resultater for å kunne bli benyttet som forankringssystem til en flytende vindturbin. Begge systemene viste lave linestrekk og de fikk en lav systemstivhet, noe som er fordelaktig for et forankringssystem. De stramme nylonsystemene viste også lave linestrekk og en lav systemstivhet. Problemet for de stramme systemene er at forankringslina som ligger i le for værretningen går i slakk for 50-årskondisjonen. Syntetiske fibertau har dårlige egenskaper mot slitasje, det er dermed uakseptabelt at linene går i slakk og legger seg på havbunn da friksjonen mellom havbunn vil skade de syntetiske tauene. En mulig løsning på dette problemet vil være å feste en oppdriftsbøye på den nedre enden av det syntetiske fibertauet.

Contents

List of Figures

List of Tables

Abbreviations

ALS	Accidental limit state
COG	Centre of gravity
CNC-5-T	Chain-Nylon-Chain 5MBL taut system
CNC-10-T	Chain-Nylon-Chain 10MBL taut system
CPC-T	Chain-Polyester-Chain taut system
CPC-BW	Chain-Polyester-Chain Buoy-Weight
CPC-BW-NL	Chain-Polyester-Chain Buoy-Weight Non-Linear
CWC	Chain-Wire-Chain
DAF	Dynamic Amplification Factor
DNV-GL	Det Norske Veritas - Germanischer Lloyd
DOF	Degrees of freedom
DP	Dynamic positioning
FLS	Fatigue limit state
FWT	Floating wind turbine
HF	High frequency
LF	Low frequency
MBL	Minimum breaking load
MPM	Most probable maximum
NTNU	Norwegian University of Science and Technology
O&G	Oil and gas
RAO	Response amplitude operator
SDOF	Single degree of freedom
SIMA	Simulation Workbench for Marine Applications
SIMO	Simulation of Marine Operations
ULS	Ultimate limit state
WF	Wave frequency

Nomenclature

A	cross-section area
A_∞	added mass infinite frequency
BM	height from buoyancy centre to metacentric height
C_D	drag coefficient
C_M	mass coefficient
C_j	wind force coefficient
C_∞	damping infinite frequency
D	transverse forcing of mooring line element
EA	axial stiffness
F	in-line forcing in mooring line element
GM	metacentric height
H^1	first order transfer function between excitation force and wave elevation
H_S	significant wave height
I	second moment of area
KB	height from keel to buoyancy centre
KG	height from keel to centre of gravity
K_E	elastic stiffness
K_G	geometric stiffness
K_T	total stiffness
L	length of body
S_C	characteristic capacity
T	effective tension in mooring line

T_H horizontal tension of mooring line

T_P peak period

T_Z vertical tension of mooring line

T_d design tension

T_n natural period

$T_{c,dyn}$ characteristic dynamic tension

$T_{c,mean}$ characteristic mean tension

$U(t)$ wind velocity

U_{hub} wind velocity at rotor hub

U_{ref} wind velocity at reference height

X total mooring line length

$\dot{x}$ body velocity

α height coefficient

ϵ_{mean} mean strain

γ_{dyn} dynamic load factor

γ_{mean} mean load factor

$\mathbf{A}(\boldsymbol{\omega})$ frequency dependent added mass matrix

$\mathbf{C}(\boldsymbol{\omega})$ frequency dependent potential damping matrix

$\mathbf{D_l}$ linear damping matrix

$\mathbf{D_q}$ quadratic damping matrix

$\mathbf{K}(\mathbf{r})$ non-linear stiffness matrix

$\mathbf{M}$ mass matrix

$\mathbf{Q}(\mathbf{t}, \mathbf{r}, \dot{\mathbf{r}})$ excitation force vector

$\mathbf{r}$ position vector

μ mean value of maxima

∇ displaced volume

$\overline{V}$ mean current velocity

ϕ elemental angle of mooring line

ρ	sea water density
σ	standard deviation of maxima
θ	pitch angle
dT	elemental tension
$d\phi$	elemental change of angle
ds	elemental suspended line length
dz	elemental vertical distance
g	gravitational acceleration
h	water depth
q_{cu}	global current force
q_{wa}	global wave force
q_{wi}	global wind force
s	suspended line length
u	horizontal fluid velocity
$u(t)$	dynamic wind gusts
w	submerged weight of chain
x_{LF}	low frequency motion
x_{WF}	wave frequency motion
z	vertical distance

Chapter 1

Introduction

1.1 Background

Offshore wind energy, including bottom fixed and floating turbines, is considered to be one of the most promising renewable energy sources in present day. According to IEA (2019) offshore wind is capable of providing 18 times of the worlds total energy demand. And according to BVG (2019) 80% of the potential for offshore wind energy in Europe is on water depths greater than 60 metres. At this water depth the bottom fixed wind turbines are not considered to be applicable since the substructure must be very large. This creates a challenge of making floating wind turbines (FWT) which can be placed at water depths greater than 60 metres.

The main challenge of FWT is that the cost of the power produced are large compared to oil and gas (O&G), and this cost needs to be reduced in order to make FWT profitable. For a FWT the mooring system is today about 1/3 of the total cost to build the FWT. This is due to the very expensive chains needed. Therefore, there is a large focus in the industry to find suitable alternatives to using chain, or to change the conventional mooring systems more cost-efficient.

1.2 Objective

This thesis will focus on new mooring concepts for a FWT. These concepts include substituting chains with synthetic fibre rope as polyester and nylon.

To be able to model new mooring concepts, the underlying theory for mooring must be studied. This thesis will include relevant literature and a presentation of the state-of-art floating wind turbines. Synthetic fibre ropes mechanical behaviour and tension-elongation characteristics are presented. Rules and regulations are studied so that the mooring system design is in accordance with the classification society.

Using time domain simulations, all mooring concepts are analysed to study which mooring concept are feasible to use as mooring systems for a FWT. This thesis will only simulate the ultimate limit state (ULS) of the mooring systems. To comply with DNV-GL also accidental limit state (ALS) simulations and fatigue limit state (FLS) simulations must be performed. Due to the workload of the ULS simulations for the six mooring concepts, the ALS and FLS simulations are not covered in this thesis.

1.3 Thesis Outline

Chapter 2 presents a state-of-art overview of the FWT concepts which have been recently built or are under construction.

Chapter 3 presents different types of mooring systems and the basic theory needed to safely design a mooring system. Different types of anchors and mooring lines are also presented.

Chapter 4 presents the equations of motion for the floating structure. Wave, wind and current loads are discussed and the theory behind these loads are presented.

Chapter 5 presents the software SIMA and the underlying theory of this computer software. This chapter also presents the different integrated computer programs in SIMA which are used to analyse the mooring concepts.

Chapter 6 presents the rules and regulations stated by the classification society DNV-GL on floating wind turbines.

Chapter 7 presents how the wave, wind and current loads are calculated and the results of these calculations.

Chapter 8 presents the mooring concepts which are used for simulations in this thesis.

Chapter 10 presents how the substructure, mooring lines and environmental loads are modelled in SIMA.

Chapter 11 presents and discusses the results from the simulations performed in this thesis.

Chapter 12 states the conclusions made from the simulations and recommendations for further work are presented.

Chapter 2

Floating wind turbine concepts

This chapter will discuss different floating wind turbine concepts and present some of the concepts which have been realised.

According to IEA (2019) offshore wind is capable of providing the world up to 18 times the global energy demand. And in recent years a number of different floating wind turbine concepts has been proposed. Some of them have been through full scale model tests, while some are still in the concept phase.

Figure 2.1: Different offshore wind turbine concepts, Beiter et al. (2016).

Figure 2.1 shows six different offshore wind turbine concepts which is presented in an article written by Beiter et al. (2016). In this figure three bottom fixed turbines and three floating turbines are presented. The three floating concepts include one semi-

submersible substructure, one tension-leg platform and one spar substructure. All of these three concepts of floating wind turbines are possibilities which are studied and tested in present day.

In the following sections three different FWT concepts are presented.

2.1 Hywind

Hywind is a floating wind turbine project launched by Equinor in 2001, Equinor (2020a). Equinors Hywind project sets aim to commercialise floating wind turbines, making them a renewable energy source which can be utilised all over the world.

Hywind is designed as a ballasted spar buoy which which is moored by three mooring lines. An illustration provided by Equinor (2019b) seen in Figure 2.2 shows the Hywind Scotland project.

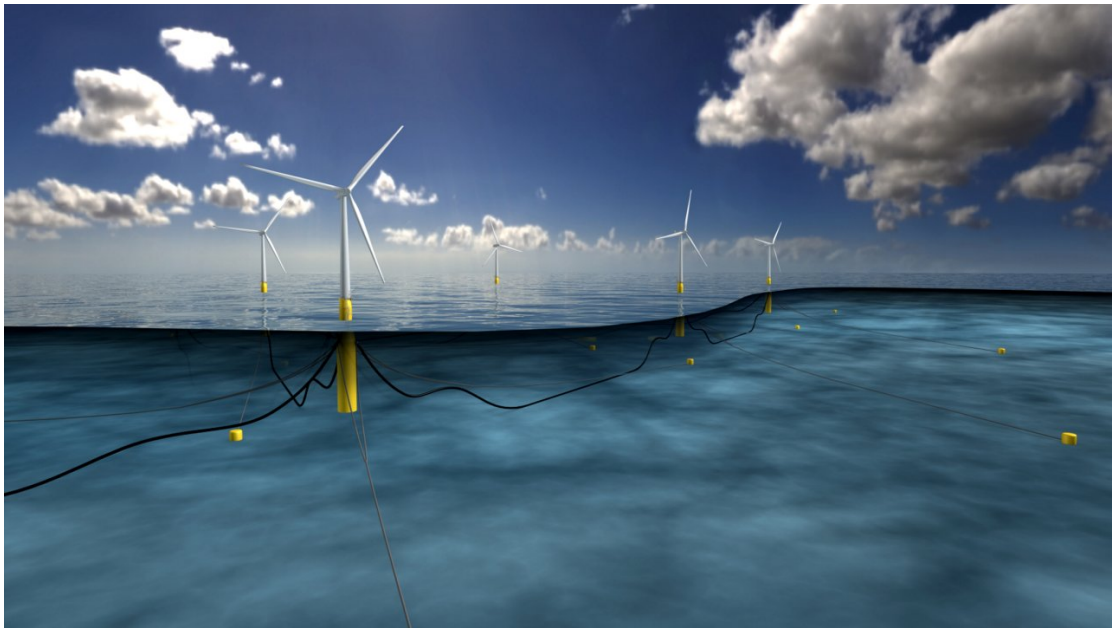

Figure 2.2: Illustration of Hywind Scotland, Equinor (2019b).

Since the substructure is a spar buoy, it is critical that Hywind controls its yaw motion. This is solved by attaching the mooring lines to a bridle which is then connected to the substructure. This bridle can be seen in Figure 2.3.

Another key aspect of building the substructure as a spar buoy is that the substructure will have a large draft. Hywind Scotland and Hywind Tampen will have a draft of 78 metres. This creates challenges regarding installation and towing of the substructure.

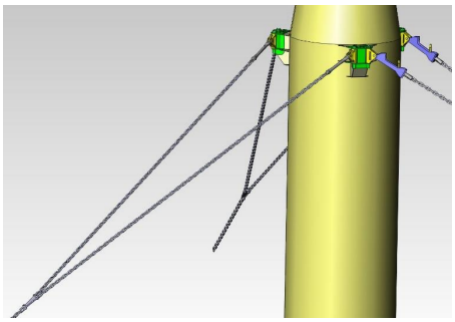

Figure 2.3: Bridle used on Hywind, Equinor (2017).

2.1.1 Hywind Demo

Hywind Demo was the first full scale model of the Hywind concept which was built and commissioned in 2009, Equinor (2020b). This is a 2.3 MW FWT which was installed outside of Karmøy, Norway. The main purpose of Hywind Demo was to test its capabilities.

It ended up producing more than 40 GWh with a capacity factor of 50%, Equinor (2020b).

2.1.2 Hywind Scotland

Hywind Scotland is Equinors pilot farm project of FWTs. This pilot farm consists of five 6 MW FWTs and it is placed approximately 30 km of the coast of Scotland, Equinor (2019b).

This FWT park has produced electricity since 2017, floating at water depths between 96-129 metres. These FWT follows the same principles of construction as the Hywind Demo, only scaled up.

2.1.3 Hywind Tampen

Hywind Tampen is a floating wind turbine farm which consists of 11 FWT which are developed by Equinor. The purpose of the project is to provide clean energy to 5 O&G platforms which operate on the Snorre and Gullfaks reservoirs. The Hywind Tampen project is planned to provide approximately 35% of the annual power demand of these platforms. In October 2019, Equinor and the stakeholders at Gullfaks and Snorre announced that they will proceed in developing Hywind Tampen, Equinor (2019a).

Each FWT will have a power capacity of 8 MW and will use the same concepts used and developed through the Hywind Scotland and Hywind Demo projects. The development of this project will cost up to 5 billion NOK.

The wind farm will be installed approximately 140 km offshore, with a water depth of 270-300 metres. An illustration of Hywind Tampen is seen in Figure 2.4.

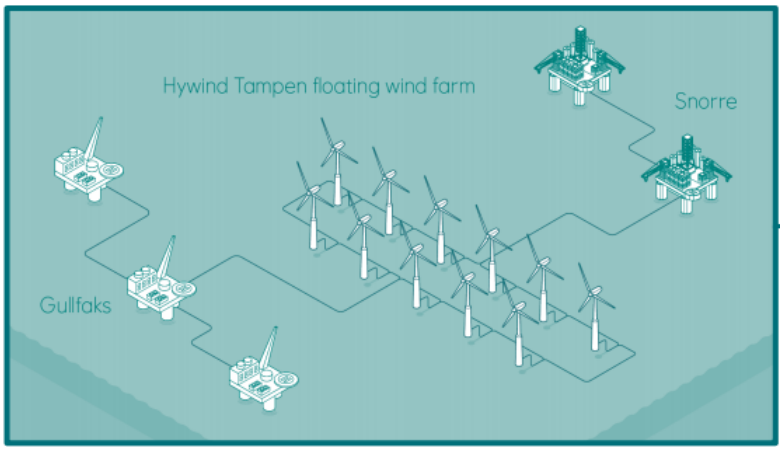

Figure 2.4: Illustration of Hywind Tampen, Nysæther (2019)

The project is scheduled to start in late 2022. As discussed in the beginning of this section, one of the major challenges for FWT is to reduce cost. One of the biggest cost drivers is the mooring system of a FWT, and a large amount of research and development are being done to lower this cost.

Hywind Tampen will use traditional chains with the same configuration as used in Hywind Scotland. Each mooring line is connected to a suction anchor at the seabed, and some of the mooring lines in the FWT farm shares the same suction anchor. A preliminary mooring configuration of Hywind Tampen is seen in Figure 2.5.

According to Larsen (2020a) the horizontal length between the suction anchor and the FWT is approximately 1000 metres.

The key difference between Hywind Tampen and the previous Hywind projects is that Hywind Tampen will use a concrete substructure instead of steel.

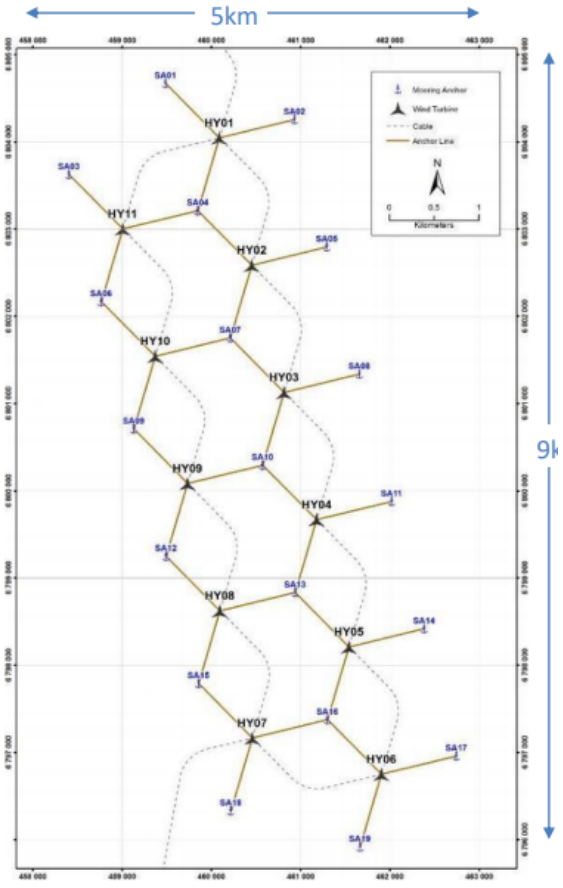

Figure 2.5: Mooring configuration of Hywind Tampen, Larsen (2020a).

This thesis will look at different mooring concepts using the same geographic location

and the same anchor configuration as Hywind Tampen. Hence, the same Metocean data for the Hywind Tampen location and water depth are used in this thesis.

2.2 WindFloat

WindFloat is a floating wind turbine project by Principle Power. WindFloat uses a semi-submersible substructure made of steel. In 2011 the first full scale 2 MW WindFloat was installed of the coast of Portugal, Power (2020).

Seen in Figure 2.6 the WindFloat substructure is a semi-submersible with the turbine sitting on top on of the columns.

Figure 2.6: WindFloat, Power (2020).

WindFloat uses a column-stabilised semi-submersible substructure which is connected through braces. Compared to Hywind the draft of WindFloat is considerably less. WindFloat have a draft between 10-20 metres depending on the size of turbine that is placed upon it. This means that the installation and towing can be done more easily at quayside.

2.3 CSC semi-submersible

The semi-submersible substructure proposed by Wang (2014) is one of many design iterations of the design initially proposed by Luan et al. (2018). The CSC 10 MW FWT uses the same concept as WindFloat, using a column-stabilised three column semi, but the CSC places the wind turbine in the middle of the semi-submersible compared to WindFloat who places the wind turbine on top of one of the columns. The CSC also have no braces connecting the columns, instead the CSC uses submerged pontoons.

This thesis will use the design iteration proposed by Wang (2014) as floater and different mooring concepts will be tested using the CSC. More detailed information about the CSC 10 MW is presented in Chapter 9.

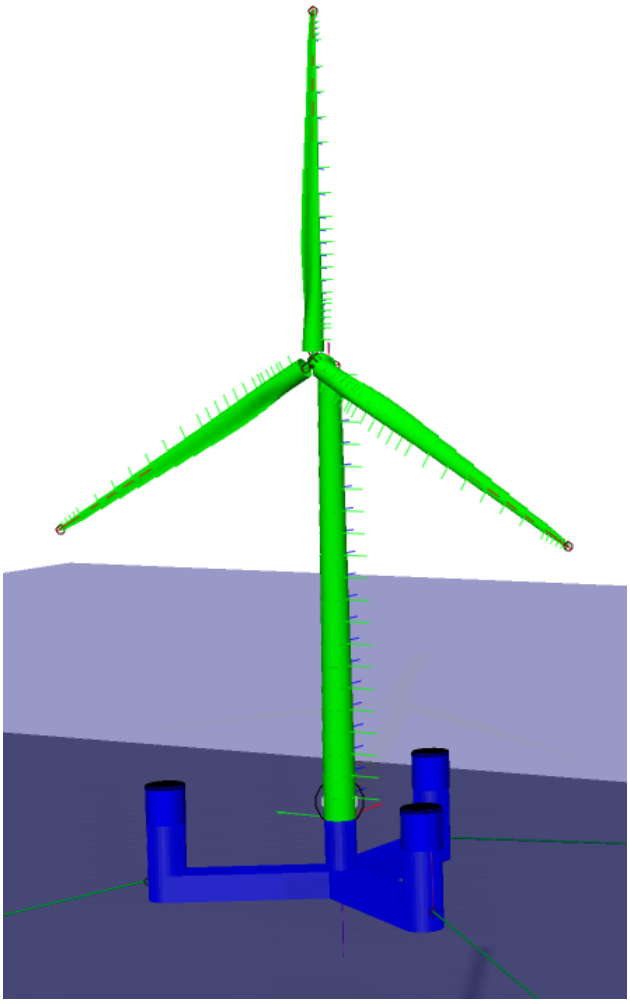

Figure 2.7: CSC 10 MW FWT proposed by Wang (2014).

Chapter 3

Mooring systems and station keeping

This chapter discuss the different mooring systems that are used for semi-submersible structures operating today, and different mooring systems which are not widely used, but are interesting concepts for a FWT. Briefly, the different components necessary for a mooring system are explained.

As long as floating structures have existed station-keeping has been a subject which has been heavily tested and studied. Conventional use of a mooring line connected to the structure down to an anchor was for many years the only way to secure a structure. Station-keeping then evolved to include catenary mooring, taut mooring, dynamic positioning (DP), single-point mooring and tension leg mooring as different systems applicable for a variety of station-keeping challenges.

For FWTs dynamic positioning is not applicable, due to the longevity of the station-keeping. The mooring system is a huge contributor to the total manufacturing cost of a FWT. There is therefore large focus in the industry to reduce cost in this segment, and different mooring concepts are being investigated.

3.1 Mooring Systems

Station-keeping of an offshore structure is crucial for the structure to be able to perform as designed. For a floating wind turbine the most important aspect of the mooring system is to control the mean offset of the FWT within an acceptable limit.

Floating wind turbines shall operate for several years, so the requirement of stationarity for a long life span is highly important. The time span and requirement of a small offset rules out dynamic positioning and single point mooring.

This thesis will focus on catenary and taut mooring, hence only these two mooring systems will be described further. The other station-keeping systems are left to the reader to study.

3.1.1 Catenary

Mooring systems using chains, or a combination of chain and steel rope, are the most common mooring system today. The weight of chain and steel rope will make the mooring lines form a catenary geometry. The mooring lines must be sufficiently long so that the lines rest on the seabed in a static condition. The chains are very well suited against wear and tear, this is fundamental as the chains will be scratching against the seabed for many years.

Mooring chains are made of steel, and steel have a very high density. Hence the chains will have a large submerged weight, which will give the mooring lines a catenary geometry.

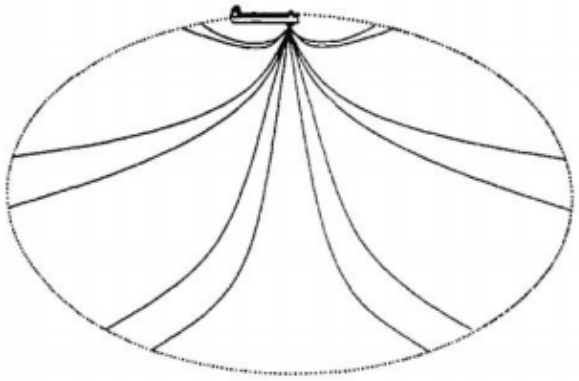

Figure 3.1: FPSO catenary mooring, Chakrabarti (2005)

Seen in Figure 3.1 the line length of catenary mooring is very long, and since the price of steel to this date is high, the total cost of the mooring system can be very large.

The advantages of using steel chains and its weight is as earlier stated its wear and tear capabilities, its well known properties, but also the large submerged weight can be an advantage in mooring systems. The stiffness of the system will get softer, and this can be of great importance. How the submerged weight affects the stiffness of the system will be described in section 3.3.

3.1.2 Taut mooring

Taut mooring is where the mooring lines will go in a approximate straight line from the anchor to the moored structure. Taut mooring is applicable when using synthetic mooring lines because of the light submerged weight of synthetic mooring lines, which will not create a geometric stiffness. Therefore, synthetic mooring lines must be pretensioned so that they do not go slack.

Since synthetic mooring lines have a low submerged weight, the mooring lines can reach a taut geometry without using excessive force on the mooring line.

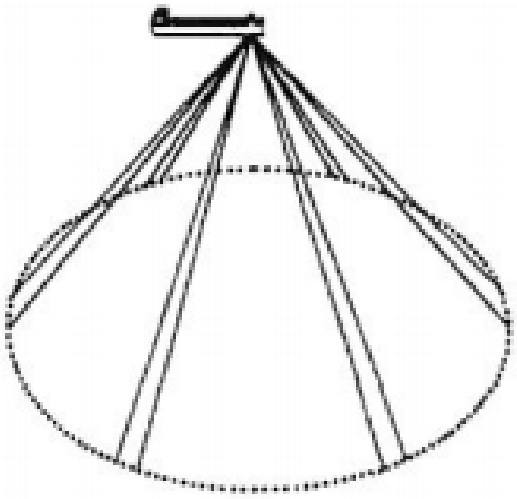

Figure 3.2: FPSO taut mooring, Chakrabarti (2005)

Seen in Figure 3.2 the line lengths are largely decreased compared to the catenary geometry.

The use of synthetic mooring lines have a great cost benefit. The drawbacks are that taut mooring can make the mooring stiffness very stiff since the stiffness is only dependent on the axial stiffness of the mooring lines. Another drawback is that synthetic mooring lines are not well suited against wear and tear. This makes them exposed for seabed friction and vessel propellers. How the system stiffness is affected by the mooring line are discussed in section 3.3.

3.2 Catenary Equations

To be able to calculate the line tension and outreach of the mooring lines when using chain, the catenary equations are used. A catenary line is presented in Figure 3.3.

The distance X_B is the length of chain lying on the seabed. ϕ_0 is at the point where the mooring line is lifted from the seabed, ϕ is the angle in the XZ-plane of an arbitrary element and ϕ_w is the angle of the mooring line when intersecting the water plane. s is the suspended length of chain and h is the water depth. T_H is the horizontal tension in the mooring line and T is the effective tension in the line.

By studying a small element on the suspended line, ds, we can find the elemental tension dT and angle ϕ. An element of length ds is seen in Figure 3.4.

The following equations are based on the assumptions that we have a totally flat seabed,

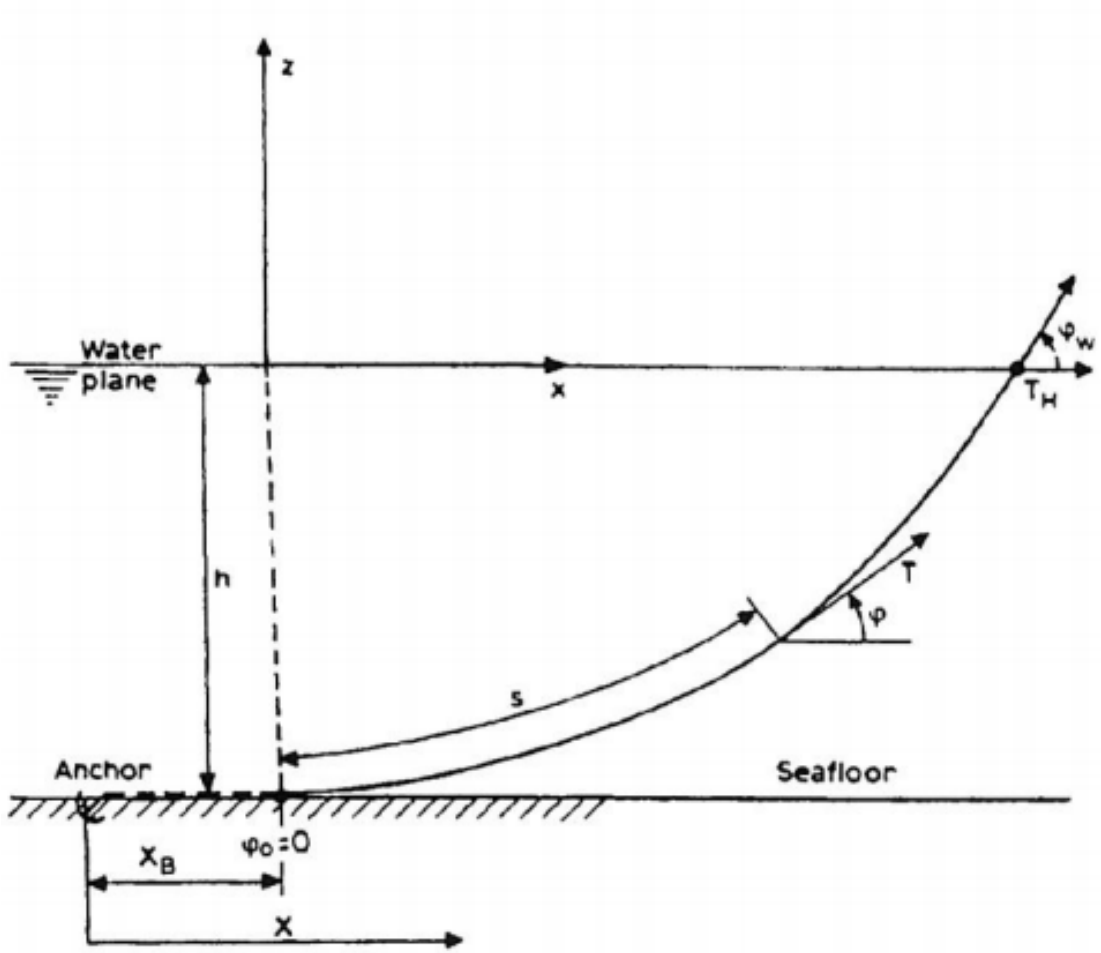

Figure 3.3: Catenary mooring line, Chakrabarti (2005)

and that the bending stiffness effects are neglected, Chakrabarti (2005).

Seen in Figure 3.4 the weight of the line segment, wds, is the constant submerged line weight per unit length. The following expressions for in-line forcing and transverse forcing respectively can be developed:

$$dT - \rho g A dz = \left[w sin\phi - F\left(\frac{T}{EA}\right)\right] ds \tag{3.1}$$

Where ρ is the sea water density, A is the cross-section area, dz is the vertical elemental length, w is the submerged weight, F is the axial force and EA is the axial stiffness from Young's modulus E multiplied with the cross-section area.

$$Td\phi - \rho g A z d\phi = \left[w cos\phi + D\left(1 + \frac{T}{EA}\right)\right] ds \tag{3.2}$$

For the transverse forcing seen in Equation 3.2 $d\phi$ is the change in elemental angle in

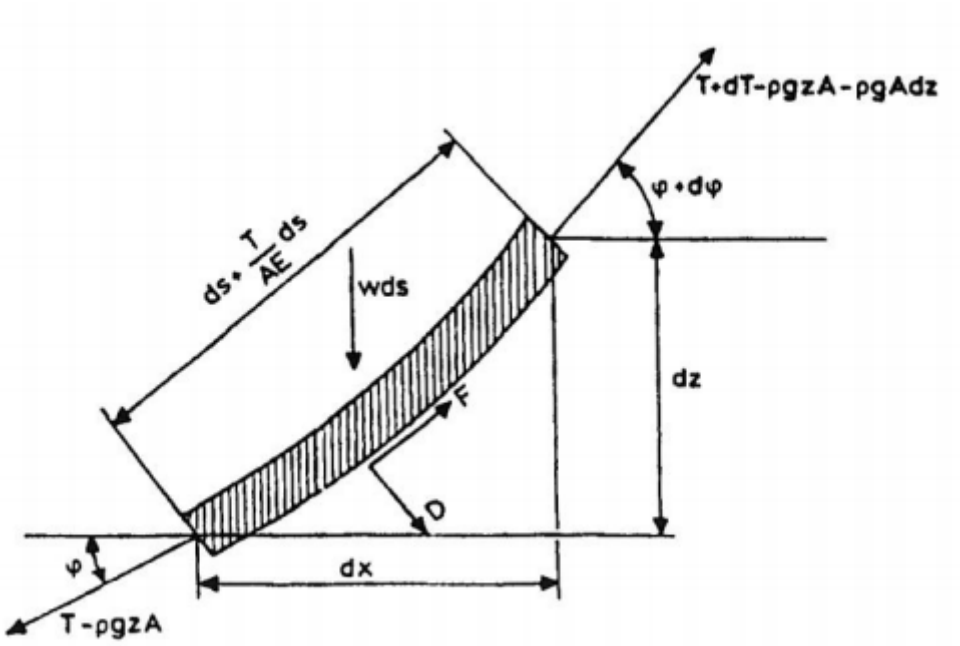

Figure 3.4: Catenary line element, Chakrabarti (2005)

the XZ-plane, z is the vertical distance, ϕ is the elemental angle and D is the transverse force.

Given the assumptions stated, we can obtain the suspended line length s and vertical dimension h as:

$$s = \left(\frac{T_H}{w}\right) sinh\left(\frac{wx}{T_H}\right) \tag{3.3}$$

$$h = \left(\frac{T_H}{w}\right)\left[cosh\left(\frac{wx}{T_H}\right) - 1\right] \tag{3.4}$$

The tension in the top of the mooring line can then be expressed in terms of the line length s and water depth h:

$$T = \frac{w\left(s^2 + h^2\right)}{2h} \tag{3.5}$$

The vertical component of the line tension becomes:

$$T_Z = ws \tag{3.6}$$

And the horizontal component:

$$T_H = Tcos\phi \tag{3.7}$$

3.3 Stiffness

The stiffness of a system is its ability to resist motion from its equilibrium. A high stiffness implies that a large force is needed to induce a motion to the system. Stiffness of a mooring system is the sum of elastic and geometric stiffness.

3.3.1 Geometric

Geometric stiffness is a physical property that is derived from the mooring lines geometry change from an equilibrium position. Seen in Figure 3.5 the horizontal offset, x, from equilibrium will lift more of the chain from the seabed and increase the suspended weight resultant of weight in water, w.

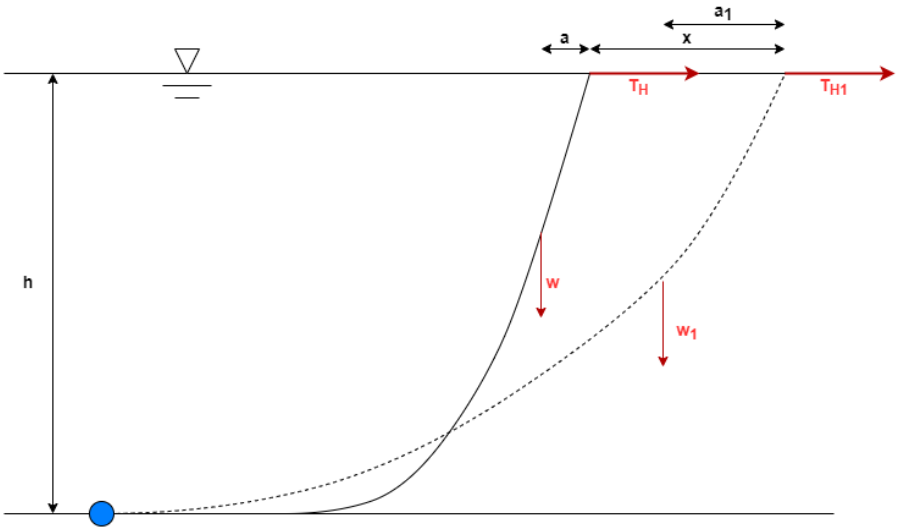

Figure 3.5: Horizontal offset in catenary mooring

Seen in Figure 3.5 a horizontal offset x will increase the suspended weight in water w to w_1. This increase in suspended line will hence increase the horizontal tension, T_H, as well. In Figure 3.5 a and a_1 is the arm from the suspended weight resultant to the top of the line. This arm can be used to calculate the equilibrium of the mooring line around the anchor (blue dot in Figure 3.5).

Equilibrium of the line:

$$T_H \cdot h = w \cdot a \tag{3.8}$$

The geometric offset can then be calculated as the change in horizontal tension T_H divided by the offset, x:

$$K_G = \frac{T_{H1} - T_H}{x} \tag{3.9}$$

3.3.2 Elastic

Elastic stiffness is the stiffness of the mooring line itself and for steel structures it is generally very high. Elastic stiffness can be written as:

$$K_E = \frac{EA}{L} \tag{3.10}$$

Where E is the material property Young's modulus, A is the cross-sectional area and L is the length of the structure.

3.3.3 Total stiffness

The total stiffness can then be considered as two springs (geometric and elastic) connected in a series. This yields:

$$\frac{1}{K_T} = \frac{1}{K_E} + \frac{1}{K_G} \tag{3.11}$$

Explicitly, Equation 3.11 can be written as:

$$K_T = \frac{K_G \cdot K_E}{K_G + K_E} \tag{3.12}$$

Equation 3.11 is the total stiffness of a mooring line. To find the total stiffness of the mooring system, pullout tests must be performed. Pull-out tests are further described in Chapter 10.

3.4 Mooring Lines

As previously mentioned there are three main line types used for mooring of floating structures. These line types are described in this section.

3.4.1 Chain

Chain are the most common mooring line to date. The extensive use of chains for mooring lines have made the limitations and applications of chain well documented.

There are two different chain types that are much used, studded and stud-less chain. Studded chains have a higher capacity than the stud-less, and the stability of the links are also improved. But the added weight of each link for studded chain are a negative factor in terms of cost and weight of each link. The two chain links are seen in Figure 3.6.

Chains have been very popular to use in mooring systems that shall have a long life span.

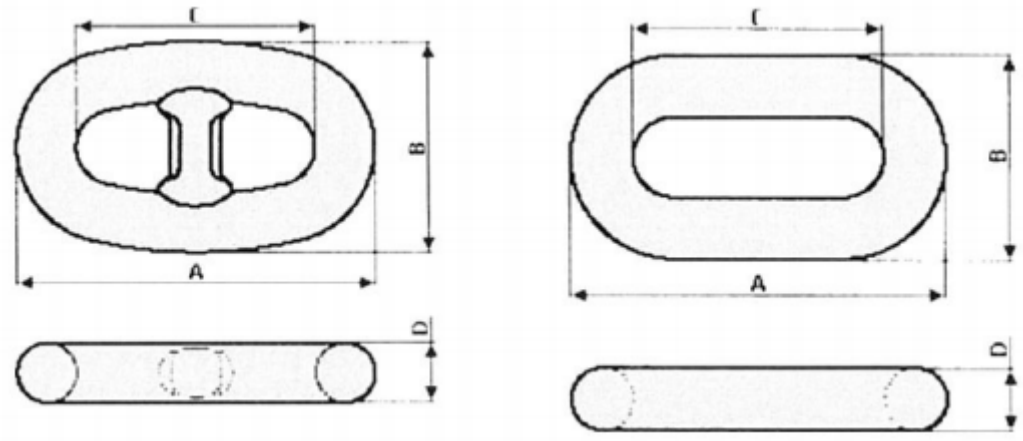

Figure 3.6: Studded and stud-less chain, Chakrabarti (2005)

This is due to steels high breaking strength and the fact that it is heavy and have good properties when it comes to wear and tear.

The drawback are the cost of steel, and the fact that they are corrosive.

3.4.2 Wire Rope

Wire rope consists of layers of wires made of steel that are wounded to create a helical pattern, this is called a strand. Mooring lines using wire rope consists of multi-strand or single-strand. The pattern of the helical wires define the elasticity of the wire rope. The benefits of using wire rope is that it is cheaper than chains and the reduced weight compared to chains, increases the payload which the mooring line may hold. Wire rope can also be more resistant to corrosion when an galvanised layer of paint is smeared on the wire. It is also possible to have some strands of zink included in the wire rope.

Different strand configurations are shown in Figure 3.7.

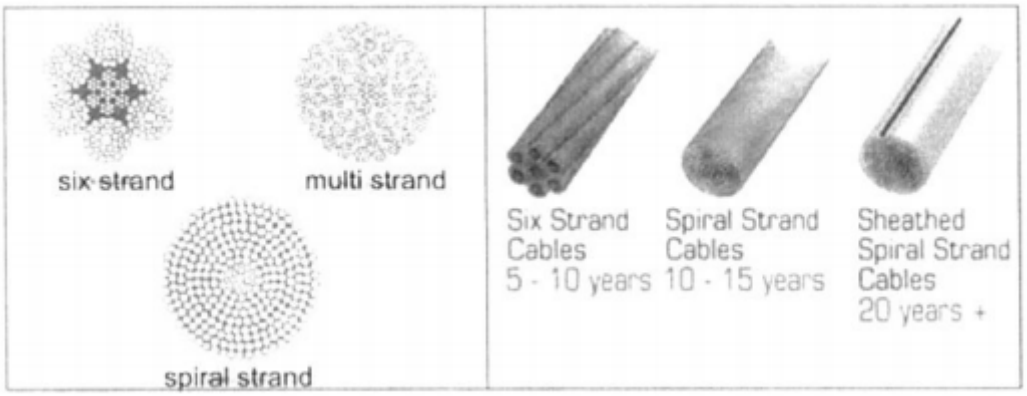

Figure 3.7: Wire rope configurations, Chakrabarti (2005)

A combination of wire rope and chain are used in Hywind Tampen. Chains are used at

the top and bottom of the mooring line, while wire rope are used on a large part of the suspended length of the line.

3.4.3 Synthetic Fibre Rope

The use of synthetic fibre rope as mooring lines have been under research for many years. There are now four different synthetics that are used in the industry. These are polyester, Aramid, HMPE's and nylon. Fibre rope are much more flexible than chain and wire rope, and therefore much easier to handle and to install.

Fibre ropes consists of many threads of yarn that are braided together, making them stronger. In Figure 3.8 a cross-section of a typical layout of the fibre rope is presented.

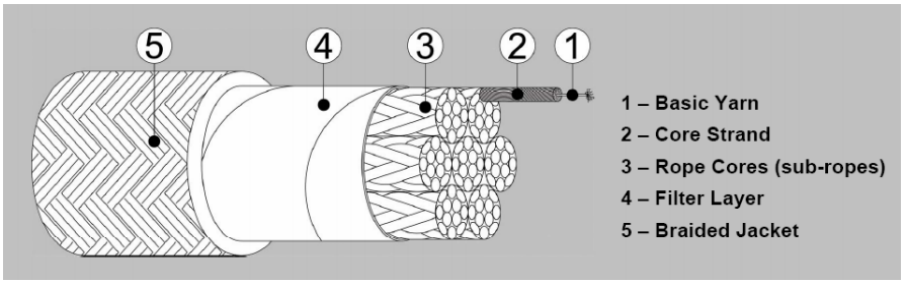

Figure 3.8: Cross-section of fibre rope, Larsen (2019)

Other benefits of choosing fibre rope is similar to wire rope, the fibre ropes light weight increases the payload of the floating structure. Taut mooring are used for fibre rope, which may lead to a very stiff mooring system. This reduces the offset of the structure, which leads to cheaper riser solutions. The cost for fibre rope is also much lower than chain, and the reduced line length because of the taut mooring, will also help to reduce the total cost of the mooring system.

This thesis will use polyester and nylon for different mooring concepts.

Bridon Superline Polyester

This thesis will use Bridons Superline Polyester, Bridon (2013), properties when modelling. According to Bridon, this is a torsionally balanced mooring line which offers the highest strength to weight ratio for permanent mooring solutions.

Bridon Superline Nylon OCIMF 2000

This thesis will also use Bridons Superline Nylon OCIMF 2000 properties for modelling of nylon mooring lines, Bridon (2013). Bridon states that the Superline Nylon is torsionally balanced like the polyester. The mechanical properties of the Superline Nylon can be seen in Appendix D.

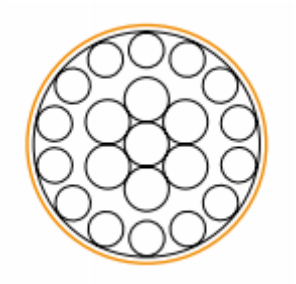

Figure 3.9: Cross-section of Superline Polyester, Bridon (2013).

3.5 Anchors

Anchors are a critical part of the mooring system as it is the connection point between the mooring line and the seabed. There are several types of anchors for different applications, and only a few relevant for FWT, will be briefly described in the following section. It is left to the reader to study anchors to get a more detailed description.

3.5.1 Suction anchors

Suction anchors is a cylindrical tube with an open bottom. These anchors are sunk down to the seabed and are pushed down into the soil of its own weight. By pumping out the water inside the cylinder a negative pressure inside the cylinder will "suck" the anchor down in the soil. The suction anchor will effectively be "locked" in place by its own weight and a "vacuum" inside the cylinder.

Figure 3.10: Suction anchors, ResearchGate (2017)

The main advantage of suction anchors is that they can take tension both horizontally and vertically. Other anchors can only take horizontal tension which make them not

applicable for taut mooring.

Hywind uses suction anchors to secure their FWT, and this thesis will also use suction anchors.

3.5.2 Fluke anchors

Fluke anchors are a more traditional anchor which uses friction as its main source of resistance. Fluke anchors are lowered down towards the seabed and dragged by the seabed until it has dug itself sufficiently down into the soil.

Figure 3.11: Fluke anchor, Vryhof (2020).

These anchors are commonly used for chain mooring. One of the main reasons fluke anchors are popular is that they are easy to manufacture hence, they are cheap. For traditional O&G installations using chain a sufficient length of the chain will rest on the seabed which will make all the tension horizontal in the line at the anchor.

3.5.3 Torpedo anchors

Torpedo anchor is a original anchor type which uses gravity to embed the anchor to the seabed. By lowering the torpedo anchor into the sea, and the dropping the anchor using its weight and gravity the anchor will torpedo itself down into the seabed.

One of the drawbacks using this anchor is that the anchor placement will not be very accurate. But for mooring systems where this is not critical, the torpedo anchor have significant advantages in installation cost.

Figure 3.12: Torpedo anchor, GcCaptain (2012)

Chapter 4

Equations of Motion

To be able to describe the motions of a floating structure, we must first identify the contributions from the time dependent accelerations, velocities, motions and forces on the structure.

The equation of motion for six degrees of freedom (DOF) are seen in Equation 4.1.

$$(\mathbf{M} + \mathbf{A}(\boldsymbol{\omega})) \cdot \ddot{\mathbf{r}} + \mathbf{C}(\boldsymbol{\omega}) \cdot \dot{\mathbf{r}} + \mathbf{D_l} \cdot \dot{\mathbf{r}} + \mathbf{D_q} \cdot \dot{\mathbf{r}}|\dot{\mathbf{r}}| + \mathbf{K}(\mathbf{r}) \cdot \mathbf{r} = \mathbf{Q}(\mathbf{t}, \mathbf{r}, \dot{\mathbf{r}}) \tag{4.1}$$

where:

M: mass matrix
A(ω): frequency-dependent added mass matrix
r: position vector
C(ω): frequency dependent potential damping matrix
$\mathbf{D_l}$: linear damping matrix
$\mathbf{D_q}$: quadratic damping matrix
K(r): non-linear stiffness matrix
Q(t,r,ṙ): excitation force vector

This equation is derived from Newton's second law, $\sum F = m \cdot \ddot{x}$. For a floating structure, damping and stiffness is introduced in the equilibrium equation.

All six degrees of freedom are presented in Figure 4.1

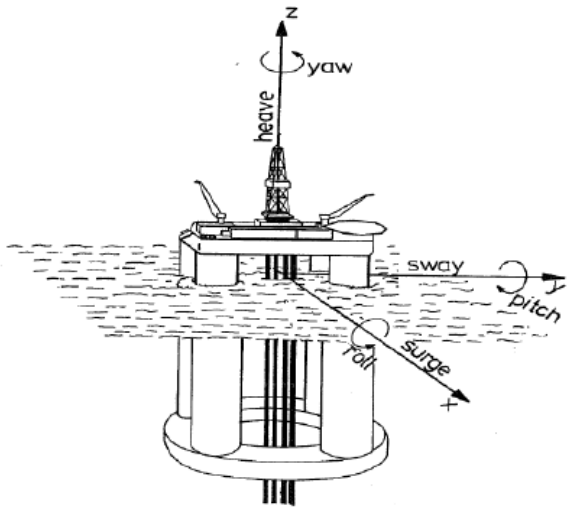

Figure 4.1: Six degrees of freedom on offshore structure. Faltinsen (1990)

A large number of time domain simulations are to be performed using SIMA. The need to understand the mathematical theory which SIMA is based on is therefore essential to be able to correctly evaluate the simulation results.

4.1 Excitation Forces

The floating wind turbine will be subjected to wind, current and wave loads. These excitation forces $Q(t, x, \dot{x})$ are important to identify and study to be able to understand how the FWT will behave in the ocean.

One of the most important parameter which needs to be identified, is the frequencies in which these excitation forces act and the amplitude of the forces. If the structures natural frequency and the excitation frequency is in the vicinity of each other, the structure motions may become too large to control. Which can ultimately lead to structural failure of the mooring lines or the structure itself.

4.1.1 Wind Forces

Global wind forces can be calculated as

$$q_{wi}(t) = \frac{1}{2} \cdot \rho_{air} \cdot C_D \cdot A \cdot (U(t) - \dot{x})^2 \tag{4.2}$$

where:

U(t)= $\bar{U}$+u(t)
$\bar{U}$: mean wind velocity
u(t): dynamic wind gusts
$\dot{x}$: is the low-frequency velocity of the structure

By inserting $\bar{U}$ and u(t) into Equation 4.2 the equation is re-written as:

$$q_{wi} \approx \underbrace{\frac{1}{2} \cdot \rho_{air} \cdot C_D \cdot A \cdot \bar{U}^2}_{\text{Constant force}} + \underbrace{\rho_{air} \cdot C_D \cdot A \cdot \bar{U} \cdot u(t)}_{\text{Low-frequency excitation force}} - \underbrace{\rho_{air} \cdot C_D \cdot A \cdot \bar{U} \cdot \dot{x}}_{\text{Low-frequency damping}} \tag{4.3}$$

Equation 4.3 shows hot the global wind force can be decomposed into three governing contributions. The constant force is due to the mean wind velocity. This will cause a mean drift of the FWT.

The second term contains LF dynamic wind gusts. These gusts gusts have significant energy at surge, sway and yaw natural oscillation periods, which means that the wind gusts will excite low-frequency motions of moored floating structures, Larsen (2019).

The third term in Equation 4.3 are the low-frequency damping force which is introduced by the low-frequency velocity of the structure. Notably the third term is a negative contribution to the total wind forces and is hence a damping term. Logically, the LF velocity of the structure will make the actual wind velocity that the FWT experiences lower than the wind velocity in a fixed point. This damping contribution is included in the the damping matrix in Equation 4.1.

Wind forces acting on the FWT will consist of drag forces on the tower, nacelle and substructure, as well as the thrust force on the operational rotor.

The thrust curve for the DTU 10MW reference turbine is shown in Figure 4.2. This curve is taken from the Master Thesis of Wang (2014), and show the thrust force on the rotor as a function of wind speed. The thrust curve is only for the operational turbine, and the turbine is operational in the range of 4-25 m/s.

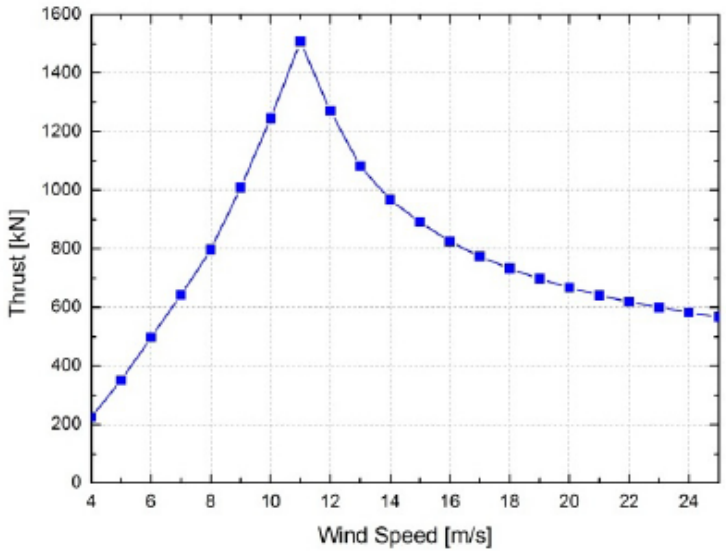

Figure 4.2: Thrust curve of DTU 10 MW reference wind turbine, Wang (2014).

When the wind turbine is operational the thrust force on the rotor is expected to be the largest wind force on the structure. Seen in Figure 4.2, the thrust force is increasing quadratically until the wind speed reaches the rated wind speed of 11.4 m/s. Then the thrust will decrease with an approximately exponential shape. This decrease in thrust is due to the blades pitching to maintain a constant rotor speed, and consequently a constant energy production.

For wind speeds above 25 m/s the wind turbine will feather its blades and park the rotor. This will make the thrust force on the rotor only dependent on drag and the only contribution to the wind force will be from drag on the FWT elements.

A more detailed discussion around wind forces are done in Chapter 10 when the modelling in SIMA are explained.

4.1.2 Current Forces

For motion of floaters, it is the current velocity at the surface that is of primary interest. The current velocity at larger water depths will only create a drag force on the mooring lines which will be much lower than the effect the current will have on the floating structure. But the current velocity down in the water depths is not to be neglected as the drag forces on the mooring lines can create a greater mean offset of the floater.

The global current forces are expressed as:

$$q_{cu}(t) = \frac{1}{2} \cdot \rho \cdot C_D \cdot A \cdot |\bar{V} - \dot{x}| \cdot (\bar{V} - \dot{x}) \tag{4.4}$$

where:

$\bar{V}$: constant current velocity
$\dot{x}$: low-frequency velocity of structure
C_D: drag coefficent
A: cross-sectional area
ρ: sea water density

If $\bar{V} > \dot{x}$, Equation 4.4 can be approximated as:

$$q_{cu}(t) \approx \underbrace{\frac{1}{2} \cdot \rho \cdot A \cdot \bar{V}^2}_{\text{Constant force}} - \underbrace{\rho \cdot C_D \cdot A \cdot \bar{V} \cdot \dot{x}}_{\text{Low-frequency damping}} \tag{4.5}$$

If $\bar{V}$ is larger than $\dot{x}$, the low-frequency damping will increase the total damping. The assumption that the current velocity is larger than the structure motion may not be valid if the LF motion of the structure is large, and the current velocity is low. The LF

motions must be studied to know if the assumption is valid.

Equation 4.5 show that the current will have a constant term and a LF damping term. This constant term will a large effect on the surge and sway motions of the FWT.

4.1.3 Wave Forces

Loads from waves can be divided into two main contributions, first order wave loads and second order wave drift loads. The first order loads are in general larger than the second order loads, hence they are of most important for a floating structure. But the linearization used in calculating the first order loads neglects some important effects which may be of significance to avoid resonant motion.

Linear wave excitation loads

Wave excitation loads are the forces and moments on the body when the structure is restrained from oscillating and there are regular incident waves, Faltinsen (1990). These hydrodynamic loads are composed of Froude-Kriloff and diffraction forces and moments. Froude-Kriloff force comes from unsteady pressure induced by the undisturbed incident waves. Considering a fixed vertical cylinder penetrating the free-surface, seen in Figure 4.3, as the waves passes the cylinder, the pressure along the surface of the cylinder changes with the waves. Diffraction forces take into account the presence of the cylinder which will affect the pressure within the incident waves. These loads are calculated using potential theory, where the loads are considered linear and the contribution of the two loads can be superimposed to get the total linear wave excitation loads.

A more detailed explanation of these loads will not be given in the thesis. Reference is done to Faltinsen (1990). By deriving the expressions for the total linear wave excitation loads, we get Morisons equation:

$$dF = \underbrace{\rho \frac{\pi D^2}{4} \cdot C_M \cdot a_1 \cdot dz}_{\text{Mass force}} + \underbrace{\frac{\rho}{2} C_D \cdot D \cdot |u|u \cdot dz}_{\text{Drag force}} \tag{4.6}$$

Where D is the diameter of the cylinder, C_M and C_D is the mass and drag coefficient, a_1 is the acceleration at the mid-point of the strip, u is the horizontal undisturbed fluid velocity and dz is the elemental length of the strip.

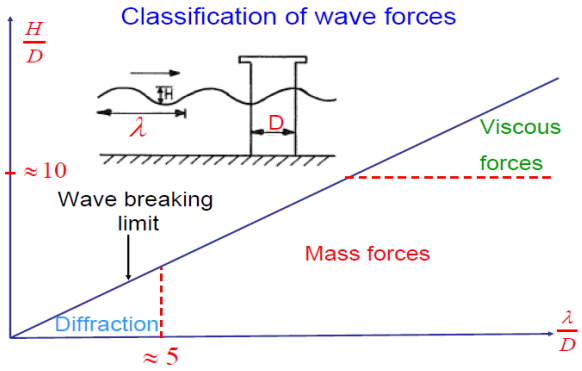

Figure 4.3: Classification of wave forces Greco (2019)

As seen in Figure 4.3, diffraction, mass and viscous forces are dominant for different geometries and wave lengths of the incident wave.

The floating wind turbine has cylindrical substructure and tower. Morison's equation is applicable for structures where the wavelength, λ, divided by the diameter is equal or larger than 5. Integrating over the length of the FWT we get the drag and Morison forces.

Second order wave drift loads
Second order mean wave drift forces are generally much smaller than the first order wave forces. These loads are more difficult to estimate than the linear contributions to the loads, both numerically and experimentally. This is due to the sensitivity in the input of geometry details, incident waves, first order motion etc. which can have a large significance in the calculated results since second order effects are generally smaller than first order wave forces.

As the second order effects are assumed very small they are not included in the simulation model, and not further described.

4.2 Single degree of freedom equations of motion

The matrices which goes into the equations of motion are built up by the contribution in all six DOF, and the matrices can be very complex. By studying the different DOF separately we can identify which DOF are dominant, and what kinds of motions are critical for the mooring system.

For a mooring system the top end motions need to be identified. The top end motions are the floating structure motions, and to control these motions are essential for designing a safe mooring system.

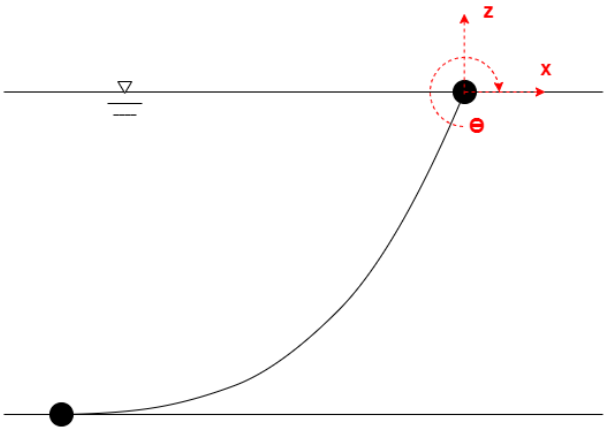

Figure 4.4: Top end motions

Figure 4.4 shows a two-dimensional view of a catenary mooring line. The top end motions are impacted by surge (x), heave (z) and pitch (θ), and these SDOF equations of motion are studied in the following sections.

For a cylindrical floating wind turbine the DOFs roll and pitch, and surge and sway will have the same system properties, but not the same excitation forces due to the mooring systems configuration of the mooring lines. Yaw is the only DOF which will not have a major contribution to the top end motion. This is because yaw motions have no effect on the vertical motions, and the angle of yaw is limited by the horizontal geometric stiffness of the mooring lines.

By studying these single degree of freedom contributions, we can understand the top end motions and also how to control these motions. For the rest of this section SDOF equations are studied. The acceleration, velocity and position vector used in Equation 4.1 containing the components in all DOF, are for SDOF systems represented as acceleration $\ddot{x}$, velocity $\dot{x}$ and position x. The equation of motion for a SDOF can then be generally written as:

$$(m + a(\omega))\ddot{x} + c(\omega)\dot{x} + d_l\dot{x} + d_q|\dot{x}|\dot{x} + k(r)r = q_{exc} \tag{4.7}$$

Where e_{exc} is the excitation force.

4.2.1 Surge, η_1:

The stiffness in surge is controlled by the mooring system. The natural period in surge can be found as:

$$T_n = 2\pi\sqrt{\frac{M + A}{K_{e,\eta_1}}} \tag{4.8}$$

Where M is the mass of the structure, A is the added mass, and K_{e,η_1} is the elastic stiffness of the mooring lines. Figure 4.5 shows how the natural period in surge is defined as a body with mass $M + A$ which is constrained by a spring with stiffness K.

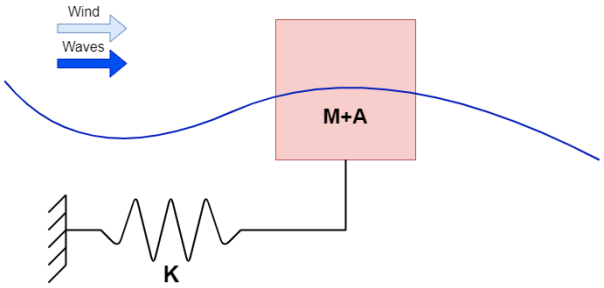

Figure 4.5: Stiffness in surge

The stiffness in surge for the floating structure are dependent on the mass, added mass and the wave period. As seen in Figure 4.5 the stiffness can be modelled as a spring connected to the floating structure. With a large mass and added mass, the stiffness will be large.

Added mass is an important contribution to the mass for submerged structures. Added mass can be considered as the inertia added to the system as the water particles are forced to accelerate around the structure. The added mass are calculated using analytical software as WAMIT, which calculates the added mass using potential theory. This is described in Chapter 9.

4.2.2 Heave, η_3:

The stiffness in heave are calculated using the simple Equation 4.9. Using only the waterline area of the structure, gravity and the density of seawater, the stiffness can be calculated. As seen in Equation 4.9, the stiffness is dependent on the hydrostatic properties of the FWT, and not the mooring lines.

Heave, η_3:

$$K_{e,\eta_3} = \rho g A \tag{4.9}$$

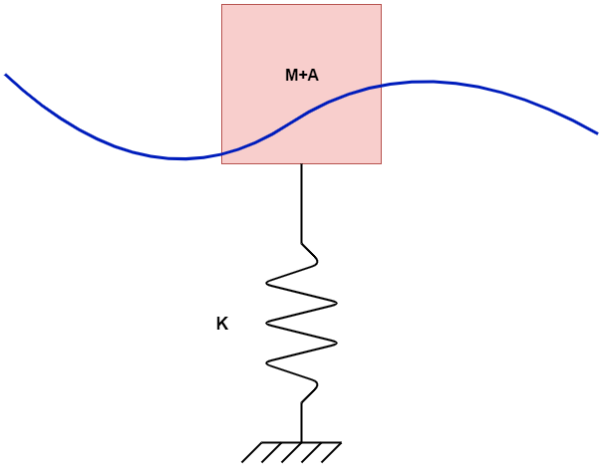

Figure 4.6: Stiffness in heave

4.2.3 Pitch, η_5:

The structure's stiffness in pitch is also easily calculated using the volumetric displacement, gravity, density of seawater and the distance GM.

Pitch, η_5:

$$K_{e,\eta_5} = \rho g \nabla \overline{GM} \tag{4.10}$$

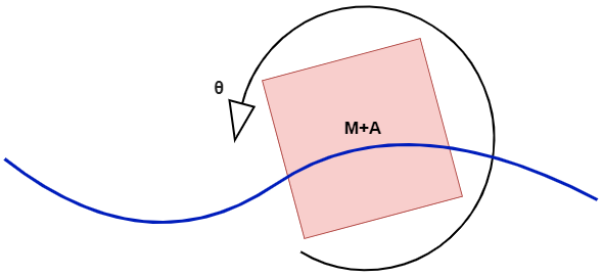

Figure 4.7: Stiffness in pitch

Also pitch stiffness is not affected by the mooring lines.

4.2.4 Resonance

The most important physical phenomenon that we need to avoid is resonance. This phenomenon occurs when the excitation force frequency coincides with the natural frequency of the system. This means that the response will get much larger than for other frequencies that are affecting the system. The natural frequencies of the system in all DOF must be identified to be able to design the mooring system in a safe manner.

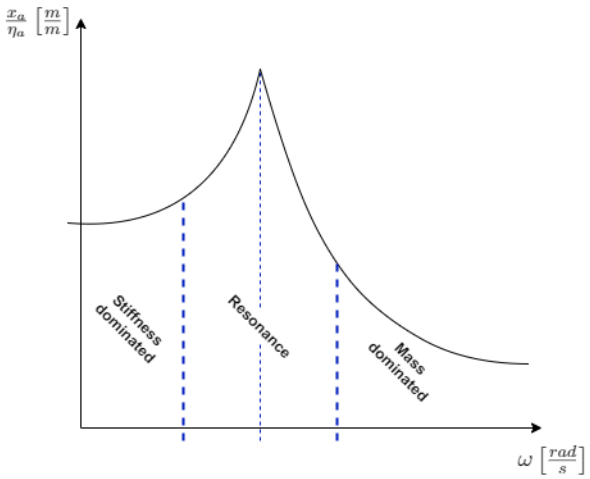

Figure 4.8: Dynamic amplification factor

Figure 4.8 show the dynamic amplification factor (DAF) of the a system. The DAF shows how the amplitude the motions for a structure can be amplified depending on the frequency of the excitation loads.

The first regime in the DAF figure is stiffness dominated, meaning that the excitation forces are in equilibrium and are absorbed by the stiffness in the system. The resonance regime is where the excitation frequency coincides with the natural frequency of the system. The damping of the system governs the displacement in this regime. The third regime is mass dominated. Here, the excitation frequency is so large that the system will not be able to respond to the forces, and the mass inertia of the structure will govern the displacements.

4.3 Damping

Damping is the processes that dissipates energy from the oscillating system. It is generally difficult to accurately calculate the damping of the system.

But its very important to be able to identify which effects and excitation's that have a damping effect. For FWTs the dominant damping forces will come from the current, wind and mooring lines.

As seen in the Equation 4.5 current forces will have a negative contribution to the excitation forces when the current velocity is larger than the FWT velocity. This is a linear low-frequency damping term.

A similar linear low-frequency damping term comes from the wind forces seen in Equation 4.3.

Due to wave-frequency motions on the FWT, drag forces will act on the mooring lines.

Drag forces are seen in Equation 4.6 in the second term. Drag forces act in the opposite direction of the motion. Hence, the drag force on the mooring lines will give a contribution to the total damping. As seen in the drag force equation, the drag force is velocity squared. The drag forces will therefore give a quadratic contribution the damping.

As seen in Equation 4.1, the damping consists of a linear damping matrix and a quadratic damping matrix. The terms presented above are dependent on velocities. But there are some of the damping terms that are dependent on quadratic velocity. We therefore separate linear and quadratic terms in two different matrices.

Viscous damping as skin friction and flow separation are also contributing to the total damping. These terms are harder to calculate and are small compared to damping due to wind, current and mooring lines. These effects are neglected.

Chapter 5

SIMA Software

The simulations of the floating wind turbine in this thesis is done using SIMA. This is a computer workbench created by DNV-GL and Sintef Ocean. SIMA are widely used in the marine industry to analyse marine operations e.g lifting and towing, and the dynamic response of slender systems e.g risers and mooring lines.

SIMA uses different integrated computer programs to analyse the different scenarios. SIMO is an abbreviation of Simulation of Marine Operations, and is used to analyse large volume body motions like the response in the FWT. While RIFLEX is used to analyse slender structures using the finite element method. Flexible risers, mooring lines and other slender structures are analysed using RIFLEX.

To be able to interpret the results, and to give accurate input to SIMA, it is important to understand the underlying mathematical formulations and methods. This chapter will therefore study the theory used in this software using the SIMO Theory manual, SINTEF-Ocean (2019).

5.1 SIMO

SIMO solves the Equations of Motion, ref. Equation 4.1, in the time domain. To solve the equation of motion in time domain, the frequency dependent terms $A(\omega)$ and $C(\omega)$ must be transformed to the time domain. SIMO can do this either by separation of motion or by using a convolution integral.

5.1.1 Separation of motion

As seen in Chapter 4 the low-frequency excitation forces comes from wind, current and second order wave drift forces. While the wave-frequency excitation comes from first order wave forces. Separating the motion into low-frequency and wave-frequency motions we get:

$$x = x_{WF} + x_{LF} \tag{5.1}$$

Where x_{WF} is the wave frequency motion and x_{LF} is the low-frequency motion.

By separating the WF and LF contributions into separate equations of motions, the WF forces can be calculated in the frequency domain.

$$(m + A(\omega)) \cdot \ddot{x}_{WF} + (C(\omega) + D_l) \cdot \dot{x}_{WF} + K \cdot x_{WF} = q^1_{wa}(\omega) \tag{5.2}$$

The WF motions can then be found by using the inverse Fast Fourier Transform (FFT) of:

$$x_{WF}(\omega) = (-\omega^2(m + A(\omega)) + i\omega(C(\omega) + D_l) + K^{-1})H^1(\omega) \cdot \zeta_a(\omega) \tag{5.3}$$

Where $H^1(\omega)$ is the first order transfer function between excitation force and wave elevation, and $x_{WF}(\omega)$ is the first order transfer function between motion and wave elevation.

The LF equation of motion in time domain becomes:

$$(m+A(\omega=0))\cdot\ddot{x}_{LF}+D_l\cdot\dot{x}_{LF}+D_q\cdot\dot{x}_{LF}|\dot{x}_{LF}|+K(x_{LF})\cdot x_{LF} = q_{cu}+q_{wi}(t)+q^2_{wa}(t) \tag{5.4}$$

Solving the above equation for x_{LF} the total motion is found.

5.1.2 Convolution integral

Total motion can also be found by using a convolution integral. The frequency dependent terms can are written as:

$$\underbrace{A(\omega) \cdot \ddot{x} + C(\omega) \cdot \dot{x}}_{f(t)} = q(t, x, \dot{x}) - D_l\dot{x} - D_q\dot{x}|\dot{x}| - K \cdot x - M \cdot \ddot{x} \tag{5.5}$$

The frequency dependent terms are to be identified in the time domain. $f(t)$ in the frequency domain is written as:

$$F(\omega) = (-\omega^2 A(\omega) + i\omega C(\omega)X(\omega)) \tag{5.6}$$

Where $X(\omega)$ is the frequency dependent response.

$$X(\omega) = \frac{1}{2\pi}\int_{-\infty}^{\infty} x(t)e^{i\omega t}dt \tag{5.7}$$

The integral from negative infinity to infinity is not relevant for a time domain analysis due to the fact that at $t = 0$ is the start of the simulation. For $t < 0$ all values will be equal to 0. The limits of the integral is therefore changed to 0 to t.

$h(\tau)$ is the retardation function. The retardation function can be found from both frequency dependent terms in the equation of motion.

$$h(\tau) = -\frac{2}{\pi}\int_0^{\infty} \omega a(\omega)sin(\omega t)d\omega = \frac{2}{\pi}\int_0^{\infty} c(\omega)cos(\omega t)d\omega \tag{5.8}$$

Frequency dependent added mass and potential damping can be written as:

$$A(\omega) = A_\infty + a(\omega) \tag{5.9}$$

$$C(\omega) = C_\infty + c(\omega) \tag{5.10}$$

Where A_{inf} is the added mass at infinite frequency and C_{inf} is the damping at infinite frequency.

Inserting these relations into the frequency dependent equation of motion, we get:

$$-\omega^2 A_\infty X(\omega) + (i\omega A(\omega) + c(\omega)) \cdot i\omega X(\omega) = F(\omega) \tag{5.11}$$

Taking the inverse FFT of the equation above, the frequency dependent terms can be written in time domain as:

$$A_\infty \ddot{x}(t) + \int_0^t h(t-\tau)\dot{x}(\tau)d\tau = f(t) \tag{5.12}$$

Inserting Equation 5.12 into Equation 5.5, the total convolution integral is:

$$A_\infty \ddot{x}(t) + D_l\dot{x} + D_q\dot{x}|\dot{x}| + K(x) \cdot x + M\ddot{x} + \int_0^t h(t-\tau)\dot{x}(\tau)d\tau = q(t, x, \dot{x}) \tag{5.13}$$

SIMO can solve the integral in Equation 5.13 using several different methods, but in this report the Newmark-Beta method is used.

5.2 RIFLEX

RIFLEX was developed to analyse riser systems and other slender structure systems. The total motions which have been calculated in SIMO are imported to RIFLEX as top end motions on the mooring system. RIFLEX then uses finite element method to calculate the response on the mooring lines based on the forces acting on a discretized model of the mooring lines. RIFLEX then calculates the total dynamic line tensions.

5.3 Coupled Analysis

The simulations of the FWT and mooring system can be numerically calculated in SIMA using two different approaches. One approach is to do an uncoupled analysis where SIMO calculates the FWT motions, then the SIMO results are imported to RIFLEX to analyse the mooring line tensions. However, this approach will not consider the change in system stiffness matrix $\mathbf{K}$ when the SIMO analysis is performed. The total stiffness of the system will change as the body moves as the mooring lines will change configuration and resist the motions of the structure.

In this thesis a coupled analysis are performed. Meaning that both SIMO and RIFLEX are simultaneously analysing the FWT and mooring system. For each time step the SIMO results are imported to RIFLEX and the mooring lines response and stresses are calculated, and the stiffness matrix will then also change for each time step.

In order to perform a coupled analysis, the convolution integral approach are needed. Then the large volume SIMO body, and the slender RIFLEX model are coupled through retardation functions.

Since the equation of motions are calculated for each time step, the accuracy of the results are dependent on the size of the time steps. This parameter is input from the user of SIMO.

Chapter 6

Rules and Regulations

In the following chapter the rules and regulations used in this report are described. The FWT are designed according to the classification society DNV-GLs standard on floating wind turbine structures, and its offshore standard on position mooring. These standards state the design limits which the FWT should be tested for, and the application limitations given by the society.

The following sections state and discuss various design limits stated in DNVGL-ST-0119 and DNVGL-OS-E301.

6.1 DNVGL-ST-0119: Floating wind turbine structures

This standard provides guidance, technical requirements and principles for design of structures and its station keeping design for floating wind turbines.

Initially in the offshore standard two consequence classes are presented. These consequence classes are two different design parameters which consider the consequence of failure of the structure. Consequence class 1 is where failure is unlikely to lead to unacceptable consequences such as loss of life. As a FWT will be unmanned during severe weather conditions, consequence class 1 is suitable and will be used in this thesis.

In DNVGL-ST-0119 ultimate limit state (ULS) design shall be based on the 50-year return period for waves and wind, while the current shall have a 10-year return period.

Important sections from DNVGL-ST-0119 relevant for the mooring design in this thesis are highlighted below. All sections are taken from chapter 8 Station Keeping in the standard.

Restrained floaters - general

When fibre rope are subjected to permanent tensile loads, time-dependent elongation due to creep will occur. This will cause the fibre rope to have a softer tension-strain characteristic than the unloaded fibre rope. This issue should be addressed during the design of a mooring system using fibre rope.

In an internal Equinor memo written by Larsen (2018), a proposed model of the axial stiffness of polyester ropes based on full scale testing is presented. This memo addresses this issue regarding creep and a principle tension-strain curve for polyester ropes called "SyROPE" can be seen in Figure 6.1.

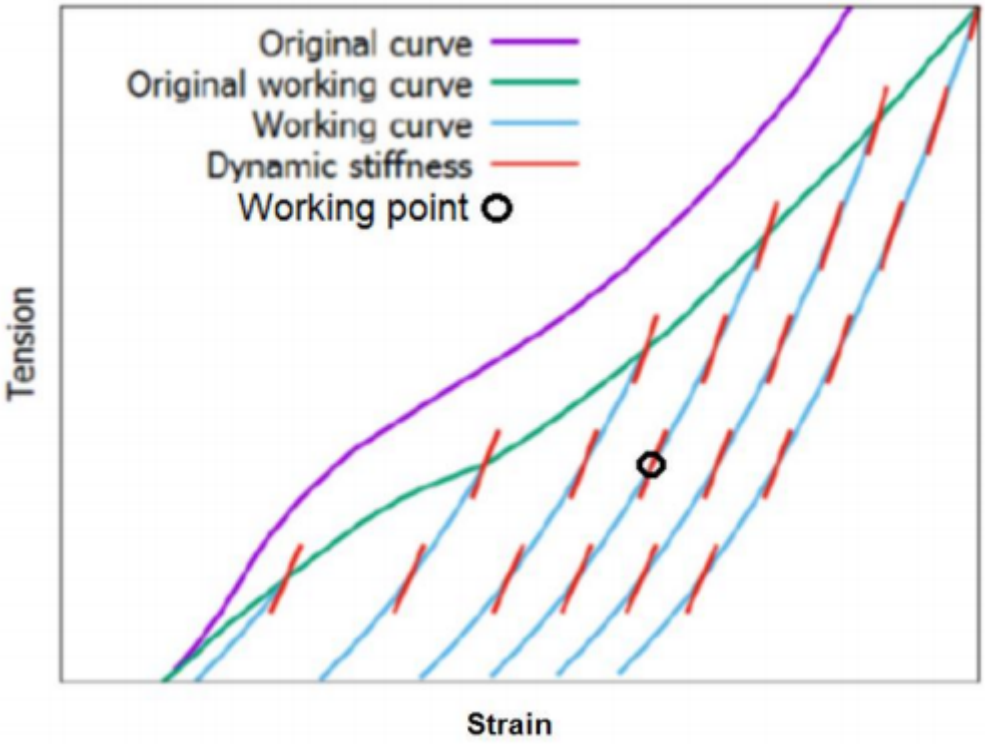

Figure 6.1: Principle tension-strain curve from Larsen (2018).

In Figure 6.1 the original curve shows a tension-strain characteristics for a new rope during its first, quick loading. The original working curve shows the stationary working curve for a polyester rope which is subjected to its historical highest tension after the permanent strain has been taken out after some time.

The blue working curve is the static elastic stiffness of the polyester rope when subjected to a mean tension lower than the original working curve. The working curve is a downwards working curve, while the original working curve is an upwards working curve. During cyclic tension the shape of the tension-strain relationship will form a hysteresis curve.

More detailed polyester characteristics and how it is accounted for in the modelling in

SIMA is discussed in later sections.

Ultimate loads

Each mooring line should be designed according to the following formula:

$$T_d = \gamma_{mean} \cdot T_{c,mean} + \gamma_{dyn} \cdot T_{c,dyn} \tag{6.1}$$

This is the design tension, T_d, of which the most loaded mooring line in a 50-year storm should be designed after. Here, γ_{mean} and γ_{dyn} are two load factors of the mean and dynamic tension. These factors are dependent on which consequence class the floating structure complies with. $T_{c,mean}$ is the characteristic mean tension and it is defined as the mean tension of a 50-year value of the line tension caused by wind, waves and current. $T_{c,dyn}$ is the characteristic dynamic tension and is defined as the dynamic part of the 50-year value.

The load factors for consequence class 1 is:

Table 6.1: Load factors in consequence class 1 from DNGL-ST-0119

Load factors in consequence class 1	
γ_{mean}	1.3
γ_{dyn}	1.75

A number of sea trials with the present sea states defined by Hs, Tp and U_{ref} must be investigated to determine the highest value of the characteristic mean and dynamic tensions.

Because of the FWT properties, the largest mooring line tension may not occur during the 50-year contour, but during the rated wind speed. This produces the largest thrust force on the rotor on the FWT, and must be investigated if this environmental condition causes a higher mooring line load than the 50-year value.

Resistance

This section describes the characteristic capacity requirements of the mooring lines. The characteristic capacity shall be calculated based on the following equation:

$$S_c = \mu_s \cdot (1 - COV_s \cdot (3 - 6 \cdot COV_s)); COV_s < 0.10 \tag{6.2}$$

Where μ_s is the mean value of the breaking strength of the mooring line and COV_s is the coefficient of variation of the breaking strength of the component.

If μ_s and COV_s is not available, the characteristic capacity may be obtained by the

minimum breaking load MBL according to the following equation:

$$S_c = 0.95 \cdot MBL \tag{6.3}$$

Design Criterion

In the ultimate limit state (ULS) the design criterion is as follows:

$$S_c > T_d \tag{6.4}$$

6.2 DNVGL-OS-E301: Position mooring

This standard has been widely used as standard for mooring systems and station keeping by the O&G industry. This section describes the most important rules and guidelines applicable for mooring semi-submersible. Chapters from DNVGL-OS-E301 are described and discussed in the following sections.

Environmental conditions and loads

Detailed metocean data should be developed for long-term mooring. Metocean Design Basis, Equinor (2016), for the Snorre field is available and used for this thesis.

The NPD/ISO wind spectrum shall be applied for all locations. This wind spectrum and the application of the spectrum is further explained in Chapter 9.

DNVGL-OS-E301 also states that column-stabilised units which are directionally fixed, the loads from wind, waves and current are assumed acting in the same direction. This thesis will use co-linear environmental loads acting parallel to one mooring line. This will yield the highest mooring line tensions.

Forces acting on the mooring lines is also included in the model. These forces are dominated by drag forces from the current. The drag coefficients for different mooring lines are given in the standard. Drag coefficients for the relevant mooring lines are presented in Table 6.2.

Table 6.2: Drag coefficients given in DNVGL-OS-E301, DNV-GL (2015).

Drag coefficients for different mooring lines		
Mooring component	Transverse	Longitudinal
Stud less chain	2.4	1.15
Spiral rope without plastic sheating	1.6	-
Fibre rope	1.6	-

Mooring system analysis

It is stated that the required extreme value of the line tension shall be estimated as the most probable maximum (MPM) value of the extreme value distribution. For time domain analyses one long simulation can be substituted by simulating several (10-20) realisations of 3-hour simulations. From these realisations an extreme value distribution shall be established to find the MPM. An alternative to finding the MPM from the Gumbel distribution is to use Equation 6.5.

$$MPM = \mu - 0.45 \cdot \sigma \tag{6.5}$$

where μ is the mean of the peaks, and σ is the standard deviation of the peaks.

This concludes the excerpts taken from the two standards provided by DNV-GL. The rules and regulations stated above are only partial of the whole standard, and some guidelines from the standard are used for the simulations, but not stated in this chapter.

Chapter 7

Environmental Conditions

This chapter discusses the environmental loads acting on the FWT. These loads are calculated based on the Metocean Design Basis for the Snorre Field, provided by Equinor (2016). This is the location where the FWT project Hywind Tampen, launched by Equinor, is to be placed. As discussed in Chapter 6 the environmental loads should have return periods of 50-years for wind and waves and a return period of 10-years for the current.

Metocean Design Basis was first issued in 1998 and has been revised eight times to present day. This thesis uses the last revision of the document.

Since the forces acting on the FWT is highly dependent on the wind velocity the thrust curve for the 10 MW turbine seen in Figure 4.2 is used to determine which weather conditions which must be studied.

From the thrust curve it is obvious that the rated wind speed where the rotor thrust is at its maximum is a critical weather condition which must be studied. Also the cut-off wind speed at 25 m/s where the blades are feathered and the rotor is parked is also a interesting weather condition. By also analysing the 50-year storm, the three weather conditions most interesting to this thesis has been found.

This thesis will refer to the three different weather conditions as regimes from now on.

- **Regime I:** Rated wind speed, 0-11.4 m/s at hub height
- **Regime II:** Cut-off wind speed, 11.4-25 m/s at hub height
- **Regime III:** 50-year storm

In the following sections the environmental loads in the three regimes are calculated based on the Metocean design basis.

7.1 Regime I: Rated wind speed

As seen in Figure 4.2 the thrust force acting on the 10MW FWT reaches its maximum at the wind speed of 11.4 m/s at the rotor hub. This is called the rated wind speed of the FWT. SIMA uses the wind velocity at the reference height of 10 metres above sea water level as input, so the wind speed must be adjusted to the reference height. Using Equation 10.4, the wind velocity at the reference height is calculated from rated wind speed at hub.

The wind velocity at reference height is also used to calculate the sea state at the given wind velocity. Using the distribution seen in Figure A.1 in A, which show the observed and fitted 1-hour wind speed averages in Metocean Design Basis, the probability of non-exceedance for the rated wind speed can be established. This probability of non-exceedance for the wind velocity is used to find the corresponding sea state.

The probability of non-exceedance distribution for significant wave height is found in the Metocean Design Basis and can be seen in Figure A.2 in Appendix A. Using the same probability of non-exceedance found for the wind velocity above, the corresponding significant wave height is graphically found.

In Metocean Design Basis the corresponding peak periods Tp for the significant wave height is plotted with the contour lines of different return periods in the same plot. This plot is seen in Figure 7.1. It is clear that the peak periods have a large scatter for a given significant wave height. The mean peak period for the given significant wave height is used in this thesis.

The current at the Snorre field is measured at different water depths. The current is assumed to be constant for different sea states in this thesis, hence all three regimes will have the same current velocity.

The different current velocities for the water depths are found are used as input to SIMA. Current forces are important on the mean drift of the FWT, but the current forces acting on the mooring lines are of little importance, current velocities at water depths beneath the substructure are therefore not stated below.

Table 7.1: Environmental condition in regime I

Regime I	
U_{hub} [m/s]	11.4
U_{ref} [m/s]	8.68
H_S [m]	2.4
T_P [s]	9.6
$u_{z=0}$ [m/s]	1.23
$u_{z=20}$ [m/s]	1.04

7.2 Regime II: Cut-off wind speed

Environmental loads for regime II is calculated using the same procedure as for regime I. The wind velocity is found in the thrust curve seen in Figure 4.2, then the wind velocity at the reference height is found.

Following the same procedure, and remembering that the current velocity is constant in all three regimes the environmental loads in regime II is summarised in Table 7.2.

Table 7.2: Environmental condition in regime II

Regime II	
U_{hub} [m/s]	25
U_{ref} [m/s]	19.04
H_S [m]	6.8
T_P [s]	12.8
$u_{z=0}$ [m/s]	1.23
$u_{z=20}$ [m/s]	1.04

7.3 Regime III: 50-year storm

In the Metocean Design Basis, values corresponding to return periods of 1-year, 10-years, 100-years and 1000-years are presented. To find the 50-year values for wind and waves, the probability of non-exceedance for a 50-year storm is found by using the following relationship:

$$P_{50} = 1 - \frac{1}{N_{50}} \tag{7.1}$$

where N_{50} is the number of observations during a 50-year period assuming that there is one observation per a 3-hour realisation.

$$N_{50} = \frac{1obs}{3hours} \cdot \frac{24hours}{day} \cdot \frac{365days}{year} \cdot 50years \tag{7.2}$$

Using P_{50} as the probability of non-exceedance for the 50-year value, the wind speed at the reference height can be found by using Figure A.1 in Appendix A. Using Equation 10.4 the wind speed at the rotor hub can be found from the wind profile used in the ISO-19901-1 wind spectrum.

The same procedure as for the other two regimes can now be used to find the corresponding significant wave height and peak period values for the 50-year storm. The values for the environmental condition in regime III is presented in Table 7.3.

Table 7.3: Environmental condition in regime III

Regime III	
U_{hub} [m/s]	44.7
U_{ref} [m/s]	34
H_S [m]	15
T_P [s]	16.7
$u_{z=0}$ [m/s]	1.23
$u_{z=20}$ [m/s]	1.04

7.4 Summary of environmental conditions

Table 7.4 shows the calculated values of significant wave height, mean peak period and wind velocities at the reference height and at the rotor hub for each regime. All of these regimes must be analysed to be able to identify which of these regimes will introduce the largest load on the mooring lines.

Table 7.4: Summary of environmental conditions based on Metocean Design Basis Snorre Field, Equinor (2016).

Regime	U_{hub} [m/s]	U_{ref} [m/s]	H_S [m]	T_P [s]
I	11.4	8.68	2.4	9.6
II	25	19.04	6.8	12.8
III	44.7	34	15	16.7

Seen in Figure 7.1 taken from Equinor (2016), the contour plots of different return periods are shown. The 50-year values of significant wave height and mean peak period calculated above can be found just inside of the light blue curve which is the contour line of a 100-year return period.

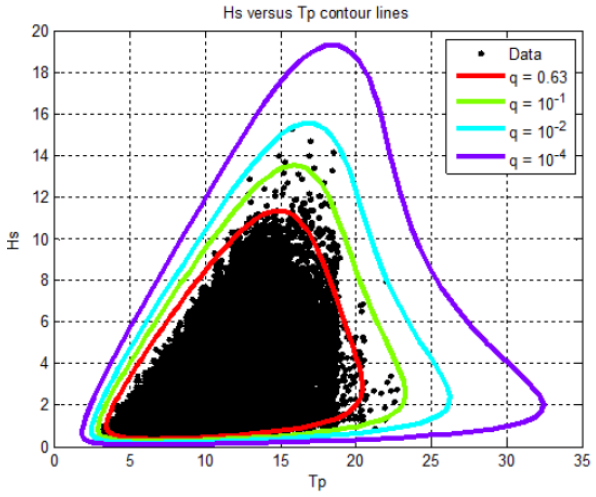

Figure 7.1: Hs versus Tp contour lines from Equinor (2016).

Chapter 8

Mooring Concepts

This chapter discusses the different mooring concepts that are modelled and will be analysed in SIMA. This thesis will use the same environmental conditions as Hywind Tampen. All mooring concepts will also have the same anchor placement and be modelled to have approximately the same pretension as is planned on the Hywind Tampen project.

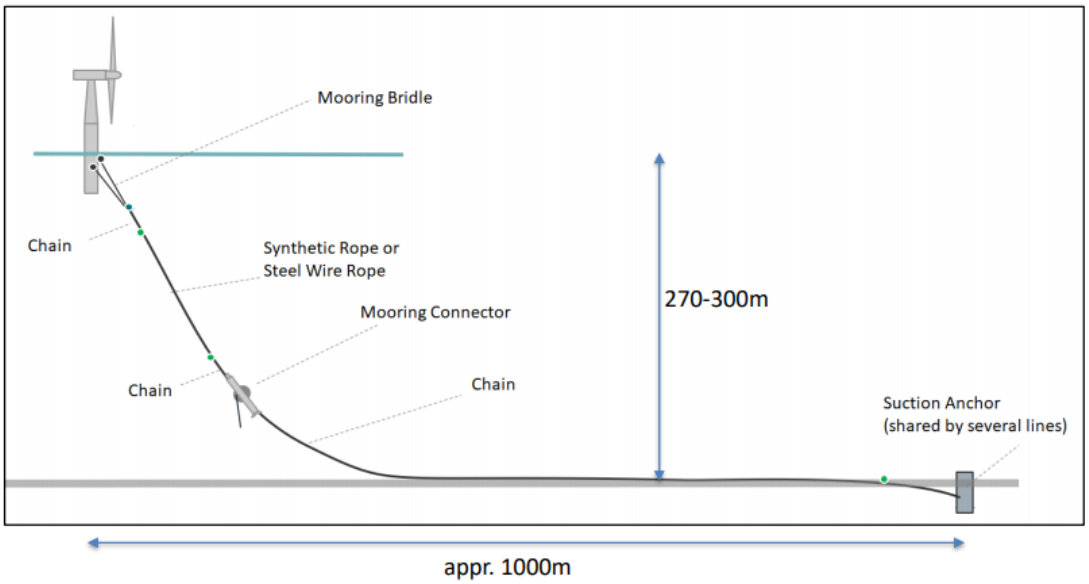

Figure 8.1: Layout of Hywind Tampen, Larsen (2020b)

As previously stated, this thesis will use the same location as Hywind Tampen. The area where Hywind Tampen is to be built has a water depth between 270-300 metres. This thesis will assume a constant water depth of 270 metres. Figure 8.1 shows an approximate layout drawing of how the Hywind Tampen mooring system will be, Larsen (2020b). The mooring bridle will be connected 15 metres below sea water level. This thesis will use the same draught for the connection of the mooring line to the substructure, but a mooring bridle is not necessary for this thesis because the CSC 10 MW are a semi-submersible

and not a spar. Figure 8.1 also show the distance from the centre of the FWT to the suction anchor which also will be used for all mooring concepts. The pretension is chosen based on the pretension designed for Hywind Tampen.

Table 8.1: Constant values for all mooring concepts

Constants for all mooring concepts	
Water depth	270 m
Draught to mooring line connection	15 m
Pretension	$\approx$ 1500 kN
Horizontal distance to anchor	1000 m

8.1 Chain-Wire-Chain - CWC

This system will use conventional chain and steel rope, and will be based both on the existing mooring system of Hywind Scotland and the planned mooring system of Hywind Tampen. According to Equinor (2014) Hywind Scotland uses R4S grade stud-less chains with a diameter of 147 mm.

Seen in Figure 8.1 Hywind Tampen will use wire or synthetic rope in the middle section of the mooring line instead of using chain. Using the hardware catalogues provided by Ramnæs (2015) for chain properties and Bridon (2020) for the steel rope properties, the applicable chain and steel rope can be chosen.

Table 8.2: Chain properties developed by Ramnæs (2015) and steel rope properties developed by Bridon (2020).

	Chain	**Steel rope**
Type	R4S	Spiral strand
MBL	21179 kN	22200 kN
Diameter	147 mm	155 mm
Mass in air	432 kg/m	133 kg/m
Axial stiffness	1.73E+06 kN	2.14E+06 kN

Knowing the desired pretension and anchor placement, the initial mooring line length was to be decided. Since the CWC system uses segments of both chain and steel rope, the catenary equations was not suitable to finding the correct line length. Instead the line lengths were found through iterations in SIMA.

The total line length was found to be 1050 metres, with 150 metres of this being steel rope. This resulted in a pretension of 1434 kN and a static line configuration as seen in Figure 8.2:

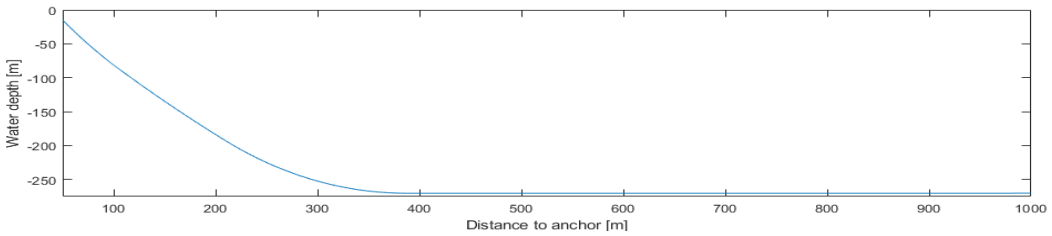

Figure 8.2: Static XZ-configuration of the CWC system.

8.2 Chain-Polyester-Chain Taut mooring - CPC-T

This concept uses 30 metres of chains both at the mooring line connection point to the CSC and to the anchor. The rest of the mooring line is polyester rope. Top and bottom of a mooring line is prone to friction against the substructure and against the anchor, hence the chains are used in these areas as they are able to withstand the wear and tear.

The chains used in this concept are the same as used in the CWC system. The polyester mooring lines are modelled based on the Superline Polyester developed by Bridon (2013). Based on the MBL of the chains the polyester mooring line dimension can be chosen. In Table 8.3 the properties of the chain and polyester mooring lines chosen for this concept is shown:

Table 8.3: Chain properties developed by Ramnæs (2015) and polyester properties developed by Bridon (2013).

	Chain	**Polyester**
Type	R4S	Permanent mooring
MBL	21179 kN	22563 kN
Diameter	147 mm	286 mm
Mass in air	432 kg/m	52.6 kg/m
Axial stiffness	1.73E+06 kN	20· MBL

As described in Chapter 6 the modelling of synthetic fibre ropes are challenging as the mechanical properties of the fibre ropes change in time and after the fibre has been under axial stress. In the internal Equinor memo written by Larsen (2018), it is shown how a non-linear stiffness model compare to linear stiffness models. This plot is displayed in Figure 8.3.

Based on Figure 8.3 the axial stfess of the polyester mooring lines in this concept will be based on a linear stiffness model using $EA = 20 \cdot MBL$. This will give the system a high stiffness, and also a conservative approach of modelling.

As for the CWC system the mooring line length is found through iterations in SIMA. The pretension shall be approximately 1500 kN and the anchor placements are the same as before. This resulted in a mooring line length of 981 metres and a pretension of 1476 kN.

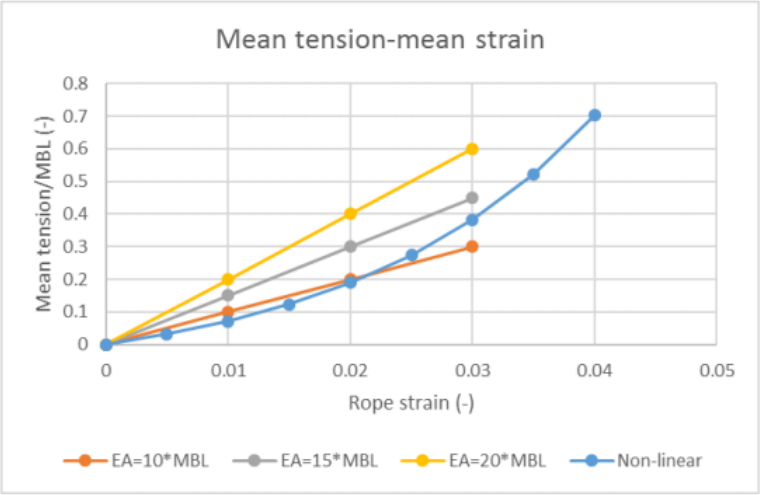

Figure 8.3: Linear and non-linear stiffness models of synthetic fibre ropes taken from Larsen (2018).

A static configuration of the mooring line is seen in Figure 8.4.

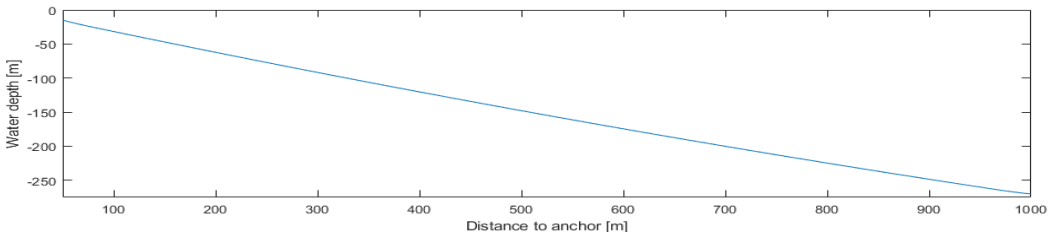

Figure 8.4: Static XZ-configuration of the CPC-T concept.

8.3 Chain-Polyester-Chain Buoy and Weight - CPC-BW

This mooring concept uses the exact same mooring line as for the CPC-T concept, but a clump weight and buoy are attached to the mooring line. The purpose of attaching a clump weight and buoy on the mooring line is to replicate a catenary system to add geometric stiffness to the total stiffness of the system.

A mooring system using a clump weight and buoy proposed by IFE (2020) is used as a starting point for modelling of the CPC-BW system. IFE (2020) used the following properties for their clump weight and buoy:

Table 8.4: Clump weight and buoy properties proposed by IFE (2020).

Buoy and clump weight properties	
Submerged clump weight mass	35 tonnes
Submerged buoy mass	2.5 tonnes
Volume buoy	$13m^3$
Connection distance of clump weight as fraction of water depth	93% water depth

The parameters given in Table 8.4 are used as input to SIMA. The buoy are modelled

with a volume of $13m^3$ which will impose forces on the buoy. The buoy is connected to the end of the polyester rope. The clump weight is modelled as a point mass connected at a length of 93% of the water depth which corresponds to 238 metres on the mooring line.

As for the other concepts the mooring line length if found through iterations in SIMA. The line length is set to 988 metres with the corresponding pretension of 1490 kN. The static mooring line configuration is seen in Figure 8.5.

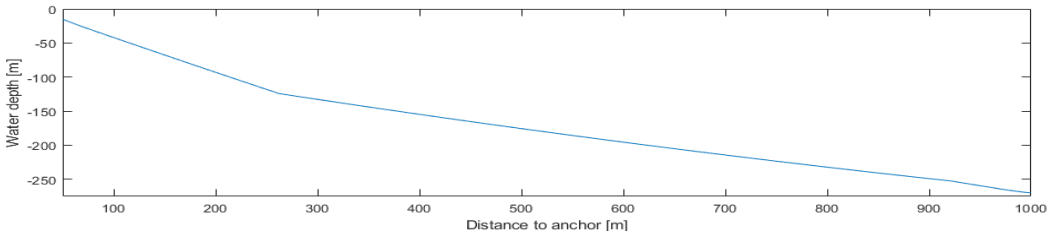

Figure 8.5: Static XZ-configuration of the CPC-BW concept.

8.4 Chain-Polyester-Chain Buoy and Weight, Non-Linear stiffness model - CPC-BW-NL

As stated when modelling the CPC-BW concept, the mooring lines were modelled with the assumed axial stiffness of 20·MBL. This is seen in Figure 8.3 to be a conservative assumption compared to the non-linear stiffness model.

A non-linear stiffness model proposed in Larsen (2018) is used. The non-linear stiffness model is seen in Equation 8.1:

$$\frac{T_{mean}}{MBL} = \frac{f}{g \cdot 100} \cdot [exp(g \cdot 100 \cdot \epsilon_{mean}) - 1] \tag{8.1}$$

where T_{mean} is the mean tension in the polyester and ϵ_{mean} is the mean strain. f and g are constants estimated from full scale testing. Larsen (2018) proposes to use $f = 5.5$ and $g = 0.5$ This gives the following non-linear tension strain relation:

$$\frac{T_{mean}}{MBL} = 0.11 \cdot [exp(50 \cdot \epsilon_{mean}) - 1] \tag{8.2}$$

The non-linear and linear stiffness models are seen in Figure 8.6 where $\frac{T_{mean}}{MBl}$ is plotted against mean strain.

Using the exact same mooring line configuration with buoy and clump weights attached as in the CPC-BW concept, the system is modelled in SIMA and the pretension and line length can be found. The pretension is 1323 kN and the line length is 986 metres.

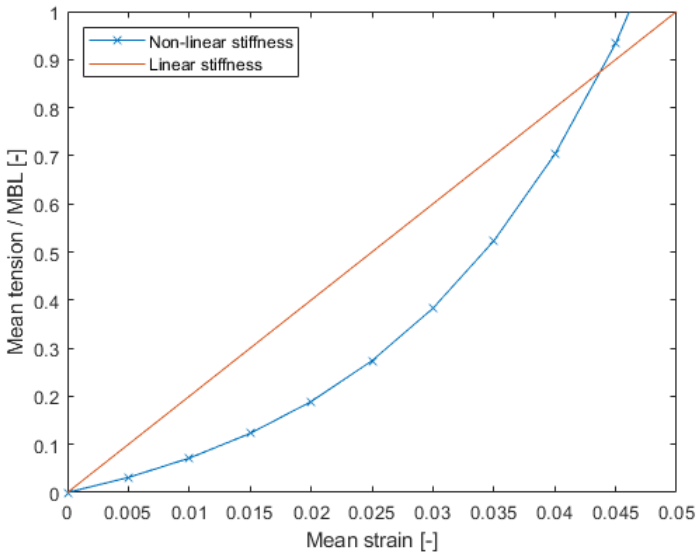

Figure 8.6: Linear and non-linear stiffness model

The static mooring line configuration for this system is almost identical to the CPC-BW concept, only difference is that the clump weight drags the mooring line further down.

8.5 Chain-Nylon-Chain - CNC-5-T

Instead of using polyester mooring lines, this concept uses nylon as the main mooring line segment. Keeping the 30 metres of chain at top and bottom as for the other synthetic mooring line systems. This system is a taut mooring system, like the CPC-T system. Nylon mooring lines will be modelled according to the linear stiffness model.

Before the mooring concepts using nylon was designed, the results from the time domain simulations from the CPC-T and CPC-BW system was analysed. The polyester mooring lines proved to be have been modelled with a too conservative MBL. The results showed that the largest value of design tension, T_d, for the very stiff mooring lines in the CPC-T concept only used 72% of the capacity of the mooring lines. And since the nylon systems are assumed to get lower tensions because nylon have a lower stiffness, it was decided to decrease the MBL of the nylon systems to $MBL = 15000kN$.

According to a study done by Huntley (2016) nylon ropes axial stiffness can be estimated as a factor of the MBL. This stiffness ranges from 4.7-14.3 times the MBL of the nylon according to Huntley (2016). This thesis chooses to do two different nylon systems where one stiffness is modelled as 5·MBL and the other system is modelled as 10·MBL.

The CNC-5-T concept is modelled with an axial stiffness equal to 5·MBL. Bridon (2013) delivers nylon mooring lines for short term mooring. Hence, the nylon mooring line dimensions need not be large as they shall not withstand high tensions. The largest

nylon mooring line in Bridon (2013) has a MBL of 11507 kN, which is not large enough for this concept. This thesis assumes that the nylon mooring lines can be up-scaled to have a larger MBL and be used for permanent mooring. Figure 8.7 shows the how the MBL is extrapolated from the values given in Bridon (2013).

The same extrapolation is done for the weight of the mooring lines. This extrapolation is seen in Figure 8.8. From Figure 8.7 and Figure 8.8 the nylon mooring lines which are used in this thesis have a diameter of 265 mm, a dry weight of 47.3 kg/m and a wet weight of 4.6 kg/m.

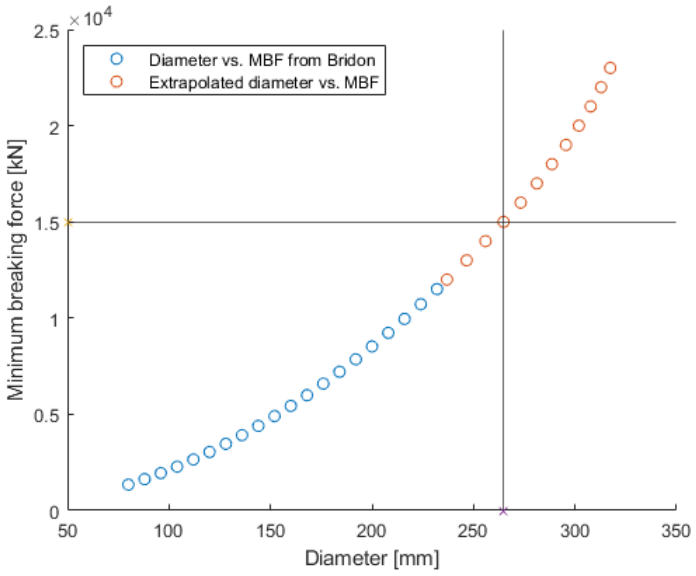

Figure 8.7: Extrapolation of nylon mooring line diameter developed by Bridon (2013).

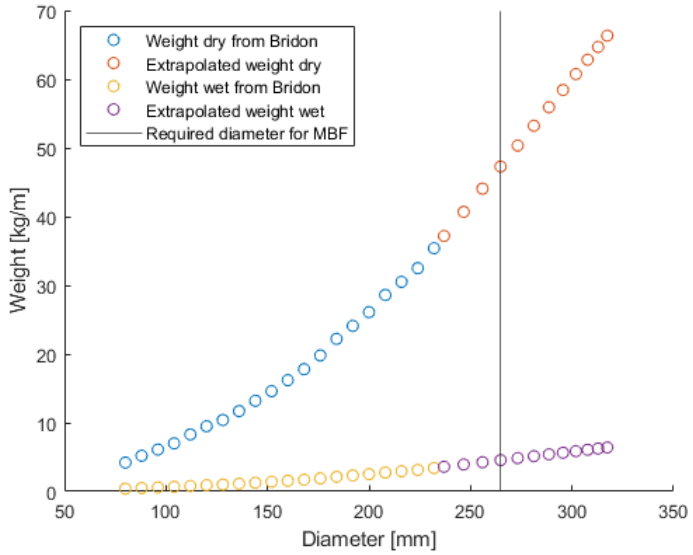

Figure 8.8: Extrapolation of nylon mooring line weight

The mooring line length and pretension is then to be found through iterations in SIMA. The line length is chosen to be 966 metres with a pretension of 1491 kN.

As for the CPC-T concept, the static mooring line configuration is almost a straight line from the CSC down to the anchor.

8.6 Chain-Nylon-Chain - CNC-10-T

This system is an exact replica of the CNC-5-T system, using the same mooring line properties. In this concept the axial stiffness of the nylon mooring line is set to be 10·MBL.

The same procedure as stated above of finding the line length and pretension are done also for this concept. The line length is chosen to be 975 metres with a pretension of 1445 kN.

8.7 Summary of all mooring concepts

Table 8.5: Summary of all mooring concepts initial design

Mooring system	$\frac{EA}{MBL}$	Pretension [kN]	Line length [m]	Buoy and weight
CWC	81.7	1434	1050	No
CPC-T	20	1476	981	No
CPC-BW	20	1490	988	Yes
CPC-BW-NL	Non-linear	1323	986	Yes
CNC-5-T	5	1491	966	No
CNC-10-T	10	1445	975	No

Chapter 9

CSC 10 MW Wind Turbine

This thesis will study different mooring deigns using the CSC semi-submersible developed by Wang (2014) as the floating structure. The semi-submersible proposed by Wang (2014) is one of many design iterations of the design initially proposed by Luan et al. (2018).

Wang (2014) designed his semi-submersible substructure to support the 10MW DTU reference turbine developed by Bak et al. (2013).

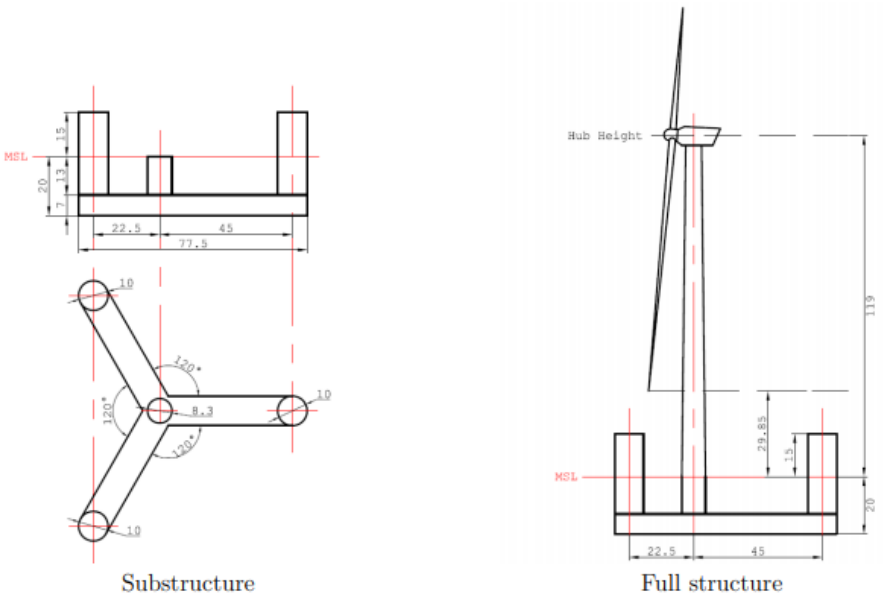

Figure 9.1: Geometry of the CSC10MW FWT

The geometry of the CSC 10 MW FWT is seen in Figure 9.1 and the main dimensions of the substructure proposed by Wang (2014) are listed in Table 9.1.

Table 9.1: Main dimension of CSC 10MW floating wind turbine proposed by Wang (2014).

Main dimensions [m]	CSC 10MW
Draft	20
Center column diameter	8.3
Tower base diameter	8.3
Tower top diameter	5.4
Hub height	119
Side column diameter	10
Side column distance to origo	45
Pontoon height	7
Pontoon width	10
Thickness	0.04

9.1 Kinetics

The kinetics give the body properties such as mass, added mass, hydrostatic stiffness and first order motion transfer functions.

9.1.1 Hydrostatic stiffness

Using Equations 4.9 and 4.10, the hydrostatic stiffness of the FWT in heave, pitch and roll can be found.

Heave:
The hydrostatic stiffness in heave are dependent of the cross-sectional area of the structure at seawater level, gravitational acceleration and the water density. The waterline area is calculated to $A_{wl} = 289.7m^2$.

The resulting hydrostatic stiffness in heave is then:

$$K_{e,\eta_3} = 2.91 \cdot 10^6 N/m \tag{9.1}$$

Pitch and roll:
As seen in Equation 4.10 the stiffness in pitch and roll are dependent on displaced volume and the metacentric height $\overline{GM}$, along with gravity and seawater density. The metacentric height can be calculated by:

$$GM = KB + BM + KG \tag{9.2}$$

where:

- KB: Distance from keel to centre of buoyancy of the submerged volume.

- BM: Distance from centre of buoyancy to the metacentre.
- KG: Distance from keel to centre of gravity of the structure.

The distance from the centre of buoyancy to the metacentric height, BM, is found by calculating the second moment of area around the axes lying in the water plane and dividing it by the displaced volume.

$$BM = \frac{I}{\nabla} \tag{9.3}$$

Due to symmetry the second moment of area around the x- and y-axis are identical, hence the metacentric height is also identical. Calculating the second moment of area around the x-axis for the waterline areas results in:

$$I_{x,tot} = 2.40 \cdot 10^5 m^4 \tag{9.4}$$

Having found all three terms in Equation 9.2, the metacentric height is calculated to be $GM = 9.40m$. And the hydrostatic stiffness in pitch and roll becomes:

$$K_{e,\eta_4} = K_{e,\eta_5} = 1.30 \cdot 10^9 Nm \tag{9.5}$$

The hydrostatic stiffness in heave, pitch and roll are then used as input to SIMA.

9.1.2 Added mass

Data regarding the infinite frequency added mass and frequency dependent added mass was provided by Associate Professor Erin Bachynski at the Institute for Marine Technology at NTNU. She has done the calculations using WADAM. This data was provided as an STASK-file which was imported to the simulation workspace and included in the model.

9.1.3 First order motion transfer functions

Associate Professor Erin Bachynski also provided the first order motion transfer functions for the model. The data was also obtained using WADAM which was included to the model.

The response amplitude operators (RAO) for surge, heave and pitch for the CSC is seen in Figure 9.2, Figure 9.3 and Figure 9.4.

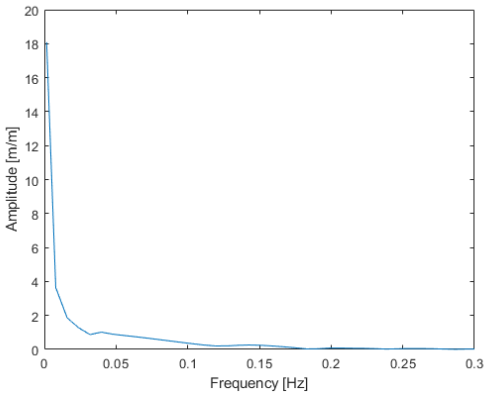

Figure 9.2: Surge RAO for the CSC. 0 degree heading.

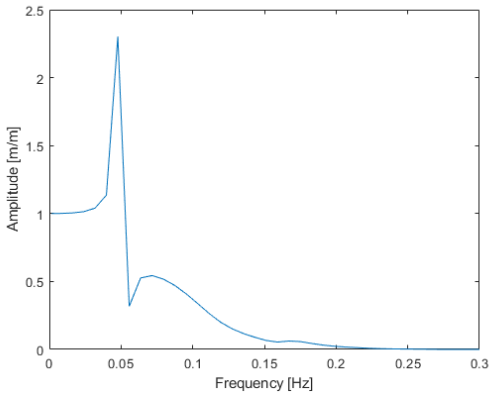

Figure 9.3: Heave RAO for the CSC. 0 degree heading.

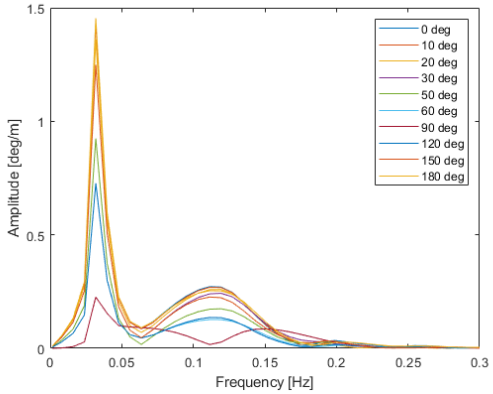

Figure 9.4: Pitch RAO for the CSC. Multiple headings.

9.2 Inertia

9.2.1 Mass

The model proposed by Wang (2014) is based on the design of a 5MW floating wind turbine, and was scaled up to support the DTU 10MW reference wind turbine developed by Bak et al. (2013). This thesis uses the masses and geometry proposed by Wang (2014) for the 10MW wind turbine, and the mass of the different components are given in Table 9.2.

The total mass of 3893 tonnes is not enough mass to get the desired draft of 20 metres. Buoyancy calculations for the floater with 20 metres draft are proposed by Wang (2014) and is shown in Table 9.3.

The total mass is $m_{steel} + m_{ballast}$, hence the mass of the ballast is equal to 10188 tonnes, which becomes $9940m^3$. As described by Wang (2014), the pontoons have available space for $9770m^3$ of ballast water. This leaves $170m^3$ which are needed to get the correct draft, but Wang (2014) excluded this from the model for two reasons:

Table 9.2: Mass of structural components proposed by Wang (2014).

	Component	Mass [tonnes]	x [m]	y [m]	z [m]
	Rotor	230	-7.1	0	119
	Nacelle	446	2.7	0	121.5
	Tower	628	0	0	47.6
Wind Turbine	**SUM**	**1305**	**-0.3**	**0**	**85.5**
	Columns	1005	0	0	1.2
	Pontoons	1583	0	0	-16.5
Semi	**SUM**	**2588**	**0**	**0**	**-9.6**
Total	**Total**	**3893**	**-0.1**	**0**	**22.3**

Table 9.3: Buoyancy calculations proposed by Wang (2014)

Buoyancy	Displacement [tonnes]	x[m]	y[m]	z[m]
Center column	721	0	0	-6.5
Side columns	3140	0	0	-6.5
Pontoons	10221	0	0	-16.5
Total	14081	0	0	-13.8

- Buoyancy error is 1.7% and this is an acceptable error for initial design.
- Weight of mooring lines are not included in the initial model, and therefore the mooring lines would contribute to a larger weight during mooring analysis.

This thesis also neglect the remaining $170m^3$.

A summary of the mass properties are presented in Table 9.4.

Table 9.4: Summary of mass and centre of gravity of CSC 10MW

	Mass [t]	COGx [m]	COGy [m]	COGz [m]
Wind turbine	1305	-0.3	0	85.5
Semi	2588	0	0	-9.6
Ballast	10188	0	0	-16.5
Total	14080	-0.3	0	-5.7

9.2.2 Moments of inertia

In order to simplify the calculations of the moments of inertia of the FWT, each component of the FWT are separately calculated. Then all contributions are added together to get the global moments of inertia about the principle axes.

In general terms, the moment of inertia is a body's resistance to rotational acceleration and can according to Lien and Løvheiden (2001) be written as:

$$I_i = \int_M r^2 dm \tag{9.6}$$

where r is the perpendicular distance from an arbitrary elemental mass dm to the axis of rotation which coincides with the mass centre of the body.

Another approach is to use the parallel axis theorem. This states that the moment of inertia of a body about any axis can be found by the body's local moment of inertia about an axis which is parallel with an axis which goes through the objects centre of gravity and the perpendicular distance between the two axes.

$$I_i = I_{i,loc} + Ms^2 \tag{9.7}$$

where the global moment of inertia I_i is equal to the local moment of inertia of the body $I_{i,loc}$ plus the Steiner contribution of the mass M multiplied with the perpendicular distance s squared.

Pontoons

In order to simplify the calculations for the moment of inertia, the three pontoons are calculated separately. Each pontoon are assumed to have an evenly distributed mass including the ballast mass, this gives each pontoon the mass $\frac{1}{3}m_{substructure}$. Each pontoon is also considered as a rectangular box with length of 50 metres.

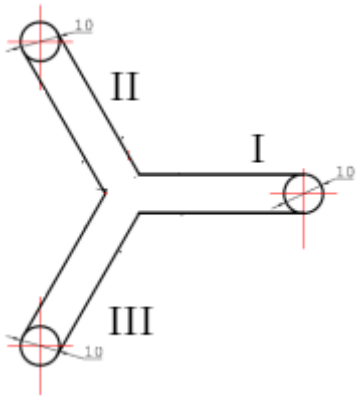

Figure 9.5: Pontoons are divided in three components of equal size

I:
The local moment of inertia for the pontoon with its x-axis parallel to the principle x-axis, the local moment of inertia about the x-axis is calculated as:

$$I_{x,loc} = \frac{1}{12}m(y^2 + z^2) \tag{9.8}$$

The mass, m, is one third of the total mass of the substructure, y and z are the cross section dimension of the pontoon. For the moment of inertia about the x-axis, the cross section is given in the YZ-coordinate system.

Substituting the values in Equation 9.8, the equation is valid for all local moments of inertia for pontoon I.

Adding the Steiner contributions to each local moment of inertia gives the global moment of inertia for pontoon I.

$$I_{x,I} = \frac{1}{12} \cdot m \cdot (y^2 + z^2) + m \cdot s^2 \tag{9.9}$$

Seen in Equation 9.9 the full equation for the moment of inertia about the x-axis for pontoon I is seen. In this equation the perpendicular distance between local and principle axis is equal to the distance between the $COG_{z,FWT}$ and $COG_{z,pontoon}$.

II:
The two pontoons that do not have parallel x-axis with the principle x-axis, a different approach is needed. According to Panagopoulos and Chalkiadakis (2015) the moment of inertia for a tilted cube with the principle axis through its centre of gravity can be written as:

$$I_c = \frac{1}{12} \cdot m \left(l^2 cos^2(\beta) + d^2 sin^2(\beta) + w^2 \right) \tag{9.10}$$

Equation 9.10 is used for both I_x and I_y. Equation 9.10 and Figure 9.6 uses the y-axis in the figure as the axis of rotation.

When calculating the Steiner contributions of these moments of inertia, it is important to remember that it is the perpendicular distance between the local and principal axis which goes into the formula, and not the distance from local axis to origo of the FWT.

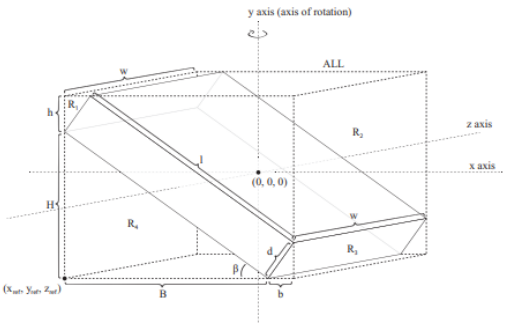

Figure 9.6: Tilted Cuboid with principle axis through COG. Figure taken from Panagopoulos and Chalkiadakis (2015)

To calculate $I_{i,II}$ the equations for local moment of inertia becomes:

$$I_{x,loc} = \frac{1}{12} \cdot m \left(50^2 cos^2(30°) + 10^2 sin^2(30°) + 7^2 \right) \tag{9.11}$$

$$I_{y,loc} = \frac{1}{12} \cdot m \left(50^2 cos^2(60°) + 10^2 sin^2(60°) + 7^2 \right) \tag{9.12}$$

III:
Pontoon III is symmetrical to pontoon II and will therefore have the exact same local moments of inertia and Steiner contributions as pontoon II.

Columns

The columns are considered to be a solid cylinder with constant density.

$$I_{x,loc} = I_{y,loc} = \frac{1}{2}m\left(3r^2 + h^2\right) \tag{9.13}$$

where r is the column radius, and h is the column height.

The local moment of inertia around the z-axis is then calculated as:

$$I_{z,loc} = \frac{1}{2}mr^2 \tag{9.14}$$

Tower

The tower is assumed to have a constant radius equal to the tower base radius, and the tower is also assumed to be a thin rod with constant density. Using these assumptions, the local moments of inertia about the x- and y-axis is:

$$I_{x,loc} = I_{y,loc} = \frac{1}{12}mL^2 \tag{9.15}$$

where m is the mass of the tower and L is the length from top of the pontoon to the nacelle.

As for the columns, the local moment of inertia around the z-axis is based on the assumption that the tower has a constant density:

$$I_{z,loc} = \frac{1}{2}mr^2 \tag{9.16}$$

The Steiner contributions from the tower are a significant contribution to the global moment of inertia.

Nacelle

The nacelle is assumed to be a point mass which is placed on top of the tower. Using Table 9.2, the Steiner contributions from the nacelle can be calculated.

$$steiner_x = steiner_y = m \cdot COG_z^2 \tag{9.17}$$

where m is the mass of the nacelle and COG_z is the distance from the nacelle to origin.

Rotor

Similarly to the nacelle, the rotor is also modelled as a point mass. Hence, only the Steiner contribution is added to the global moment of inertia.

$$steiner_x = steiner_y = m \cdot COG_z^2 \tag{9.18}$$

where m is the mass and COG_z is the vertical distance from the point mass to origin.

Since the rotor does not have it centre of gravity directly vertically above the origin, a Steiner contribution around the z-axis must also be included:

$$steiner_z = m \cdot COG_x^2 \tag{9.19}$$

Global moment of inertia

A summary of the local moments of inertia and the subsequent global moments of inertia are listed below.

Table 9.5: Moments of inertia

Component	Mass [t]	Ix_loc	Steiner x	Global Ix	Iy_loc	Steiner y	Global Iy	Iz_loc	Steiner z	Global Iz
Pontoons	11771	$1.32 \cdot 10^9$	$5.0 \cdot 10^9$	$6.32 \cdot 10^9$	$1.32 \cdot 10^9$	$5.0 \cdot 10^9$	$6.32 \cdot 10^9$	$2.55 \cdot 10^9$	$7.35 \cdot 10^9$	$9.85 \cdot 10^9$
Columns	1005	$7.19 \cdot 10^7$	$1.02 \cdot 10^9$	$1.09 \cdot 10^9$	$7.19 \cdot 10^7$	$1.02 \cdot 10^9$	$1.09 \cdot 10^9$	$1.26 \cdot 10^7$	$2.03 \cdot 10^9$	$2.05 \cdot 10^9$
Tower	628	$9.12 \cdot 10^8$	$2.69 \cdot 10^9$	$3.60 \cdot 10^9$	$9.12 \cdot 10^8$	$2.69 \cdot 10^9$	$3.60 \cdot 10^9$	$2.98 \cdot 10^7$	-	$2.98 \cdot 10^7$
Nacelle	446	-	$6.59 \cdot 10^9$	$6.59 \cdot 10^9$	-	$6.59 \cdot 10^9$	$6.59 \cdot 10^9$	-	-	-
Rotor	230	-	$3.26 \cdot 10^9$	$3.26 \cdot 10^9$	-	$3.26 \cdot 10^9$	$3.26 \cdot 10^9$	-	$1.16 \cdot 10^7$	$1.16 \cdot 10^7$
Sum	14080	$I_x = 2.09 \cdot 10^{10}$			$I_y = 2.09 \cdot 10^{10}$			$I_z = 1.19 \cdot 10^{10}$		

According to Wang (2014), the mass moment of inertia in pitch is $2.15 \cdot 10^{10} kg \cdot m^2$. Seen in Table 9.5 the mass moment of inertia in pitch and roll calculated above are close to the calculations done by Wang (2014). The differences in the calculations are a consequence of different methods and assumptions regarding the geometry of the FWT, and the error is thought to be insignificant for the simulations and are therefore accepted as valid values.

Chapter 10

Modelling in SIMA

This thesis uses the CSC 10 MW model proposed by Wang (2014). Instead of modelling the full CSC 10 MW with the correct plate thicknesses, rotor blades, nacelle and hub, this thesis will simplify modelling by using slender elements in SIMA and the total mass of the FWT is modelled as a point mass in the COG. This simplification is done to save both time when modelling and computational time when running the simulations.

This chapter describes the simplifications made when modelling, and how the environmental loads are modelled. The coordinate system in SIMA is defined as seen in Figure 10.1.

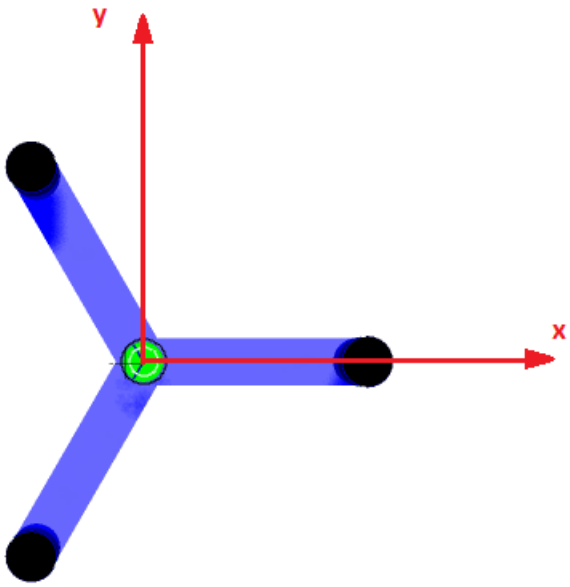

Figure 10.1: Coordinate system in SIMA

The rotor is modelled as a slender element in SIMA. The thrust curve seen in Figure 4.2

show how the thrust force acts for different wind speeds.

10.1 Slender elements

The semi-submersible proposed by Wang (2014) consists of several relatively small pontoons and columns. This is an advantage which can be utilised in SIMA. The columns, pontoons and tower are modelled as slender elements in SIMO. Slender elements have no mass and hence no volume. The slender elements are instead modelled with drag coefficients to simulate the wave and wind drag forces acting on them. The drag coefficients are discussed in detail below. The simplified model of the CSC 10 MW FWT is seen in Figure 10.2.

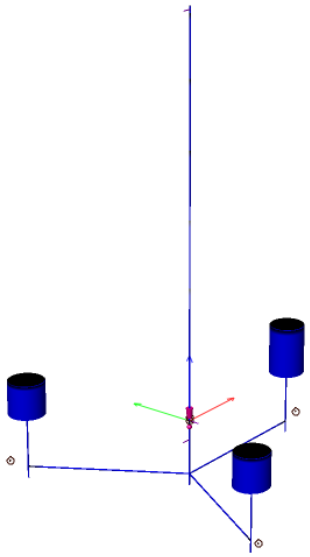

Figure 10.2: CSC 10MW FWT comprised of slender elements

10.1.1 Quadratic hydrodynamic drag coefficients

Slender elements have no physical volume, and hence they have no mass either. But slender elements are modelled to have correct physical attributes by introducing hydrodynamic drag coefficients on the submerged slender elements and wind coefficients on the tower. Moments of inertia of each column, tower and pontoon must be calculated in order to represent the full model accurately.

The hydrodynamic drag coefficients are based on the drag force term from Equation 4.6. Since the slender elements have no mass Equation 4.6 can be rewritten as:

$$dF = \frac{\rho}{2} C_D \cdot D \cdot |u| u \cdot dz \tag{10.1}$$

The pontoons and columns, respectively, have constant cross-sectional areas. Equation

10.1 may therefore be rewritten as:

$$F = \frac{\rho}{2} C_D \cdot D \cdot |u|u \cdot L \tag{10.2}$$

Equation 10.2 contains only constant terms except of the force, F and the fluid velocity u. The equation can then be reordered to contain only constant terms on one side of the equation, but since SIMA sets the quadratic drag coefficients per unit length, the length of the pontoons, columns and tower base is used as input to SIMA and the length is set as a variable to the quadratic drag coefficient. The constant terms are defined as the quadratic drag coefficient per unit length of the slender element.

$$\frac{F}{|u|u \cdot L} = \underbrace{\frac{\rho}{2} C_D \cdot D}_{\text{Quadratic drag coefficient}} \tag{10.3}$$

Equation 10.3 must be calculated for each column and pontoon and used as input in the properties of the slender elements in SIMA.

Table 10.1: Summary of the quadratic drag coefficient for the submerged elements of the substructure

		Y-direction		Z-direction	
	C_D	D_y [m]	C_{QD} $[\frac{Ns^2}{m^3}]$	D_z [m]	$C_{QD}[\frac{Ns^2}{m^3}]$
Column	0.7	10	3587.5	10	3587.5
Pontoon	1.95	7	6995.6	10	9993.8
Tower base	0.7	8.3	2978	8.3	2978

Table 10.1 shows the calculated drag coefficients for the columns, pontoons and tower base used as input to SIMA. The quadratic drag coefficients are divided into a y- and z-direction because of the box geometry of the pontoons, which yields different cross-section diameters in the respective directions.

10.1.2 Quadratic aerodynamic drag coefficients

Since the FWT model is comprised of slender elements, wind forces on the structure are calculated as quadratic wind coefficients and given as input to SIMO. These coefficients are dependent on the wind speed squared.

SIMO assumes the wind field to be 2-dimensional and this report uses the ISO 19901-1 (NPD) wind spectrum. The wind profile used for all wind spectra is described by

$$\overline{U}(z) = \overline{U}_r \left(\frac{z}{z_r} \right)^{\alpha} \tag{10.4}$$

where $\overline{U}(z)$ is average wind velocity at height z above calm water level, and $\overline{U}_r$ is the average wind velocity at the reference height z_r above calm water level. α is a height coefficient ranging between 0.10 - 0.14. Using ISO 19901-1 wind spectra the reference height is 10 meters above calm water level and $\alpha = 0.11$.

SIMO calculates the forces based on the instantaneous wind and body velocities. The force is calculated according to the following formula in SIMO

$$q_j = C_j(\alpha) \cdot v_{rel}^2 \tag{10.5}$$

where j is the degree of freedom, C is the wind force coefficient for the instantaneous relative direction, v_{rel} is the relative wind speed between body and wind and α is the relative velocity direction in the local coordinate system.

The wind direction in SIMO is parallel to the horizontal plane, hence the relative wind speed, v_{rel}, need only be considered for the body motion in x-direction which is then applicable for all directions parallel to the horizontal plane.

The relative wind speed is dependent on the average wind velocity $\overline{U}$, low-frequency wind gusts u and the body velocity $\dot{x}$. Hence, v_{rel} can be written as

$$v_{rel} = \overline{U}(z) + u - \dot{x} \tag{10.6}$$

The relative velocity squared then becomes

$$v_{rel}^2 = \overline{U}(z)^2 + \overline{U}(z)u - \overline{U}(z)\dot{x} + \overline{U}(z)u + u^2 - u\dot{x} - \overline{U}(z)\dot{x} - u\dot{x} + \dot{x}^2 \tag{10.7}$$

Considering that $\overline{U}(z) \gg u$ and $\overline{U}(z) \gg \dot{x}$, the expression for v_{rel}^2 can be written as

$$v_{rel}^2 = \overline{U}(z)^2 + 2\overline{U}(z)u - 2\overline{U}(z)\dot{x} \tag{10.8}$$

The total expression for the wind force seen in Equation 10.5 then becomes

$$q_j = \underbrace{C_j(\alpha) \cdot \overline{U}(z)^2}_{\text{Constant mean force}} + \underbrace{2C_j(\alpha) \cdot \overline{U}(z) \cdot u}_{\text{Dynamic low-frequency force}} - \underbrace{2C_j(\alpha) \cdot \overline{U}(z) \cdot \dot{x}}_{\text{Damping force}} \tag{10.9}$$

Equation 10.9 shows the three major contributions to the wind force calculated by SIMO. A constant mean force, a dynamic low-frequency force proportional to the wind gusts

and a damping contribution proportional to the body velocity. By finding $C_j(\alpha)$ the wind forces can be expressed accurately in the simplified model.

The total body velocity in x-direction, $\dot{x}$, has contributions from the velocity from the two DOF surge and pitch. The total velocity of a point at a distance z from the mean sea water level is written as:

$$\dot{x}(z) = \dot{\eta_1} + z \cdot \dot{\eta_5} \tag{10.10}$$

Inserting Equation 10.10 into the damping term in Equation 10.9, the damping term gets divided into one damping force from the surge motion and one damping force from the pitch motion.

$$2C_j(\alpha) \cdot \overline{U}(z) \cdot \dot{x} = 2C_j(\alpha) \cdot \overline{U}(z) \cdot \dot{\eta_1} + 2C_j(\alpha) \cdot \overline{U}(z) \cdot \dot{\eta_5} \tag{10.11}$$

As seen in Equation 10.4 the average wind velocity at a distance z above sea water level, $\overline{U}(z)$ is dependent on the reference wind velocity. $\overline{U}(z)$ has also a contribution from wind gusts, and Equation 10.4 can be rewritten as:

$$\overline{U}(z) = \left(\overline{U}_r + u\right)\left(\frac{z}{z_r}\right)^{\alpha} \tag{10.12}$$

Inserting Equation 10.10 and Equation 10.12 into Equation 10.9, the total force contributions are described by:

$$q_j = C_j(\alpha) \cdot \overline{U_r}^2 \cdot \left(\left(\frac{z}{z_r}\right)^{\alpha}\right)^2 \tag{10.13}$$

To find the quadratic wind coefficients the aerodynamic forces on the FWT must be identified. The tower will experience a drag force, while the rotor will have a thrust force acting on it when it is operational and a drag force for when the turbine is parked and the blades are feathered. The part of the columns that are above sea water level are neglected due to the small impact these will have compared to the tower and rotor.

An illustration of the aerodynamic forces acting on the FWT is seen in Figure 10.3.

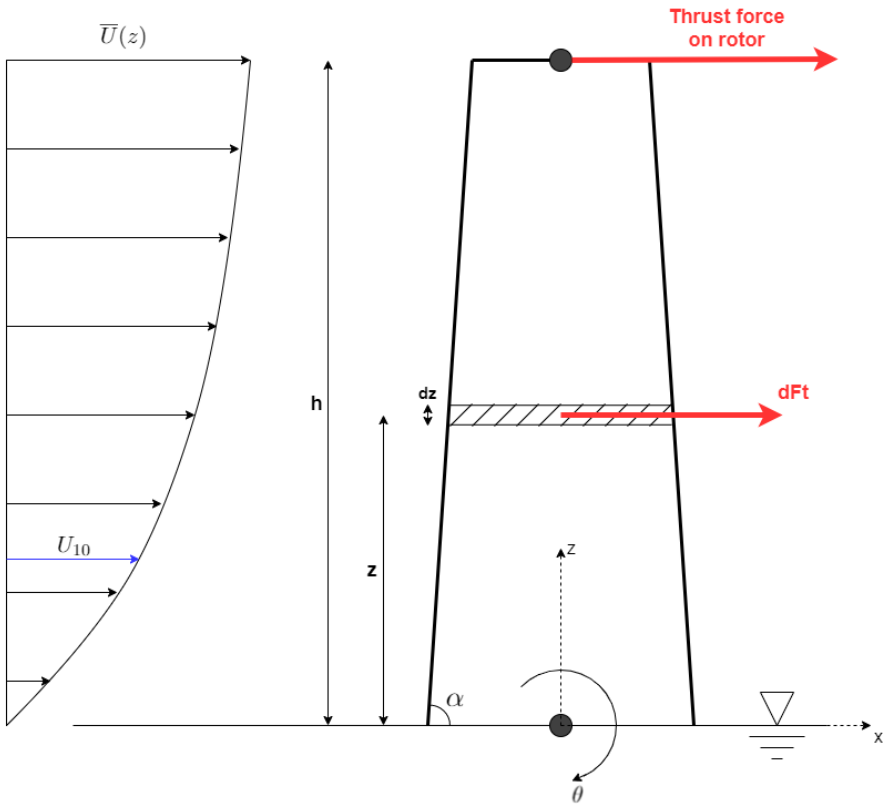

Figure 10.3: Illustration of wind forces acting on FWT tower. Illustration is used to clarify the geometry of the tower, and is not a accurate representation of the actual tower modelled.

Wind forces will affect the FWT in the two DOF surge and pitch. The quadratic wind coefficients inputs from these two DOF are calculated and used as input to SIMA.

Surge

Drag on the tower is calculated using Morisons equation (Equation 4.6). As seen on Figure 10.3, the diameter of the tower is decreasing from tower base to hub. The diameter of the tower can be expressed as a function of z:

$$D(z) = D_{base} - 2 \cdot \frac{z}{tan(\alpha)} \tag{10.14}$$

where $D(z)$ is the diameter at height z, D_{base} is the tower base diameter and α is the inclination angle of the tower, ref. Figure 10.3. The angle α is found by:

$$\alpha = arctan\left(\frac{h}{r_{base} - r_{top}}\right) \tag{10.15}$$

where r_{base} and r_{top} is the tower radius at the base and top respectively, and h is the

vertical distance between sea water level and rotor.

The explicit equation to calculate the quadratic wind coefficients on the tower in surge direction then becomes:

$$dF_{tower} = \frac{1}{2}\rho \cdot C_D \left[D_{base} - 2\frac{z}{tan(\alpha)}\right] \cdot \left[U_{10} \cdot \left(\frac{z}{10}\right)^{\alpha}\right]^2 dz \tag{10.16}$$

As stated above the rotor is modelled as a slender element. The thrust force is included in the model by assuming that the thrust can be modelled as a quadratic wind coefficient as well. Based on the thrust curve seen in Figure 4.2 the first regime up to rated wind speed of 11.4 m/s is assumed to have a quadratic shape. In the second regime the thrust curve is decreasing for higher wind speeds and it does not have a quadratic shape. Hence, a different approach is needed to model the thrust force on the rotor. For the 50 year value the blades are completely feathered and thrust force acting on the rotor can as for regime I be assumed to have a quadratic shape.

Using the relation from Equation 10.9 the constant mean force can be written as the product of the quadratic wind coefficient and the wind velocity squared. The quadratic wind coefficient for the rotor thrust in regime I and III and can then be found by looking at Figure 4.2. These results are shown in Table 10.1.

In regime II the thrust on the rotor cannot be expressed as quadratic wind coefficients. Here, the thrust force is modelled as a constant thrust force applied to the structure at the hub height. This thrust force is graphically found in the thrust curve from Figure 4.2.

Total aerodynamic excitation loads

	Surge, η_1			**Pitch,** η_5		
Wind regime [m/s]	C_{tower,η_1}	C_{rotor,η_1}	C_{total,η_1}	C_{tower,η_5}	C_{rotor,η_5}	C_{total,η_5}
0-11.4	484.5	21554.1	**22038.7**	29788.6	2564940.6	**2594729.2**
11.4-25	484.5	-	**484.5**	29788.6	-	**29788.6**
>25	484.5	81.0	**565.5**	29788.6	9639.0	**39427.6**

10.2 Mooring lines

The mooring lines are modelled as a slender system in SIMA where RIFLEX uses the finite element method to calculate the tensions and displacement of the mooring lines.

Each mooring line segment are added to SIMA by cross-section properties, mass per unit length and the axial stiffness of the mooring line segment. The length of each segment are then used as input to SIMA.

10.3 Decay tests

Decays tests are to be performed so that the natural periods in all DOF can be found. These tests are performed in SIMA. The concept of a decay test is to create an offset of the moored FWT in a DOF, then by looking at how the FWT finds its equilibrium again, important system characteristics of the FWT are found.

The applied forces and moments used in the decay tests are applied for around 200 seconds before they are set to zero. For surge decay the applied force lasts for 250 seconds. The duration of the applied force and moment is dependent on how long time it takes for the FWT to reach the desired offset.

10.3.1 Surge

Decay tests in surge are to be performed by adding a horizontal force to the COG of the FWT. The force direction is in the negative x-direction.

The time series of the applied force is presented in Figure 10.4.

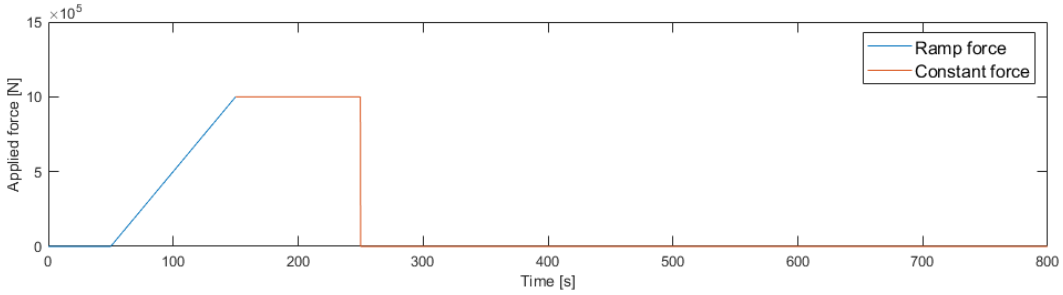

Figure 10.4: Time series of applied force in surge decay

10.3.2 Heave

In the decay test for heave, the applied force is set in the positive z-direction to the COG of the FWT. Time time series of the applied force presented in Figure 10.5

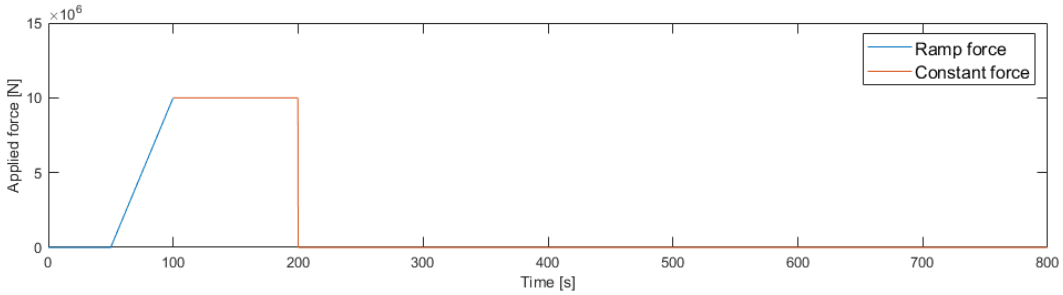

Figure 10.5: Time series of applied force in heave decay

10.3.3 Yaw and pitch

For decay tests in yaw and pitch a moment around respectively the z- and y-axis are applied to the FWT. The magnitude of the moment and the duration of the applied moment is the same for both decay tests. The time series of the applied moment are presented in Figure 10.6.

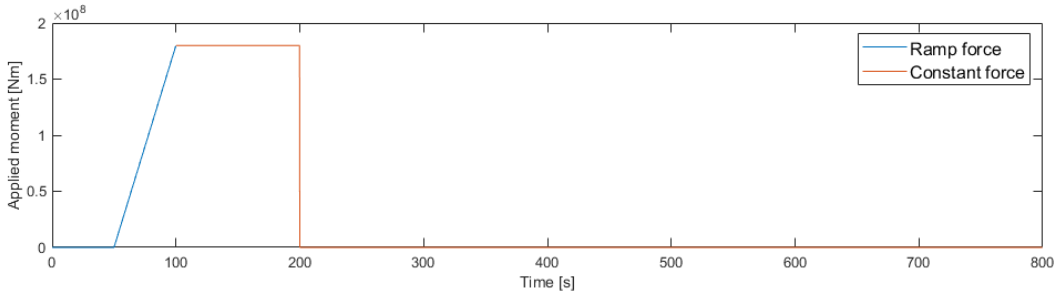

Figure 10.6: Time series of applied moment in pitch and yaw decay

10.4 Pull-out tests

Pull-out tests are performed to identify the total stiffness and restoring force of the system. To perform pull-out tests, a horizontal force is applied to the COG of the FWT in the negative x-direction. By keeping the force constant for a time period, the FWT will reach a surge offset equilibrium.

The force applied to the FWT ranges from 100 kN to 7000 kN. The surge offset is then plotted against the applied force. Two very important system characteristics can then be seen of this plot. One is the restoring force of the system and one the stiffness of the system.

Pull-out tests are performed for all mooring concepts.

Chapter 11

Results

This chapter will present and discuss the results from the time domain simulations and system characteristic analyses done in this thesis. Three main tests are performed, decay tests, pullout tests and time-domain simulations for the three environmental regimes.

11.1 Decay Tests

Decay tests are performed to identify the natural periods and damping of all mooring concept in surge, heave, pitch and yaw. The natural period is the oscillation period that the FWT will have when oscillating freely around origo, and the damping can be seen as the decrease in amplitude of the oscillations.

11.1.1 Surge

The natural period in surge is the most interesting natural period of all DOFs, because surge motions have a large influence on the mooring line tension.

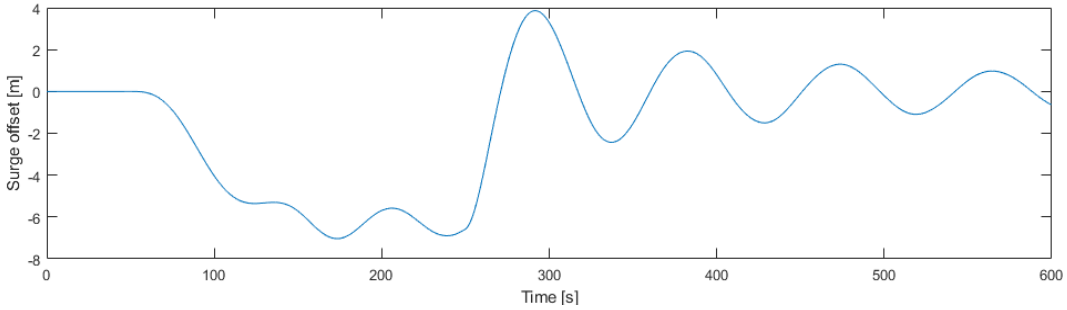

Figure 11.1: Time series of decay test in surge for CPC-BW system

The time series of the decay test in surge for the CPC-BW system is seen in Figure 11.1. The ramp force had a linear effect on the FWT until approximately 110 seconds, before the restoring force in the mooring lines started slowing the ramp force down.

LF oscillations is seen when the constant force is acting. This is due to the force and restoring force of the system dynamically harmonising.

When the constant force is set to zero the restoring forces of the mooring system will act so that the FWT goes back to zero offset. The FWT then oscillates around its equilibrium of zero offset. The natural period in surge for the system is the cyclic period of this oscillation around zero.

All decay tests for the different DOFs have the same shape, but varying oscillation periods.

The natural period in surge is the natural period which significantly changes for all systems. This is expected as the surge motion is highly dependent on the mooring line characteristics. Natural periods in surge for all mooring concepts are presented in Table 11.1.

11.1.2 Heave

Similarly to the time series shown in Figure 11.1 the time series of the the decay test in heave, seen in Figure 11.2, the FWT will oscillate around zero offset when the constant force is set to zero. The frequent oscillations in heave shows that the natural period in heave is significantly lower than the natural period in surge.

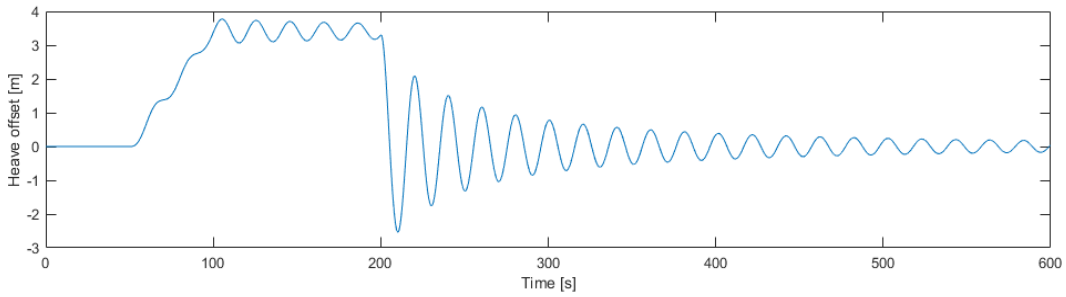

Figure 11.2: Decay test in heave for CPC-BW system

All decay tests in heave showed the same result for the natural period, 20 seconds plus minus 0.2 seconds. This shows that the mooring systems have little or no influence on the heave motion of the FWT. This is because the stiffness in heave is only on the water plane area. This is stated in Equation 4.9 and the water plane area for this FWT is not changing for relatively small heave motions. Hence, the only change in natural periods in heave comes from the slight change in weight of the mooring lines when the structure moves. This is only Natural periods in heave for all mooring concepts are seen in Table 11.1.

11.1.3 Pitch

The time series of the decay test in pitch for the CPC-BW system is shown in Figure 11.3.

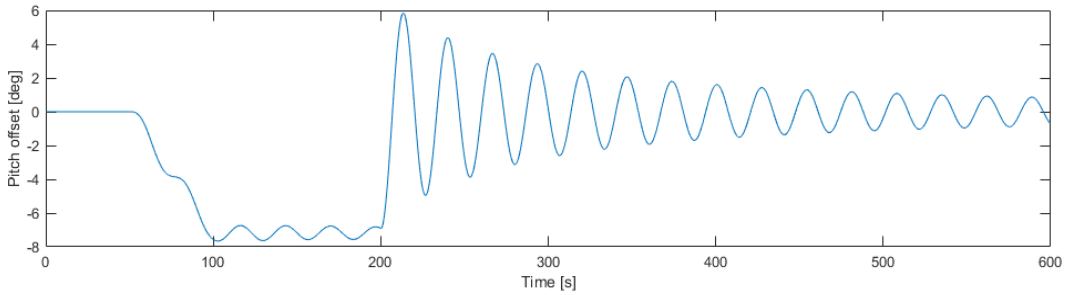

Figure 11.3: Decay test time series in pitch for CPC-BW system

Similarly to heave, the natural period in pitch is approximately constant for all mooring concepts. As seen in Equation 4.10 the stiffness in pitch is dependent on the metacentric height and the displaced volume of the structure. Since these two parameters is approximately constant for the structure, the natural period is also approximately constant. The small differences in natural period of plus minus 0.2 seconds are considered to be due to the changes in weight of the mooring lines when the FWT is pitching. Natural periods in pitch for all mooring concepts are seen in Table 11.1.

11.1.4 Yaw

The time series of the decay test in yaw for the CPC-BW system is seen in Figure 11.4. Seen in Table 11.1 the natural period in yaw is significantly higher for the CWC system compared to the other systems. It is also noted that for the buoy and clump weight systems the natural period is slightly larger than the taut systems. Stiffness in yaw is dependent on the stiffness of the mooring lines and the mooring configuration since the yaw motion will stretch the mooring lines.

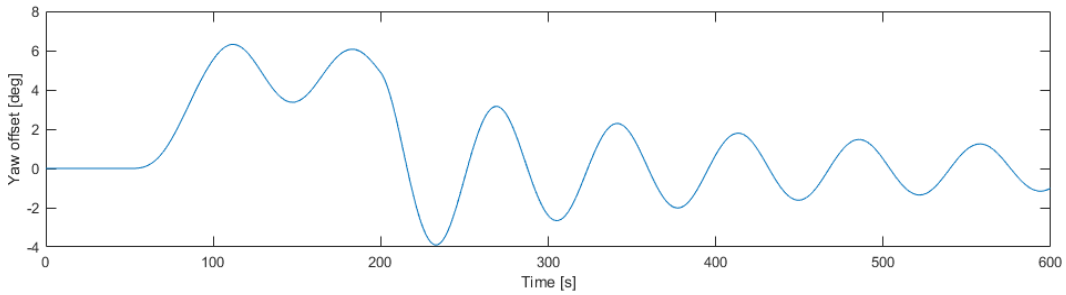

Figure 11.4: Decay test time series in yaw for CPC-BW system

11.1.5 Decay summary

The natural period in surge, heave, pitch and yaw are presented in Table 11.1. Here, it can be seen that the natural periods in surge and yaw change for different mooring

concepts while the natural periods stay constant for heave and pitch.

Table 11.1: Summary of natural periods for all systems and DOFs

	$\frac{EA}{MBL}$	Surge [s]	Heave [s]	Pitch [s]	Yaw [s]
CWC	81.7	164	20	27	93
CPC-T	20	42	20	27	70
CPC-BW	20	85	20	27	73
CPC-BW-NL	Non-linear	115	20	27	71
CNC-5-T	5	85	20	27	69
CNC-10-T	10	65	20	27	70

11.2 Pull-out tests

Pull-out tests are performed to identify the total stiffness and restoring force of the system. Several tests with increasing force was completed, and the surge offset is then plotted against the applied force. The results for all systems are seen in Figure 11.5.

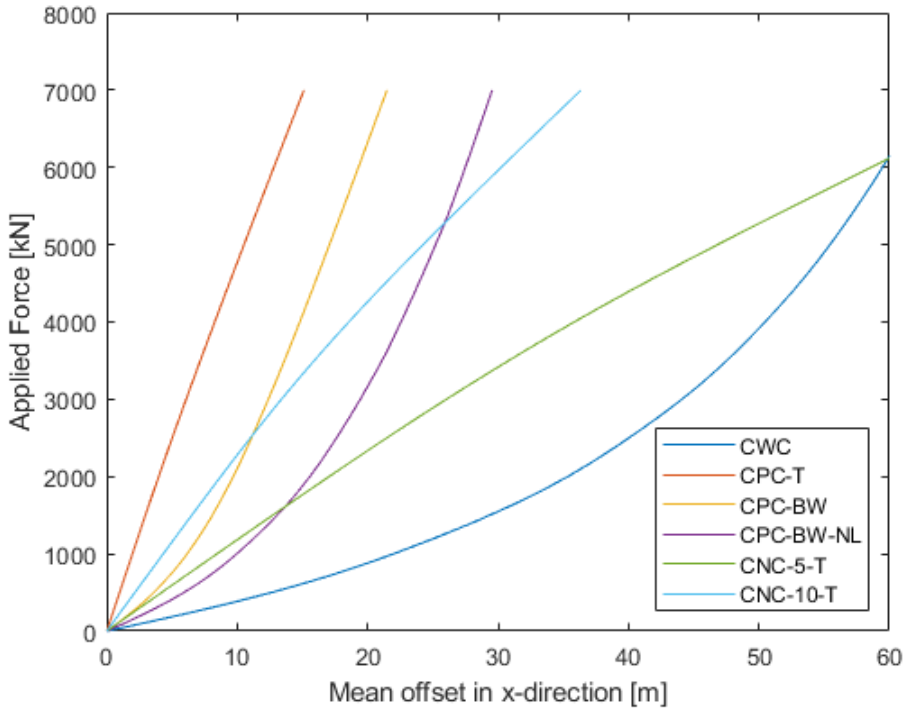

Figure 11.5: Restoring force for all mooring concepts

The forces acting on the body ranges from 100 kN to 7000 kN. The curves in Figure 11.5 give a visualisation of the different mooring concepts stiffness's.

Since the force is acting in negative x-direction the offset is totally dependent on the stiffness of only one mooring line. Notably, the taut mooring systems are seen to have a linear restoring curve from initial position. This is expected as the taut mooring concepts have no geometric stiffness to soften the total stiffness, hence it is totally dependent on

the axial stiffness of the mooring line. The two buoy and clump weight systems are seen to have a lower stiffness than the CPC-T system. Here, it is clear how much the geometric stiffness will soften the system until the surge offset is so large that only the axial stiffness of the mooring lines contribute to the system stiffness. All mooring concepts using polyester mooring lines are seen to have the same constant stiffness when the surge offset is sufficiently large.

The stiffness of a system can be graphically found in Figure 11.5 by dividing the change in tension by the offset. Hence, the steeper a curve is the higher the mooring line stiffness is. Polyester lines in taut mooring is seen to give the highest stiffness of all systems. This is also confirmed by Table 11.1 where the stiffness of a mooring line is seen as a fraction of the minimum breaking load (MBL). In Table 11.1 it can be seen that polyester is modelled with an axial stiffness which is 20 times the MBL of the polyester, and since the polyester lines have a higher MBL than nylon, the taut mooring system with polyester were expected to have higher stiffness.

The restoring curve for the CWC system show how the geometric stiffness will contribute to the total stiffness of the system. Notably, the CWC restoring curve does not become linear, hence the mooring lines does not become totally dependent on the axial stiffness of the chain mooring lines during the pull-out tests.

11.3 Convergence tests of wave and wind seeds

Each time domain simulation has a duration of 3-hours. According to DNVGL-OS-E301 several 3-hour simulations must be performed in order to substitute one long simulation. The time domain simulations for each weather regime keeps the significant wave height, peak period and mean wind speed constant, while the wave and wind seeds are changed for each simulation. These wave and wind seeds represents a randomness in the wave and wind spectres used in SIMA.

To know how many simulations are needed to get the correct results from SIMA, 20 time domain simulations of regime III are performed for all systems. By looking at convergence plots for MPM top tension and the standard deviation of the simulations, the number of realisations needed were found.

A convergence plot of the most probable maximum top tension in the windward mooring line for the CWC and CNC-5-T systems, both in regime III, are seen in Figure 11.6 and Figure 11.7. For the CWC system the MPM is seen to decrease for increasing number of realisations, and no clear convergence is seen. But the range of the y-axis in Figure 11.6 shows that the differences are very small. If only 10 realisations of the CWC system had been used, the error between the tenth iteration and the final convergence value is 1.3%, which is considered to be within an acceptable limit. For the CNC-5-T system it is more clear that the MPM top tension in the windward line will converge after around

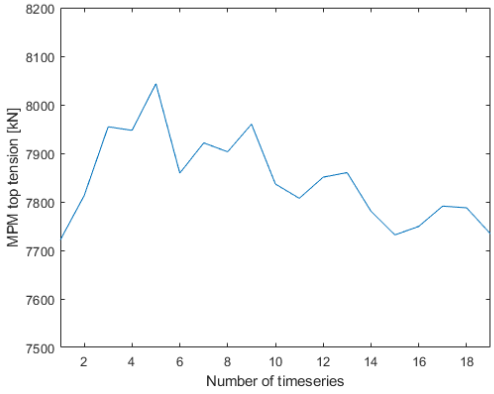

Figure 11.6: Convergence of most probable maximum top tension windward line for the CWC system in regime III

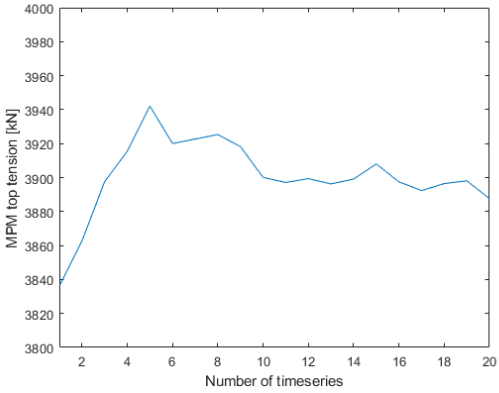

Figure 11.7: Most probable maximum top tension in windward line for the CNC-5-T system regime III

10 realisations.

In Figure 11.8 and Figure 11.9 the convergence plots show the standard deviation of the top tension in the windward mooring line for the CPC-BW and CPC-T systems. Both standard deviations seem to converge at approximately 12 realisations.

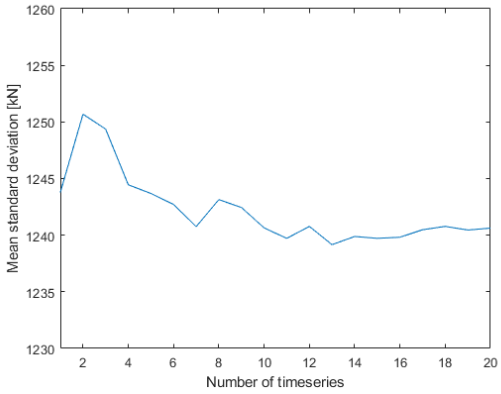

Figure 11.8: Convergence of standard deviation of the CPC-BW system in regime III.

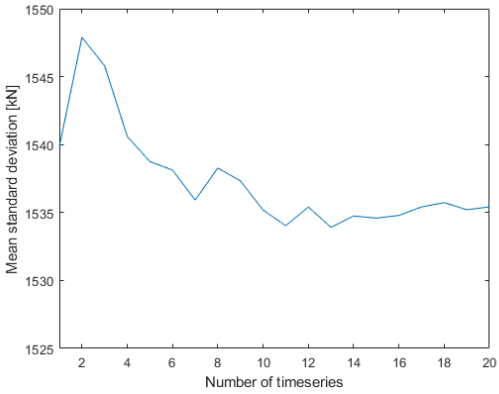

Figure 11.9: Convergence of standard deviation of the CPC-T system in regime III.

In order to be in accordance with DNVGL-OS-E301, DNV-GL (2015), which states that 10-20 realisations are needed to justify substituting one long simulation, this thesis will proceed doing 12 realisations for every mooring concept and every weather condition.

11.4 Time domain simulations

This section presents the results from the time domain simulations for each mooring concept. Table 11.2 shows the key FWT motion results for all mooring concepts and Table 11.3 shows the key results of the mooring line tensions for all mooring concepts.

Seen in Table 11.2 the surge motion is highly effected by the change of mooring concept, while heave and pitch motions are almost constant for all mooring concepts.

As stated in chapter 7 the weather direction for all time domain simulations is in the negative x-direction. Hence, the FWT will get a negative surge offset and the values for surge offset are hence presented as negative values in Table 11.2.

The CWC mooring system yields the highest FWT surge offset of all mooring concepts. In regime I, where the thrust force on the rotor is at its maximum, the LF wind loads seem to affect the mean offset greatly. The greatest most probable maximum value for surge offset for the CWC system is in regime III.

The taut polyester system (CPC-T) shows a considerable lower natural period in surge than for the CWC system. Also the mean offset in surge shows that this system is extremely stiff, which is not preferable to a mooring system. It can be noted that the mean offset in surge for the CPC-T in regime III is only 3.9 metres, while the MPM is 18 metres. This indicate that large dynamic effects on the mooring lines occur for the CPC-T system.

Using buoys and clump weights on the polyester mooring line, the natural period in surge is over doubled. The natural period in surge for the CPC-BW system will make the system less prone to LF loads hitting the resonant periods of the system. The mean surge offset is also seen to almost triple compared to CPC-T system, while the MPM surge offset for regime III only has a slight increase.

The CPC-BW-NL system modelled with the non-linear stiffness model further increases the natural period in surge.

The CNC-5-T system has the same natural period in surge as the CPC-BW system, but the surge offset are very different for the two systems. CNC-10-T system has expectantly a much lower natural period in surge than the lower stiffness system CNC-5-T. The mean and MPM surge offset for the nylon systems are both reasonable results.

Top tensions for the windward and leeward mooring lines are presented in Table 11.3. The column showing the $\frac{EA}{MBL}$ shows the relation between the stiffness of the different mooring lines and the minimum breaking load of the mooring line. The CWC and the CPC-BW-NL systems are the only systems where the stiffness of the mooring lines are not modelled as a determined factor of the MBL.

Top tensions in the windward line shown in Table 11.3 show an interesting occurrence, the mean top tension is largest for the rated wind speed for all systems, while the MPM is the largest for regime III. This is a direct consequence of the mean and MPM surge offsets given in Table 11.2.

Table 11.2: Motion results for all mooring systems with weather direction in-line.

Mooring system	Weather cond.	Natural periods [s]			Surge [m]			Heave [m]			Pitch [deg]		
		Surge	Heave	Pitch	Mean	MP Max	Std. dev.	Mean	MP Max	Std. dev	Mean	MP Max	Std. dev
CWC	11.4 m/s	164	20	27	-41	-46	1.5	-0.2	0.9	0.2	-6.0	11	1.6
	25 m/s				-34	-39	1.2	-0.1	3.0	0.8	-1.8	3.4	0.4
	ULS				-35	-49	3.2	-0.1	7.5	2.0	-0.3	5.9	1.5
CPC-T	11.4 m/s	42	20	27	-4.8	-6.7	0.5	-0.2	0.8	0.2	-7.0	12	1.5
	25 m/s				-3.5	-8.5	1.1	-0.1	3.1	0.8	-2.6	4.1	0.4
	ULS				-3.9	-18	3.3	-0.1	8.1	2.2	-1.2	7.1	1.7
CPC-BW	11.4 m/s	85	20	27	-11	-14	0.6	-0.2	0.9	0.2	-6.9	12	1.5
	25 m/s				-9.2	-14	1.0	-0.1	3.1	0.8	-2.6	4.1	0.4
	ULS				-9.2	-22	3.1	-0.1	8.1	2.2	-1.2	7.2	1.8
CPC-BW-NL	11.4 m/s	115	20	27	-18	-21	0.8	-0.2	0.9	0.2	-7	12	1.6
	25 m/s				-15	-20	1.0	-0.1	3.1	0.8	-2.6	4.1	0.4
	ULS				-15	-28	3.0	-0.1	8.1	2.2	-1.2	6.6	1.5
CNC-5-T	11.4 m/s	85	20	27	-23	-29	1.7	-0.1	0.7	0.2	-7.2	13	1.7
	25 m/s				-16	-22	1.1	0	3.0	0.8	-2.7	4.2	0.4
	ULS				-17	-32	3.2	0	7.8	2.2	-1.3	6.1	1.3
CNC-10-T	11.4 m/s	65	20	27	-12	-16	1.0	-0.1	0.8	0.2	-7.1	13	1.7
	25 m/s				-8.5	-14	1.0	0	3.0	0.8	-2.6	4.2	0.4
	ULS				-9.1	-23	3.0	0	7.9	2.2	-1.3	6.2	1.4

Table 11.3: Natural periods and top tension results for windward and leeward line for weather direction in-line for all mooring concepts.

Mooring system	Weather cond.	$\frac{EA}{MBL}$ [-]	MBL [kN]	Natural periods [s]			Top tension windward [kN]			Top tension leeward [kN]		
				Surge	Heave	Pitch	Mean	MP Max	Std. dev.	Mean	MP Min	Std. dev
CWC	11.4 m/s	81.7	21779	164	20	27	3731	4493	191	1047	983	17
	25 m/s						2984	3920	161	1114	912	37
	ULS						3117	7734	768	1111	517	84
CPC-T	11.4 m/s	20	22563	42	20	27	3611	4684	279	935	651	79
	25 m/s						2937	4989	476	1059	239	258
	ULS						3172	9159	1535	1130	8.7	637
CPC-BW	11.4 m/s	20	22563	85	20	27	3807	4819	256	1186	1046	35
	25 m/s						3061	4785	372	1225	813	114
	ULS						3233	8396	1241	1241	519	265
CPC-BW-NL	11.4 m/s	Non-linear[a]	22563	115	20	27	3632	4528	230	1035	943	23
	25 m/s						2876	4009	222	1068	824	65
	ULS						3012	7065	773	1073	601	149
CNC-5-T	11.4 m/s	5	15000	85	20	27	3343	3816	141	693	508	54
	25 m/s						2757	3153	85	914	680	48
	ULS						2836	3888	254	887	354	125
CNC-10-T	11.4 m/s	10	15000	65	20	27	3367	3989	173	704	509	57
	25 m/s						2751	3473	156	895	491	90
	ULS						2846	4869	485	878	83	231

[a] See Sec. *** for details about the non-linear stiffness

Results for the top tension in the leeward mooring line in Table 11.3 show the mean, most probable minimum top tension and standard deviation of the simulation. The most probable minimum for the CPC-T and CNC-10-T are very small and can indicate that the leeward mooring line goes slack during the simulations. This is not acceptable for synthetic fibre rope mooring lines as the seabed friction against the mooring line can damage the mooring line.

Results from each individual systems are discussed in detail below.

11.4.1 CWC

As the CWC mooring system is the the most conventional mooring concept, the results from this system act as reference values for the other mooring concepts. Therefore, the results for this system are discussed in detail for each weather regime.

Regime I

From Table 11.2, the mean surge offset from all realisations is 41 metres, and the most probable maximum surge offset is 46 metres. The mean surge offset is the largest of the three regimes for the CWC system and as previously mentioned there is a strong correlation between the surge motion and the top tension, hence the mean top tension is also the largest in regime III.

The time series of the surge motion for a single realisation is shown in Figure 11.10. Surge offset is given as negative values as the FWT is drifting along negative x-direction.

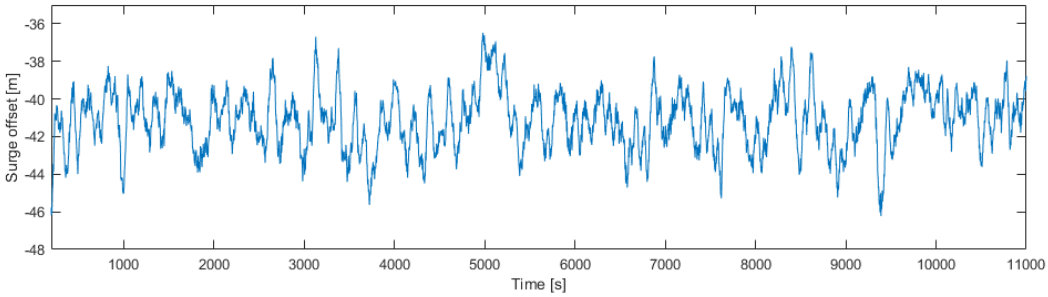

Figure 11.10: Time series of surge offset for the CWC system in regime I. First 200 seconds of time series are removed.

Figure 11.11 shows the time series of the top tension in the windward mooring line for the CWC system in regime I. By comparing the time series in surge and the top tension in the windward mooring line the correlation between them may be seen. Remembering that the surge offset is given as negative values, and since the top tension time series are positive values, the two time series can be seen to mirror each other. Negative peaks in surge gives positive peaks in top tension.

There are not large dynamic responses in surge in this regime, consequently there can

also not be seen any large dynamic tensions in the windward line.

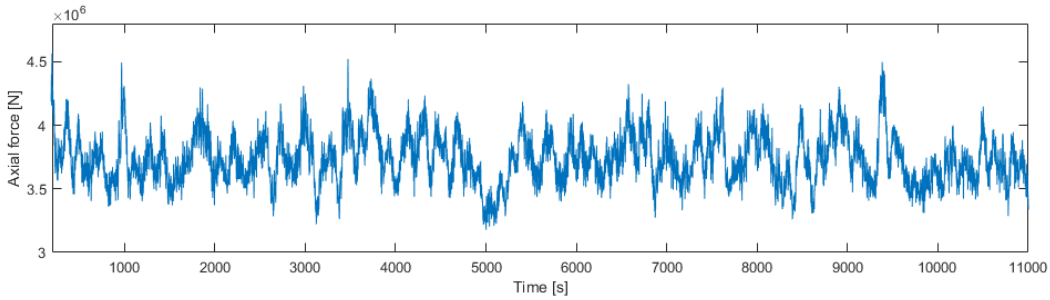

Figure 11.11: Time series of the top tension for the windward mooring line for the CWC system, regime I. First 200 seconds of the time series are removed.

In Figure 11.12 the line force spectrum for the top tension in the windward mooring line where the mean tension is removed, is presented. Notably, the low-frequency spike in Figure 11.12 shows that LF wind loads is totally dominant in this regime. Two other notable peaks is around 0.035 Hz which corresponds to the natural period in pitch, and this spike represents the pitch motion contribution to the line tension and at 0.1 Hz the wave frequency is seen.

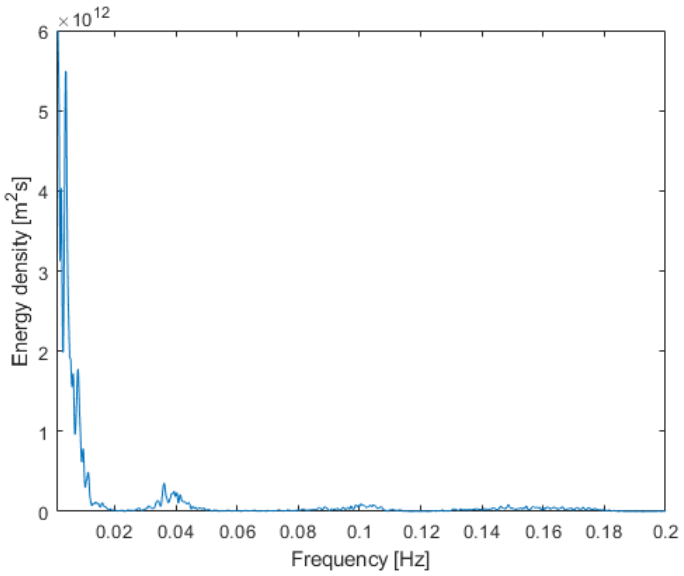

Figure 11.12: Line force spectrum for the top tension in the windward mooring line for the CWC system in regime I. Mean value is removed

The line force spectrum in Figure 11.12 is split up into a LF regime and a WF regime WF energy in Figure 11.13 and Figure 11.14, respectively.

By studying Figures 11.13 and 11.14 the pitch motion is seen to have a much larger effect on the top tension than the WF loads, but these are very small compared to the LF wind gusts.

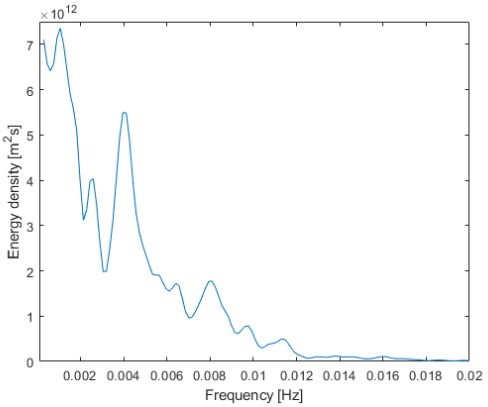

Figure 11.13: Low-frequency part of line force spectrum for top tension in the windward mooring line for the CWC system in regime I. Mean value removed.

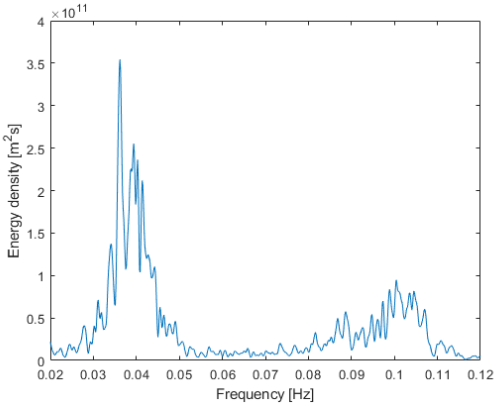

Figure 11.14: Wave-frequency and mean wind frequency part of line force spectrum for top tension in the windward mooring line for the CWC system in regime I. Mean value removed.

The power spectrum of surge motion is presented in Figure 11.15 is very similar to the power spectre for the top tension which is expected since the LF loads will contribute to a large surge offset which consequently leads to high top tensions in the windward mooring line.

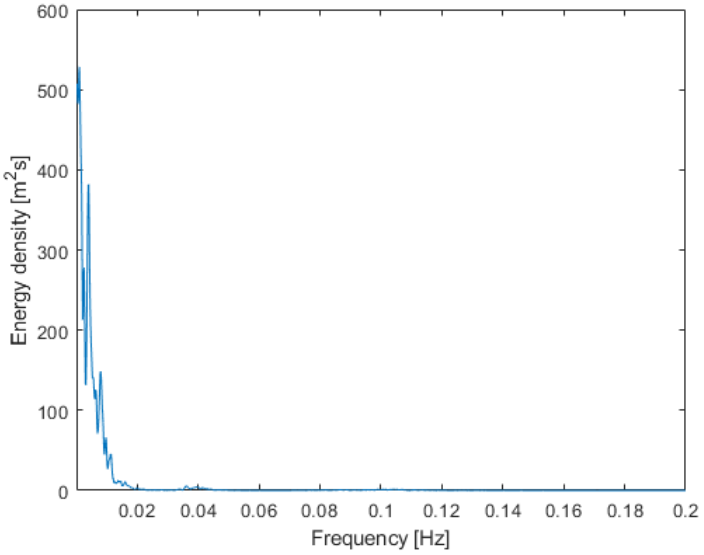

Figure 11.15: Power spectrum for the surge motion for the CWC system in regime I. Mean value is removed

Regime I is when the rotor thrust is at its maximum. This leads to a large pitching moment where the FWT will have large pitch offset in this regime. Table 11.2 shows the high pitching values in this regime. The power spectrum of pitch motion is seen in Figure 11.16.

From the power spectrum the resonant frequency is dominant while LF gusts also con-

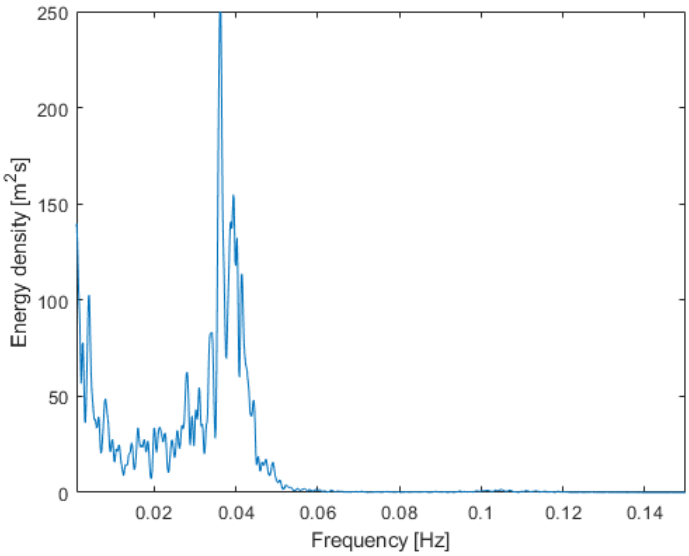

Figure 11.16: Power spectre of pitch motion for the CWC system in regime I. Mean value removed.

tain a lot of energy in the pitch motion. The WF seen around 0.1 Hz has almost no contribution to the pitch motion compared to gusts and LF resonant loads.

In Figure 11.17 the convergence of the MPM top tension in the windward line is presented. The MPM top tension is seen to converge at 4493 kN. The MPM top tension is seen to have a large variation in its convergence plot, but by looking at the y-axis it is noted that variation from one realisation to the converged value is only 50 kN.

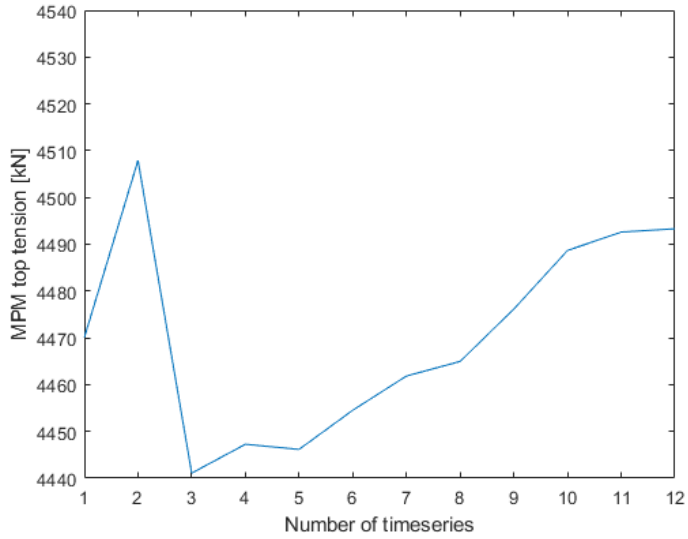

Figure 11.17: Convergence of most probable maximum top tension for the CWC system in the windward line regime I

According to DNVGL-ST-0119 the design tension T_d, described in Equation 6.1 must be

lower than the characteristic capacity shown in Equation 6.3. The design tension for the mooring line in regime I is calculated as:

$$T_d = \gamma_{mean} \cdot T_{mean} + \gamma_{dyn} \cdot (MPM - T_{mean}) = 6184kN \tag{11.1}$$

And the characteristic capacity of the chain and steel rope is:

$$S_C = 20690kN \tag{11.2}$$

Hence, the chain and steel rope are well within DNV-GL's limits.

The standard deviation of the top tension in the windward mooring line is presented in Figure 11.18. It can be seen that the standard deviation does not change much for the different realisations.

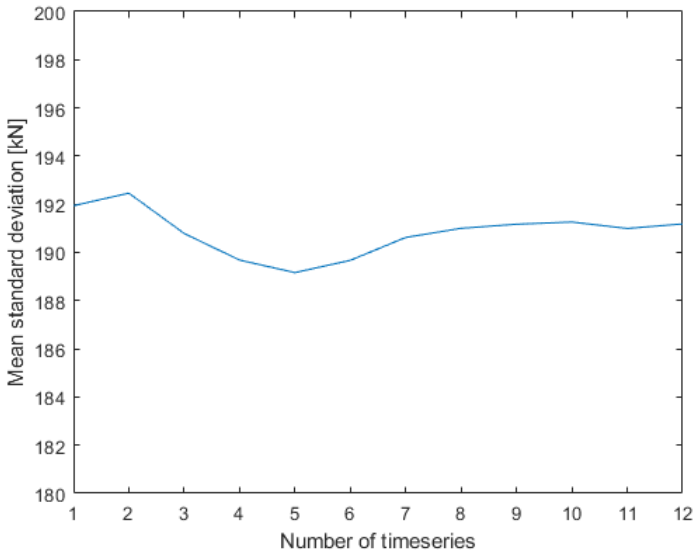

Figure 11.18: Convergence of the standard deviation of the top tension in the windward mooring line for the CWC-system in regime I.

A standard deviation of just 192 kN for a mean top tension of 3731 kN is small, and this small value can be said to verify that the dynamic responses on the FWT is also very small.

Regime II

From Table 11.2 it is seen that both mean offset in surge and most probable maximum offset in surge and pitch is lowest of the three regimes.

Figure 11.19 shows the time series of the surge motion for the CWC system in regime

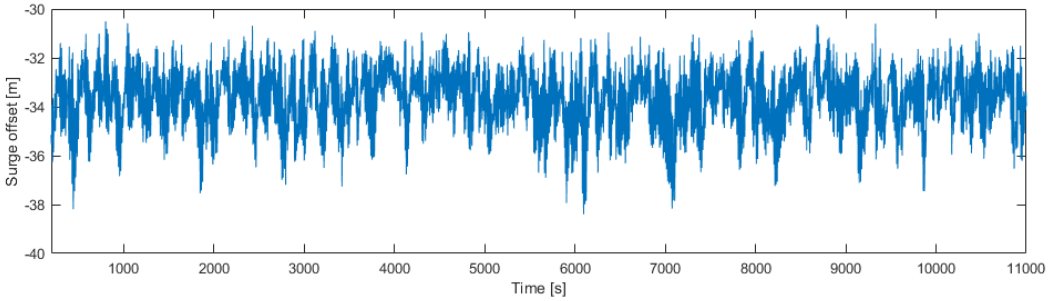

Figure 11.19: Time series of surge offset for the CWC system in regime II

II. Comparing the time series from regime I seen in Figure 11.10 it is interesting to see that there are more high frequency responses in surge in regime II than in regime I.

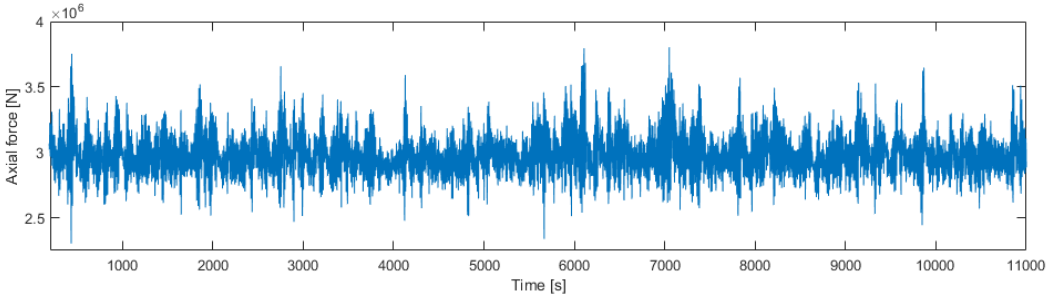

Figure 11.20: Time series of the top tension in the windward mooring line for the CWC system in regime II.

Figure 11.20 shows the time series of the windward mooring line. The time series in surge and the loaded mooring line have similar time series, where dynamic response in surge coincides with the dynamic response in the top tension. It is also noted that the high-frequency responses have a larger impact in regime II compared to regime I.

The line force spectrum for the top tension in the windward mooring line seen in Figure 11.21 verifies the observation from the time series that the high-frequency responses have a much larger effect on the FWT in regime II. The WF in this regime is seen reaching its peak at around 0.08 Hz which is the same as the peak period in this regime.

Notably, the LF wind loads are seen to almost disappear in the line force spectrum. The maximum value is approximately only 10% of the LF energy for regime I. Also the pitch contribution to the top tension at 0.04 Hz is no longer present. This may be a consequence of the modelling of a constant thrust force in this regime, which will give the pitch small dynamic responses.

But it is also expected that the LF wind loads will decrease as the thrust force in this regime is low, and it is only the drag forces from the wind which gives energy in this regime.

The peak seen at 0.15 Hz is the non-linear drag force contribution on the mooring line

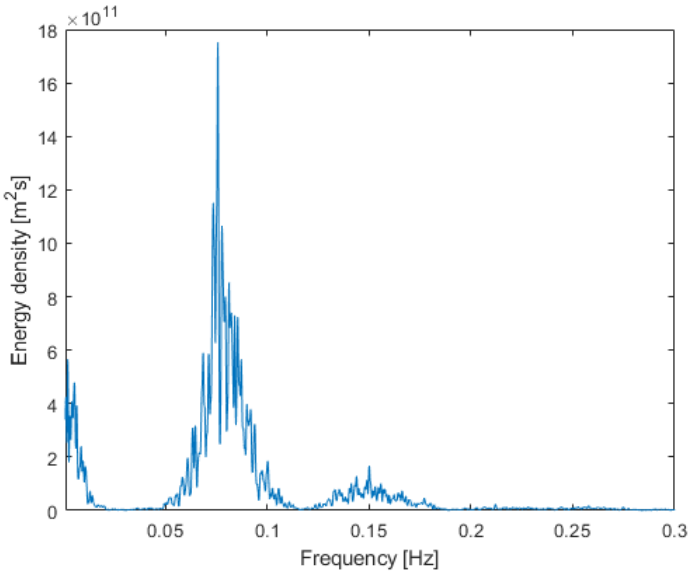

Figure 11.21: Line force spectrum of top tension in the windward mooring for the CWC system in regime II. Mean value removed.

top tension.

Figure 11.22 shows the power spectrum for the surge motion in regime II. It is observed that the LF wind gusts have significantly decreased compared to regime I. This is expected since the blades are feather and the rotor is parked, hence the wind forces will only contribute as drag on the tower and the substructure above seawater level.

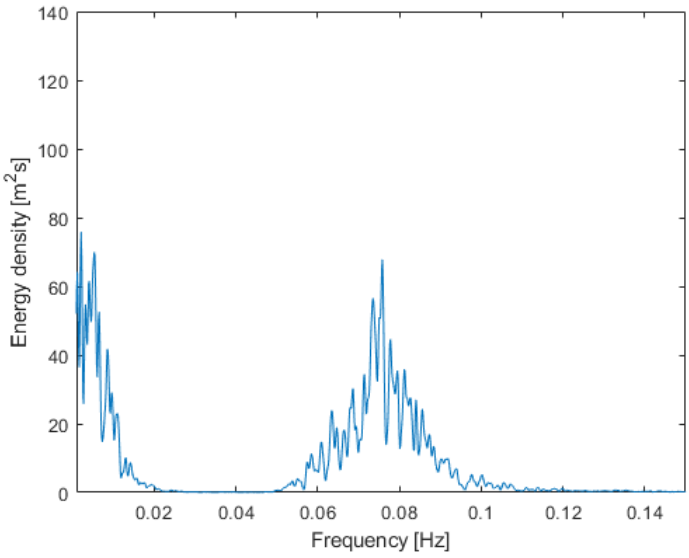

Figure 11.22: Power spectrum of surge motion for the CWC system in regime II. Mean value is removed.

While the LF wind forces have decreased it is also observed that the WF energy at around 0.08 Hz has increased.

One of the most significant differences from regime I to regime II is the pitch motion. Figure 11.23 show how little the LF wind forces affects the pitch motion of the FWT. In regime I the LF wind forces were completely dominant, while in regime II is dominated by the WF.

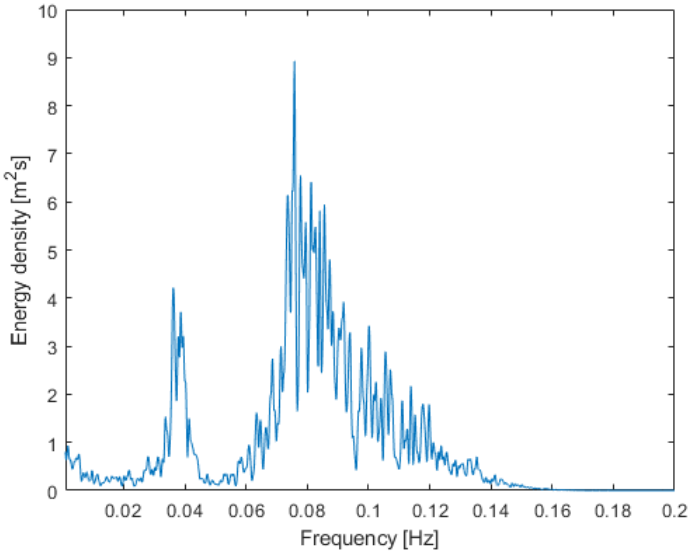

Figure 11.23: Power spectrum of pitch motion for the CWC system in regime II. Mean value is removed.

The design tension in this regime is calculated to be $5517kN$, which is well within the limits set by DNV-GL.

Regime III

For regime III the mean surge offset is lower than for regime I, but the most probable maximum surge offset is higher in regime III. The same goes for the top tension in the windward mooring line.

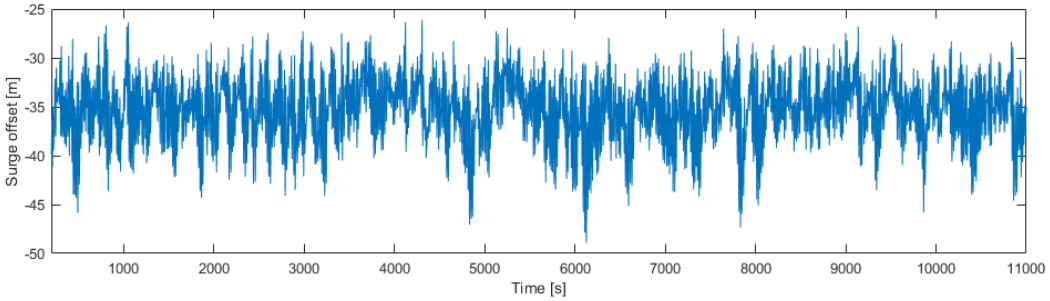

Figure 11.24: Time series of the surge motion for the CWC system in regime III.

The time series for the surge motion for the CWC system in regime III is presented in Figure 11.24. In this regime the high wind velocities cause large drag loads on the tower and blades, combined with the increased wave condition, the FWT will have large dynamic responses.

The time series for the top tension in the windward mooring line is seen in Figure 11.25. This time series clearly shows the large dynamic tensions that will occur during this sea state.

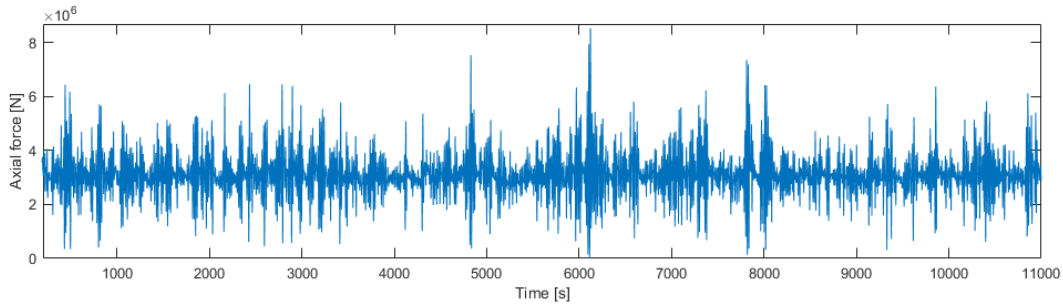

Figure 11.25: Time series of the top tension in the windward mooring line for the CWC system in regime III

Line force spectrum for the windward mooring line top tension and the power spectrum for surge motion of the FWT can be seen in Figure 11.26 and Figure 11.27, respectively.

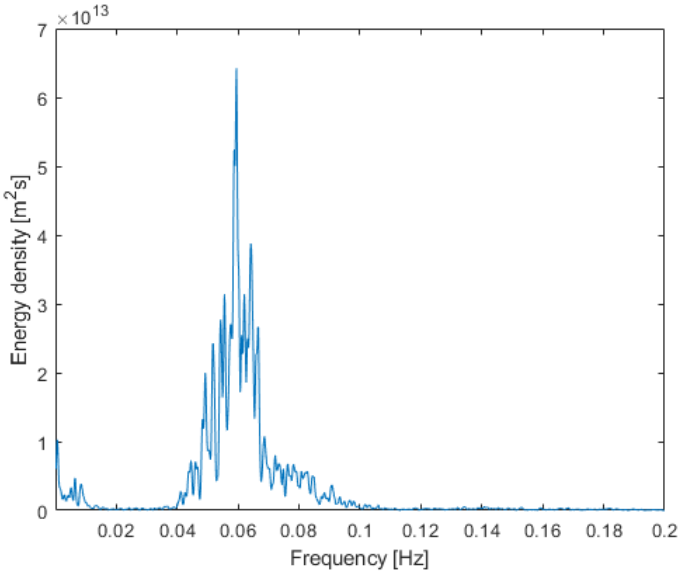

Figure 11.26: Line force spectrum for the top tension in the windward mooring line for the CWC system in regime III. Mean value and transient effects are removed.

The WF can be seen to totally dominate the windward mooring line in the line force spectrum in Figure 11.26. This is as expected, since the LF wind loads will only act as drag forces on the FWT. But it is also noted that the LF wind energy value is approximately the same as for regime I. This is due to the large wind speed which yields large drag forces on the blades and tower.

For the surge motion the power spectrum in Figure 11.27 show that the WF will not dominate as much as it did for the top tension and the LF wind forces will have a larger effect on surge.

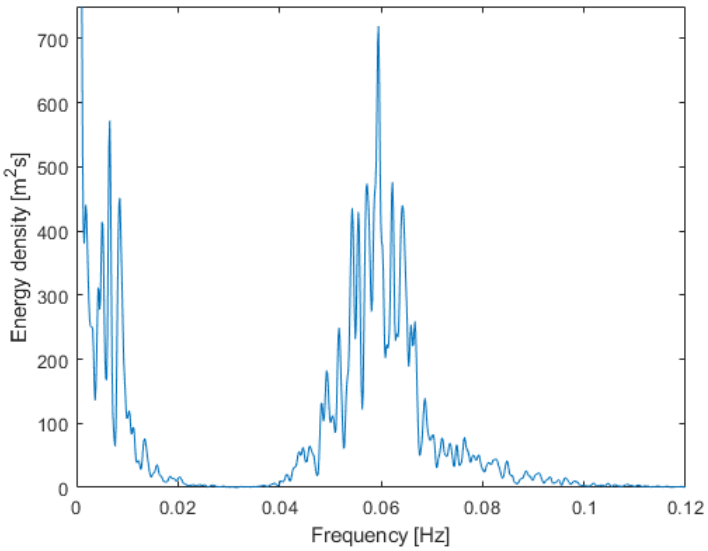

Figure 11.27: Power spectrum of surge motion for the CWC system in regime III. Mean value are removed.

The power spectrum for the heave motion is seen in Figure 11.28. As expected the only contribution to the heave motion is the WF loads.

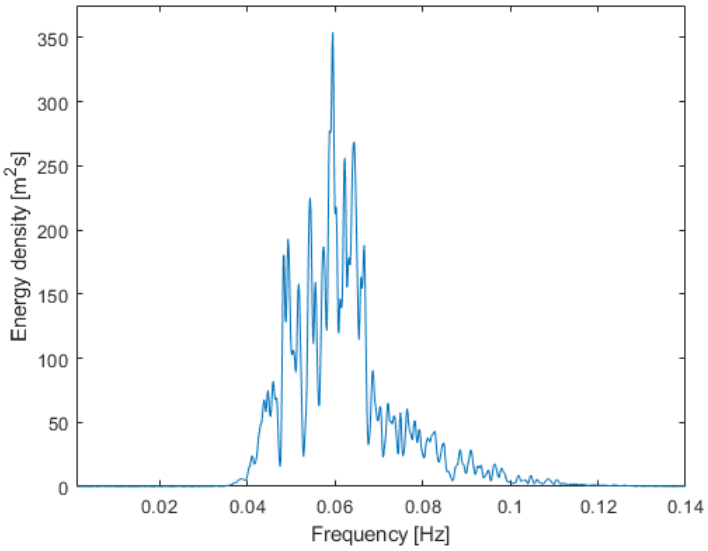

Figure 11.28: Power spectrum of the heave motion for the CWC system in regime III. Mean value are removed.

Figure 11.29 presents the power spectrum of the pitch motion. Notably, pitch have large effects both from the WF loads and the LF wind loads. The drag forces on the FWT from the wind will have a large impact because of the high wind velocity. It is also noted that the pitch motion have energy from a large frequency range compared to the other power spectra shown above.

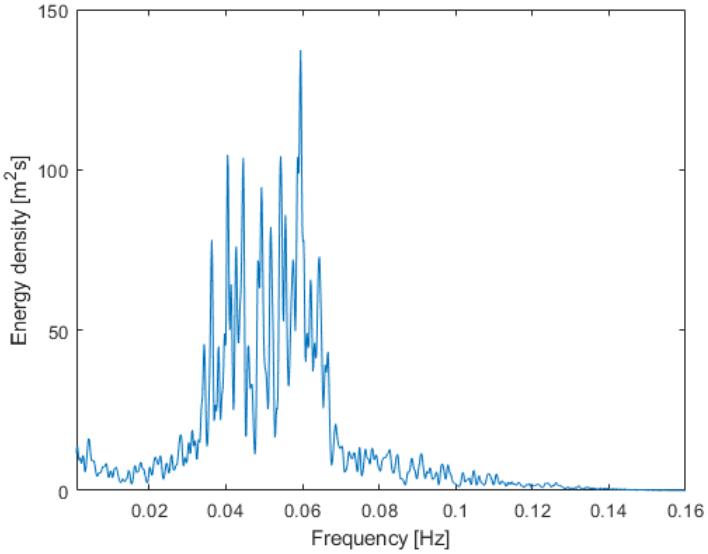

Figure 11.29: Power spectrum of pitch motion for the CWC system in regime III. Mean value are removed.

The CWC system has shown that the 50-year storm in regime III will give the largest tensions in the mooring lines, hence regime III is the ULS for this system.

The most probable maximum top tension is calculated according to Equation 6.5 to be 7734 kN. This gives a design tension of:

$$T_d = 12123kN \tag{11.3}$$

The characteristic capacity of the CWC mooring lines are:

$$S_C = 20690kN \tag{11.4}$$

This means that the CWC mooring lines utilises 59% of the mooring line capacity. It is therefore noted that the mooring lines are too conservative, and the dimensions of the mooring line may be reduced to save cost and still be safe.

Figure 11.30 show the scatter plot of all the maximum values from the realisations made in regime III for the CWC system. This shows the large variation of the maximum values from the realisations made, and how important it is to run several simulations of a weather condition.

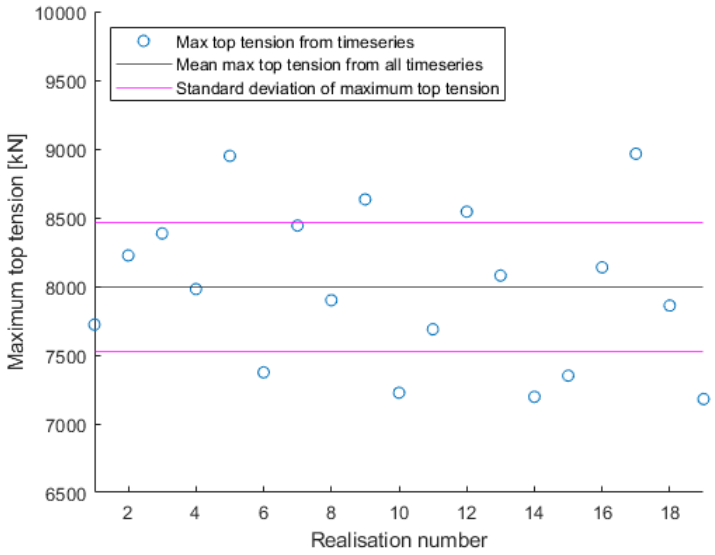

Figure 11.30: Maximum values from all realisations in the CWC system in regime III.

11.4.2 CPC-T

Results from the simulations of the taut mooring system using polyester lines are presented in this section. From Table 11.2 and Table 11.3 it is seen that, as the CWC system, the CPC-T system has larger mean surge offset and mean top tension for regime I, but the largest maximum tension is in regime III. It is also noted that the most probable minimum tension in the leeward line is very close to zero. All of these results must be studied.

The CPC-T system is very stiff compared to the CWC system. The natural period in surge is only 42 seconds, comparing this to the 164 second natural period in surge for the CWC system, it is clear that the CPC-T system can be too stiff to properly function as a safe mooring system. The stiffness of the system is seen graphically in the pull-out test results seen in Figure 11.5.

This high stiffness results in a mean surge offset of only 4.8 metres in regime I and 3.9 metres in regime III.

The two time series of the surge motion of the FWT in regime I and III are seen in Figure 11.31 and Figure 11.32, respectively.

It can clearly be seen that there are much more dynamic responses in surge in regime III compared to regime I and that the WF loads have a large impact in regime III. Even though the mean offset is larger for in regime I, it can be seen in the time series for regime III that the FWT will oscillate more, and go back and fourth the zero offset. The most probable maximum surge offset in regime I is 6.7 metres while in regime III the MPM surge offset is 18 metres, which is almost 5 times as large as the mean offset in

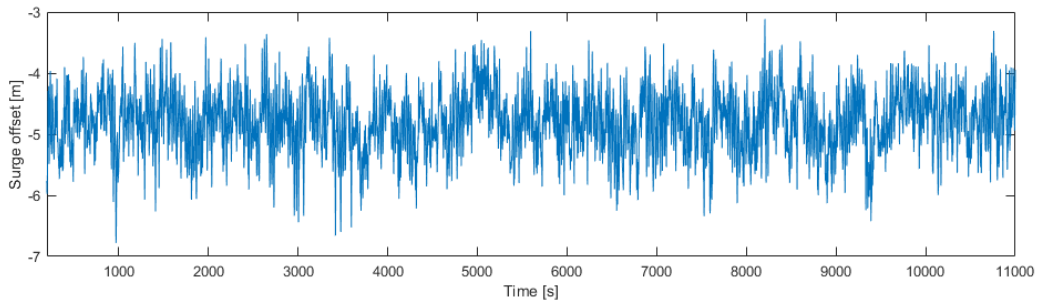

Figure 11.31: Time series of surge motion for the CPC-T system in regime I

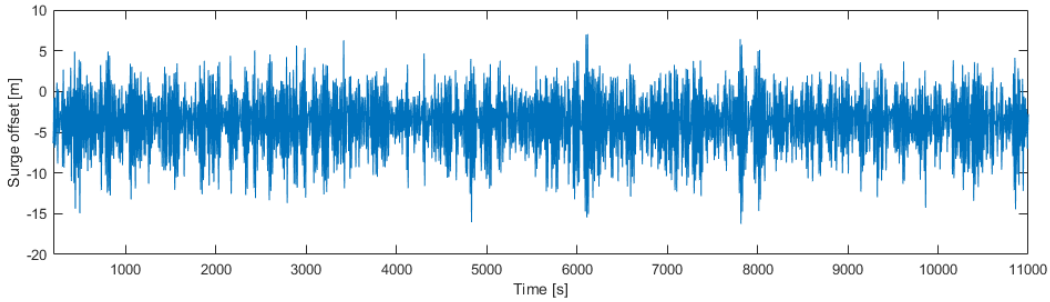

Figure 11.32: Time series of surge motion for the CPC-T system in regime III.

regime III.

Figure 11.33 and Figure 11.34 show the time series of the top tension in regime I and III, respectively. It is clear that the dynamic tensions for regime III is way larger than for regime I. It is also noted that the top tension in regime III seem to go close to zero many times in the realisation.

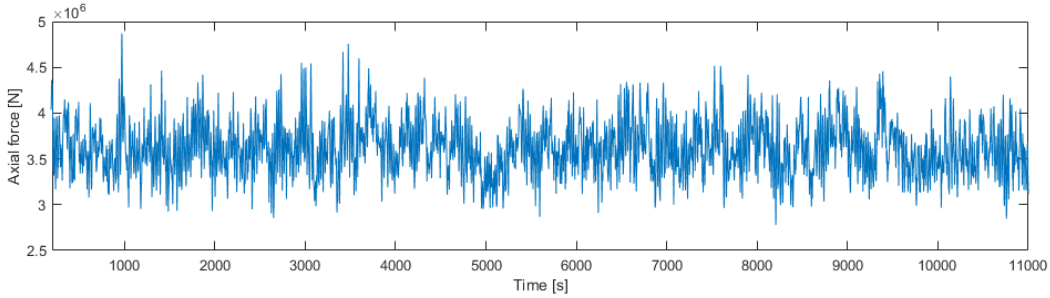

Figure 11.33: Time series of the top tension in the windward line for the CPC-T system in regime I.

Since the top tension in regime III seem to be close to zero, it is a reasonable assumption to think that the mooring line tension at the sea bed will be even lower since the weight of the line will not affect the tension. In Figure 11.35 the time series of the tension in the leeward line down by the anchor is seen.

It is seen that the tension in the leeward line down by the anchor goes to zero multiple times during the time series.

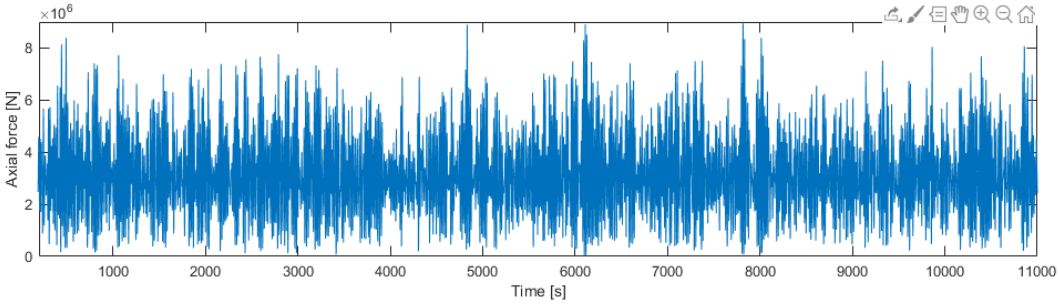

Figure 11.34: Time series of the top tension in the windward line for the CPC-T system in regime III.

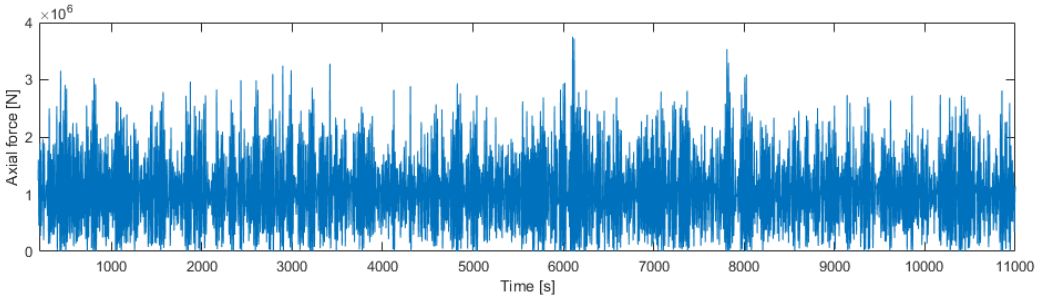

Figure 11.35: Time series of the tension at the anchor connection in the leeward line for the CPC-T system in regime III.

Because of the slack in the polyester lines, the lines will probably sink to the sea bed at several points during the 50-year storm. This will cause friction between the sea bed and the polyester rope which is unacceptable, due to polyester's low resistance to wear and tear. A possible solution to this problem would be to either have a higher pretension in the line or attach a buoy at the connection between the polyester and chain so that the polyester would float even if the mooring line went slack. Higher pretension is considered as bad option for this system as the system already is very stiff, and increasing the pretension would only make the system stiffer. The buoy solution is done in the CPC-BW system.

Figure 11.36 and Figure 11.37 show the power spectrum for the surge motion and line force spectrum for the top tension in the windward line both in regime III, respectively. For the very stiff CPC-T mooring system it is noted how little the LF wind loads influence the surge and top tension on the FWT. Both spectrum's are totally dominated by the WF loads. The natural period in surge means that the LF wind loads and gust will not hit the resonant period of the FWT, hence the contribution from the wind is not as large as for the CWC system.

As seen in Table 11.3 the largest MPM top tension is in the windward line in regime III. This is the highest MPM top tension of all the mooring concepts analysed in this thesis. The resulting design tension calculated according to Equation 6.1 is:

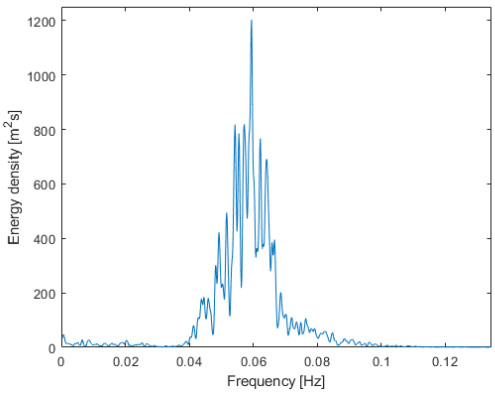

Figure 11.36: Power spectrum of the surge motion for the CPC-T system in regime III. Mean value are removed.

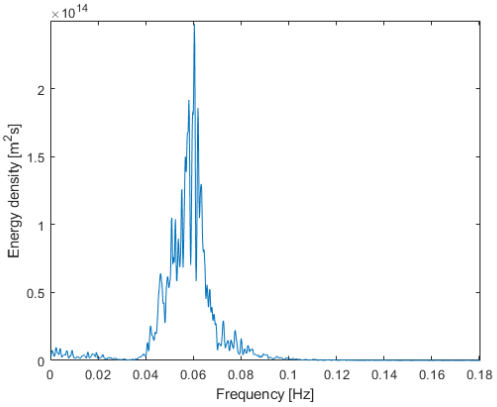

Figure 11.37: Line force spectrum for the top tension in the windward mooring line for the CPC-T system in regime III. Mean value and transient effects are removed.

$$T_d = 14601kN \tag{11.5}$$

Remembering that the CPC-T system consists of chain at the top and bottom of the mooring lines, the characteristic capacity, S_C, must be calculated from the mooring line segment which have the lowest MBL. For the CPC-T system the chain segment has the lowest MBL which is 21779 kN. Hence, the characteristic capacity of the CPC-T system becomes $S_C = 20690kN$. The mooring lines utilises 71% of the capacity. The design tension for this system is well within the limits of DNV-GL.

11.4.3 CPC-BW

The key difference in the results between the CPC-T and CPC-BW system is the natural period in surge. Seen in Table 11.2 the natural period in surge is approximately doubled for the CPC-BW system.

All tension values for the CPC-BW system seen in Table 11.3 seem to be reasonable, and the system looks promising. As for most systems the mean surge offset is largest in regime I, while the MPM in the windward line is highest in regime III.

The time series of the surge motion and the top tension in the windward mooring line is presented in Figure 11.38 and Figure 11.39, respectively.

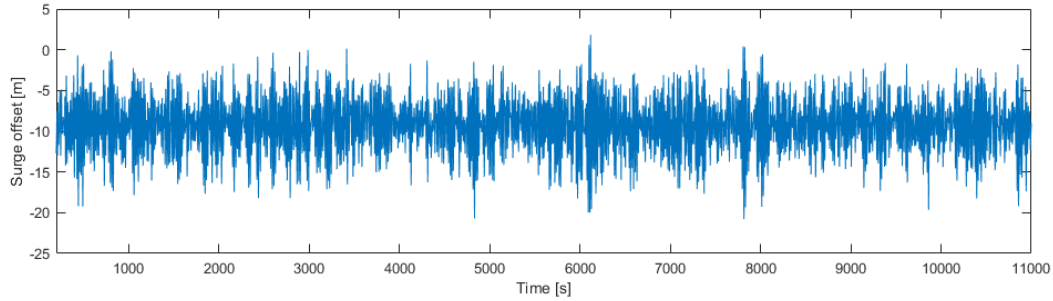

Figure 11.38: Time series of surge motion for the CPC-BW system in regime III.

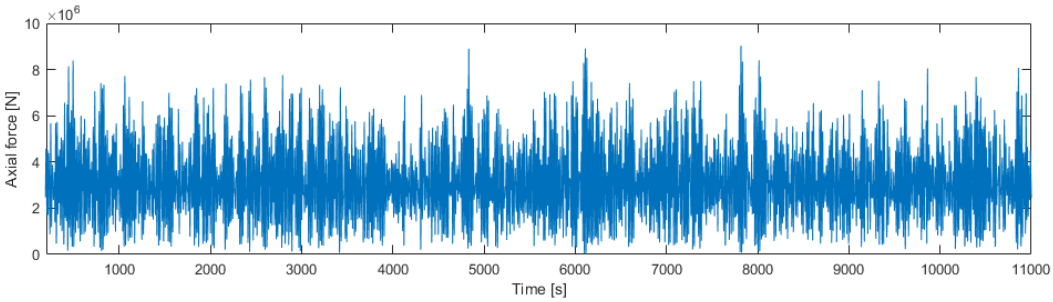

Figure 11.39: Time series of the top tension in the windward mooring line for the CPC-BW system in regime III.

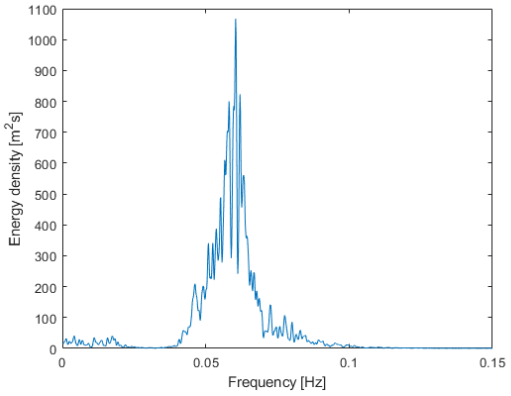

Figure 11.40: Power spectrum of the surge motion for the CPC-BW system in regime III. Mean value are removed.

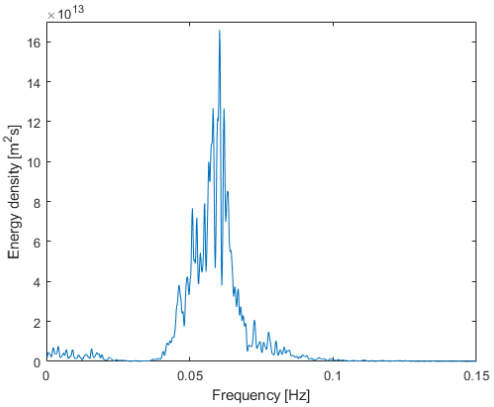

Figure 11.41: Line force spectrum for the top tension in the windward mooring line for the CPC-BW system in regime III. Mean value are removed.

Figure 11.40 show the power spectrum of the surge motion in regime III. The LF wind loads are seen to almost have no impact compared to the dominant WF. The same goes for the line force spectrum seen in Figure 11.41. Almost all of the energy in the windward mooring line comes from the WF loads. This low impact from the LF loads is due to the mooring line characteristic when the line is at its mean surge offset. The geometric stiffness of the line will almost go to zero, and the only stiffness left is the elastic stiffness. Hence, increased stiffness will yield a lower natural period of the system, and the LF loads will not impact the surge motion as much.

The leeward mooring line is seen in Table 11.3 to have a most probable minimum top tension of 519 kN and a standard deviation of 265 kN, which means that the tension will not go slack and that the mooring line will not touch the sea bed. A time series of the leeward mooring line tension at the anchor is seen in Appendix B.

The design tension for the windward mooring line in regime III is calculated to be:

$$T_d = 13238kN \tag{11.6}$$

This means that the mooring lines in the CPC-BW system utilises 64% of the mooring line capacity.

11.4.4 CPC-BW-NL

The natural period in surge is seen in Table 11.2 to increase to 115 seconds for the non-linear stiffness model, compared to 85 seconds for the CPC-BW system. Because the CPC-BW-NL system is softer than the CPC-BW system the mean surge offset is as expected also seen to increase.

Both the mean and MPM top tension in the windward mooring line is seen to decrease for all weather regimes in comparison to the linear stiffness model. And consequently the leeward lines top tension increases.

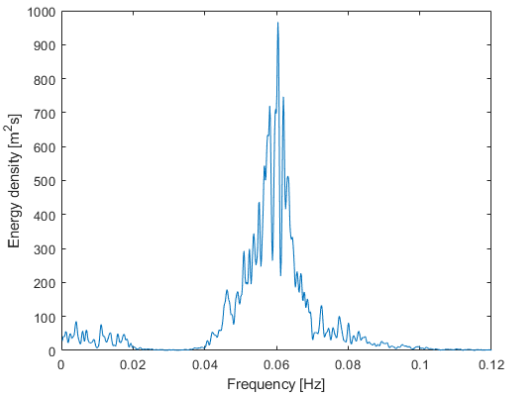

Figure 11.42: Power spectrum of the surge motion for the CPC-BW-NL system in regime III. Mean value are removed.

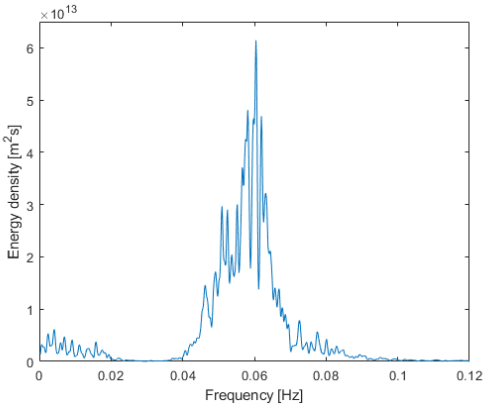

Figure 11.43: Line force spectrum for the top tension in the windward mooring line for the CPC-BW-NL system in regime III. Mean value are removed.

The power spectrum's for surge, heave, pitch and top tension in windward line are very similar to the power spectrum's seen for the CPC-BW system. It is noted in Figure 11.42 and Figure 11.43 that the LF loads have a slightly larger impact on the surge motion and top tension in the windward mooring line.

The CPC-BW-NL mooring system has very similar behaviour as the CPC-BW system.

The biggest difference is the natural period in surge and the LF loads have a little bigger impact on the power spectrum's for the non-linear stiffness model.

The design tension in regime III is calculated to be:

$$T_d = 11008kN \tag{11.7}$$

This gives mooring line utilisation factor of 53%.

11.4.5 CNC-5-T

Table 11.2 show that this low-stiffness nylon mooring line will have large surge motions in all weather regimes. The only mooring concept with a larger mean and MPM surge offset is the CWC system with almost double as large natural period as the CNC-5-T system. By looking at the restoring force curve in Figure 11.5 it is noted that this system is the second to last least stiff system of all the mooring concepts.

This mooring concept is also the only concept where the MPM top tension in regime I is almost as large as the MPM in regime III.

An interesting observation is to compare the CPC-BW system to the CNC-5-T system. Both mooring systems have a natural period in surge of 85 seconds, but it is seen in Table 11.3 that the MPM top tension in the windward mooring line is less than half of that obtained in the CPC-BW system.

Time series in surge motion for both regime I and regime III is seen in Figure 11.44 and Figure 11.45 respectively.

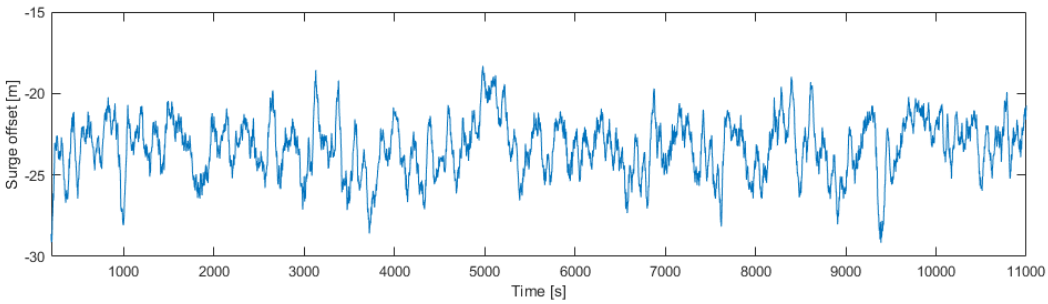

Figure 11.44: Time series of surge motion for the CNC-5-T system in regime I.

It is clear from these time series of the surge motion that the WF will have a much larger impact in regime III than in regime I.

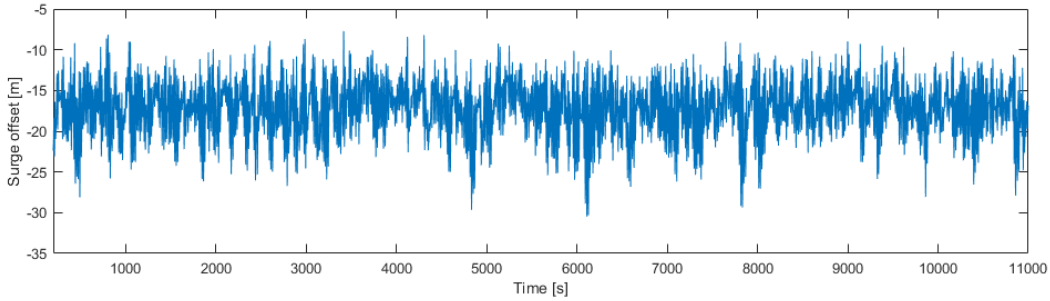

Figure 11.45: Time series of surge motion for the CNC-5-T system in regime III.

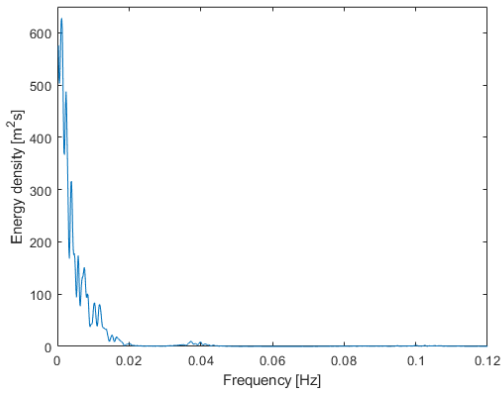

Figure 11.46: Power spectrum of the surge motion for the CNC-5-T system in regime I. Mean value are removed.

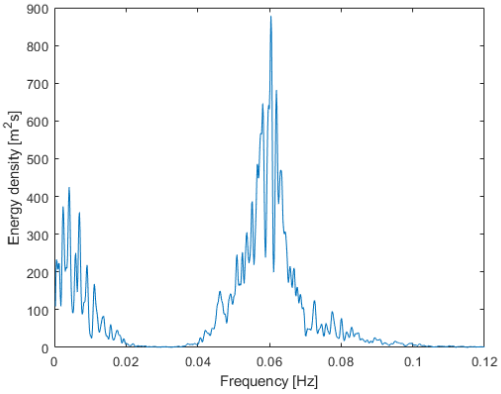

Figure 11.47: Power spectrum of the surge motion for the CNC-5-T system in regime III. Mean value are removed.

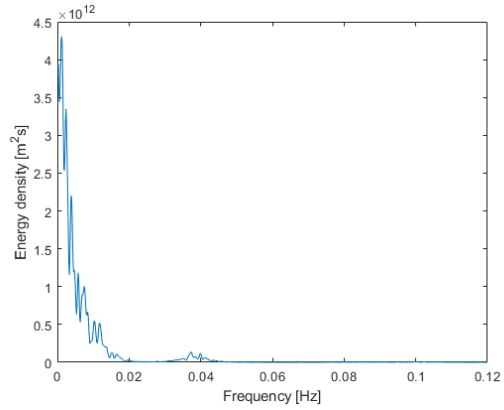

Figure 11.48: Line force spectrum for the top tension in the windward mooring line for the CNC-5-T system in regime I. Mean value are removed.

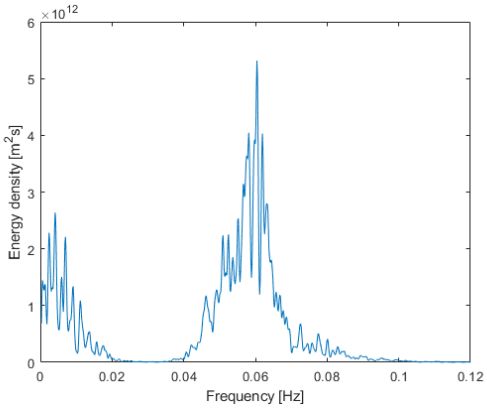

Figure 11.49: Line force spectrum for the top tension in the windward mooring line for the CNC-5-T system in regime III. Mean value are removed.

Power spectrum's for the surge motion in regime I and III is seen in Figure 11.46 and 11.47, respectively. The line force spectrum's in the windward line for the same regimes are presented in Figure 11.48 and Figure 11.49. It is seen that the line force spectrum is a linear transformation of the power spectrum of the surge motion for both regimes. This is due to the taut mooring configuration which makes the system only dependent

on the axial stiffness of the mooring line.

As stated above, the MPM top tension in the windward line has almost the same value for regime I and III. The design tension for both regimes are calculated.

Design tension in regime I:

$$T_d = 5174kN \tag{11.8}$$

Design tension in regime III:

$$T_d = 5528kN \tag{11.9}$$

Both design tensions are well within the requirement of DNV-GL. The MBL of the nylon is 15000 kN, this gives the mooring lines according to Equation 6.3 the characteristic capacity:

$$S_C = 14250kN \tag{11.10}$$

This gives a utilisation factor of just 39% for the CNC-5-T mooring lines. This shows that the mooring lines are designed very conservative, and mooring lines with lower dimensions may be used for this system.

11.4.6 CNC-10-T

The CNC-10-T mooring system is modelled with a higher stiffness than the CNC-5-T system, and as expected the natural period in surge is seen to decrease in the higher stiffness system. Table 11.2 shows that the natural period in surge for the CNC-10-T system is 65 second, which is 20 seconds less than the CNC-5-T system.

Consequently this system is seen to have a higher MPM top tension in the windward mooring line, seen in Table 11.3. The leeward line is seen to have a very small most probable minimum value in regime III. This may be the same problem as with the CPC-T system where the leeward line will go slack in this weather condition, and that is not acceptable for synthetic fibre ropes. In the two other weather regimes the leeward line has a sufficiently large most probable minimum that the mooring line will not go slack.

Figure 11.50 shows the minimum tension in the leeward mooring line down at the anchor for all realisations. Here it is seen that not all realisations will give a minimum value of zero, but all are very close. This means that this system is not applicable since the mooring lines will go slack and scratch against the seabed. This problem may have been solved with a buoy at the nylon rope end, but this mooring concept is not studied in this thesis.

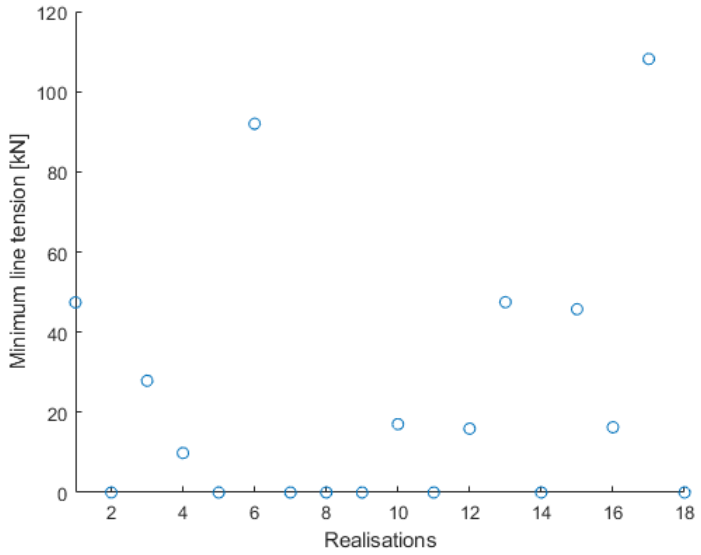

Figure 11.50: Minimum value of leeward mooring line tension at the anchor for all realisations.

The time series of the top tension in the windward mooring line in regime III is seen in Figure 11.51. Similarly to the other top tension time series of the windward line, the WF loads are clearly seen to have a large impact on the dynamic of the mooring line.

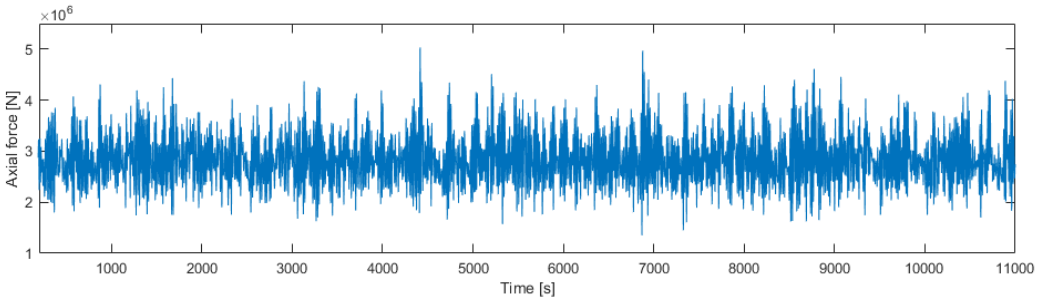

Figure 11.51: Time series of the windward mooring line in the CNC-10-T system in regime III.

Similarly to the CNC-5-T system the CNC-10-T systems power spectrum's of surge and top tension in the windward line are linear transformations of each other due to the stiffness being totally dependent on the axial stiffness of the mooring line. Hence, the surge motion will almost be the only contributing effect on the top tension. The surge motion power spectrum is seen in Figure 11.52 and the top tension in the windward mooring line is seen in Figure 11.53.

It is noted that the LF loads contribute less in regime III for the CNC-10-T system compared to the CNC-5-T system. This is expected as the natural period in surge is smaller for the more stiff system, which will make it less likely that LF loads will create resonant motions on the floater.

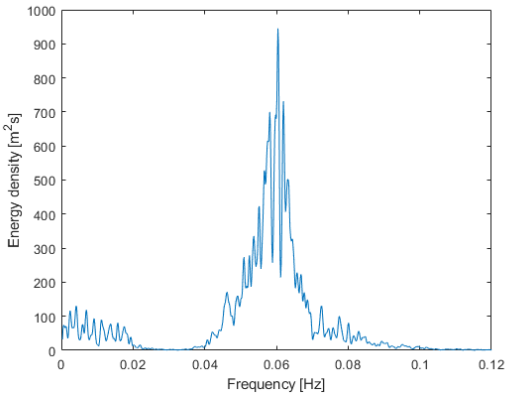

Figure 11.52: Power spectrum of the surge motion for the CNC-10-T system in regime III. Mean value are removed.

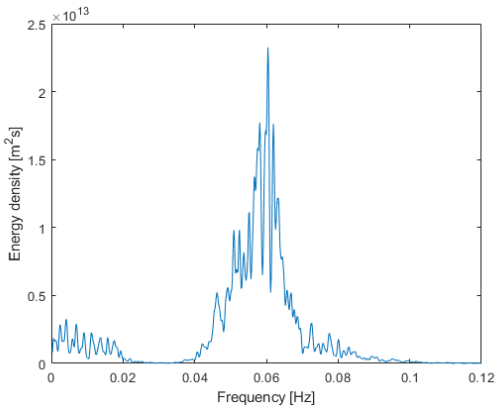

Figure 11.53: Line force spectrum for the top tension in the windward mooring line for the CNC-10-T system in regime III. Mean value and transient effects are removed.

The design tension of the mooring line for the CNC-10-T system is calculated as:

$$T_d = 7239kN \tag{11.11}$$

This gives an utilisation factor of 51% of the mooring line capacity.

11.4.7 In-between ULS simulations

Ultimate limit state simulations were performed with the weather direction in-between two mooring lines for all mooring concept. The key results of the simulations are presented in Table 11.4.

By getting the weather in-between two mooring lines the stiffness of the system will decrease since the stiffness of the system is dependent on the elastic stiffness of the mooring lines which is at an angle to the weather direction. This will cause the FWT to have a large mean surge offset before the stiffness of the systems is the same as for the in-line weather direction. This is seen in Table 11.4, where the both the mean surge offset and most probable maximum surge offset have increased compared to the results seen in Table 11.2.

It is also noted that both mean and most probable maximum top tension in the windward mooring lines will decrease for all systems. However, because of the higher mean surge offset the leeward mooring line tension will also decrease compared to the in-line weather direction. Table 11.4 shows that the most probable minimum top tension in the leeward lines will become very small for the taut mooring systems, as well as the CWC system. For the CWC system this is not a problem as the chain has good properties against seabed friction. But for the synthetic mooring lines this is not acceptable. And it can

be seen in Table 11.4 that this will occur for all taut mooring systems.

As previously stated for the CPC-T system during the in-line weather direction, a solution to avoid the synthetic mooring lines going slack is to attach a buoy at the synthetic mooring line end. This will make the mooring line float if it goes slack. The two systems which have that buoy attached, the CPC-BW and CPC-BW-NL, is seen to have a higher most probable minimum top tension in the leeward mooring line.

Table 11.4: Selected results for all mooring systems with weather direction in-between two lines

Mooring system	Weather cond.	Top Tension Windward [kN]			TopTension Leeward [kN]			Surge [m]			Heave [m]			Pitch [deg]		
		Mean	MP Max	Std. dev	Mean	MP Min	Std. dev	Mean	MP Max	Std. dev	Mean	MP Max	Std. dev	Mean	MP Max	Std. dev
CWC	ULS	2532	4134	273	752	93	98	53	65	3.5	-0.2	7.3	2.0	0.27	4.9	1.3
CPC-T	ULS	2518	5376	701	679	0	630	4.8	17	3.1	-0.1	7.9	2.1	1.4	6.9	1.5
CPC-BW	ULS	2688	4988	580	914	292	252	15	26	3.0	-0.2	7.5	2.0	1.3	6.3	1.4
CPC-BW-NL	ULS	2500	3996	341	789	362	132	25	35	3.0	-0.2	7.7	2.1	1.4	6.2	1.3
CNC-5-T	ULS	2158	2631	120	373	57	156	17	28	3.1	0	8.0	2.2	1.4	6.3	1.3
CNC-10-T	ULS	2247	3425	278	330	28	213	10	23	3.2	0	8.7	2.3	1.4	5.9	1.2

Chapter 12

Conclusion

This thesis has analysed six different mooring concepts for a FWT at the same location where Hywind Tampen is to be located. One mooring system uses conventional chains and steel rope as mooring lines. Three systems uses polyester rope, and two systems use nylon as their mooring lines.

All conclusion stated below are based on ULS simulations with intact mooring lines for the system.

Excluding the taut mooring system using polyester mooring lines, all systems show promise to be used as mooring systems for the FWT. The CPC-T mooring system with a natural period in surge of only 42 seconds, and a mean surge offset of 3.9 metres in the in-line weather direction, is very prone to large dynamic effects due to its high stiffness, and this system had the highest most probable maximum top tension in the windward mooring line off all systems. The leeward line also went slack for both weather directions which is not acceptable for synthetic fibre ropes.

The two taut mooring concepts using nylon showed that nylon gave the system a lower stiffness than the taut polyester system. Both nylon systems also had low MPM top tensions in the windward mooring line compared to the polyester. But the CNC-10-T mooring concept showed that the leeward tension would go to zero for many of the realisations. Using a buoy and clump weight on the nylon systems could improved the system so that the leeward line did not go slack.

Using a buoy and clump weight on the synthetic mooring lines seem to have a very positive effect on the mooring system design. Both systems using buoy and clump weight had high natural periods in surge, design tensions well within the limits set by DNV-Gl, and the leeward lines did not go to slack even for the in-between weather direction.

The results in this thesis show that the use of synthetic fibre ropes is a good option

to using chains when mooring a FWT. By increasing the industry knowledge of the synthetic fibre rope properties, optimised mooring configurations can be developed and used in the next FWT project.

12.1 Recommendations for further work

- Increase knowledge of nylon properties and how to model these mooring lines properly.
- Use mooring lines with lower MBL to optimise the mooring system in terms on cost savings.
- Analyse nylon mooring systems using buoy and clump weights to remove the possibility of slack in leeward mooring line.
- Integrated dynamic analyses of the full CSC 10 MW model with blades and pitch controller should be performed in order to verify if the simplified model has taken into account the correct loads and responses.
- Optimisation of anchor placement and pretension should be performed to get the maximum utilisation results of each system.
- ALS and FLS simulations should be performed to assess the fatigue capacity of the mooring lines.

Bibliography

Bak, C., Zahle, F., Bitsche, R., Kim, T., Yde, A., Henriksen, L.C., Hansen, M.H., Blasques, J.P.A.A., Gaunaa, Mac & Natarajan, A., 2013. The DTU 10-MW reference wind turbine, in: *Danish Wind Power Research 2013*, Sound/Visual production (digital). pp. 1–22.

Beiter, P., Musial, W., Smith, A., Kilcher, L., Damiani, R., Maness, M., Sirnivas, S., Stehly, T., Gevorgian, V., Mooney, M., Scott, G., 2016. *A Spatial-Economic Cost-Reduction Pahway Analysis for U.S Offshore Wind Energy Development from 2015-2030.* `https://www.nrel.gov/docs/fy16osti/66579.pdf`(Accessed: 22. May 2020).

Bridon, 2013. *Oil and Gas. Wire and fibre rope solutions for the world's most demanding applications.*

Bridon, 2020. *Bridon Structural Systems.*

BVG, A., 2019. *Guide to an Offshore Wind Farm.* Published on behalf of the Crown Estate and the Offshore Renewable Energy Catapult.

Chakrabarti, S.K., 2005. *Handbook of Offshore Engineering.* Oxford: Elsevier Science & Technology.

DNV-GL, 2015. *DNV-GL-OS-E301: Position mooring.* Available at: `https://rules.dnvgl.com/docs/pdf/dnvgl/os/2015-07/DNVGL-OS-E301.pdf` (Accessed: 12. May 2020).

Equinor, 2014. *Hywind Scotland Mooring System.* Available at: https://ntnu.blackboard.com. (Accessed: 03. June 2020).

Equinor, 2016. *Snorre Field Metocean Design Basis.*

Equinor, 2017. *Hywind Scotland Pilot Park Project Plan for Construction Activities 2017.* `http://marine.gov.scot/sites/default/files/00516548.pdf`(Accessed: 22. May 2020).

Equinor, 2019a. Investing in hywind tampen development. URL: `https://www.equinor.com/en/news/2019-10-11-hywind-tampen.html`. (Accessed: 29. January 2020).

Equinor, 2019b. *Hywind-up close and personal.* https://www.equinor.com/en/what-we-do/hywind-where-the-wind-takes-us/hywind-up-close-and-personal.html. [Accessed=16.12.2019].

Equinor, 2020a. *How Hywind was born.* Available at: https://www.equinor.com/en/magazine/how-hywind-was-born.html.html(Accessed: 22. May 2020).

Equinor, 2020b. *Hywind Demo.* Available at: https://www.equinor.com/en/what-we-do/floating-wind/hywind-demo.html(Accessed: 22. May 2020).

Faltinsen, O.M., 1990. *Sea Loads on Ships and Offshore Structures*. Cambridge: Cambridge University Press.

GcCaptain, 2012. *Maersk wins anchor handling contracts.* https://gcaptain.com/maersk-wins-anchor-handling-contracts/(Accessed: 25. May 2020).

Greco, M., 2019. TMR 4215: Sea Loads. Lecture Notes. *TMR 4215 Sea Loads.* Available at: https://ntnu.blackboard.com. (Accessed: 20. January 2020).

Huntley, M., 2016. *Fatigue and modulus characteristics of wire-lay nylon rope*, pp. 1–6. doi:10.1109/OCEANS.2016.7761501.

IEA, 2019. *Offshore Wind Outlook 2019.* Available at: https://www.iea.org/reports/offshore-wind-outlook-2019.

IFE, 2020. *Baseline Mooring System Characteristics 150m water depth.* Provided by Kjell Larsen.

Larsen, K., 2018. Memo. axial stiffness of polyester ropes - proposed stiffness model.

Larsen, K., 2019. Lecture Notes 8 - Station Keeping and Mooring of Floating Structures. *TMR4225 Marine Operations.* Available at: https://ntnu.blackboard.com. (Accessed: 14. January 2020).

Larsen, K., 2020a. Marine Operations of installing a floating wind turbine farm (Equinor's Hywind Tampen). *TMR4225 Marine Operations.* Available at: https://ntnu.blackboard.com. (Accessed: 29. January 2020).

Larsen, K., 2020b. Marine Operations of Installing a Floating Wind Turbine Farm. *TMR4225 Marine Operations.* Available at: https://ntnu.blackboard.com. (Accessed: 03. June 2020).

Lien, J., Løvheiden, G., 2001. *Generell fysikk for universiteter og høgskoler*. Universitetsforlaget.

Luan, C., Moan, T., Gao, Z., 2018. *Design and analysis for a steel braceless semi-submersible hull for supporting a 5-MW horizontal axis wind turbine.* Phd thesis. Norwegian University of Science and Technology.

Nysæther, J.B., 2019. Experiences from Hywind Scotland and the Way Forward for Floating Offshore Wind, in: EERA DeepWind, pp. 1–14. URL: https://www.sintef.no/globalassets/project/eera-deepwind-2019/presentations/opening_nysather_equinor.pdf.

Panagopoulos, A.A., Chalkiadakis, G., 2015. *Moment of Inertia of Potentially Tilted Cuboids*. KSE kasmd .

Power, P., 2020. *Windfloat®*. http://www.principlepowerinc.com/en/windfloat(Accessed: 23. May 2020).

Ramnæs, 2015. *Top Quality Offshore Products for Harsh Offshore Conditions.*

ResearchGate, 2017. https://www.researchgate.net/figure/Typical-suction-anchors-used-as-foundation-of-a-floating-offshore-platform-courtesy_fig3_320244827(Accessed: 25. May 2020).

SINTEF-Ocean, 2019. SIMO 4.16.1 Theory Manual.

Vryhof, 2020. Anchors: Stevpris mk6. http://www.vryhof.com/products/anchors/stevpris_mk6.html(Accessed: 25. May 2020).

Wang, Q., 2014. *Design and Dynamic Analysis of a Steel Poonton-type Semi-Submersible Floater Supporting the DTU 10MW Reference Turbine*. M.s. thesis. Norwegian University of Science and Technology.

Appendix A

Metocean Design Basis

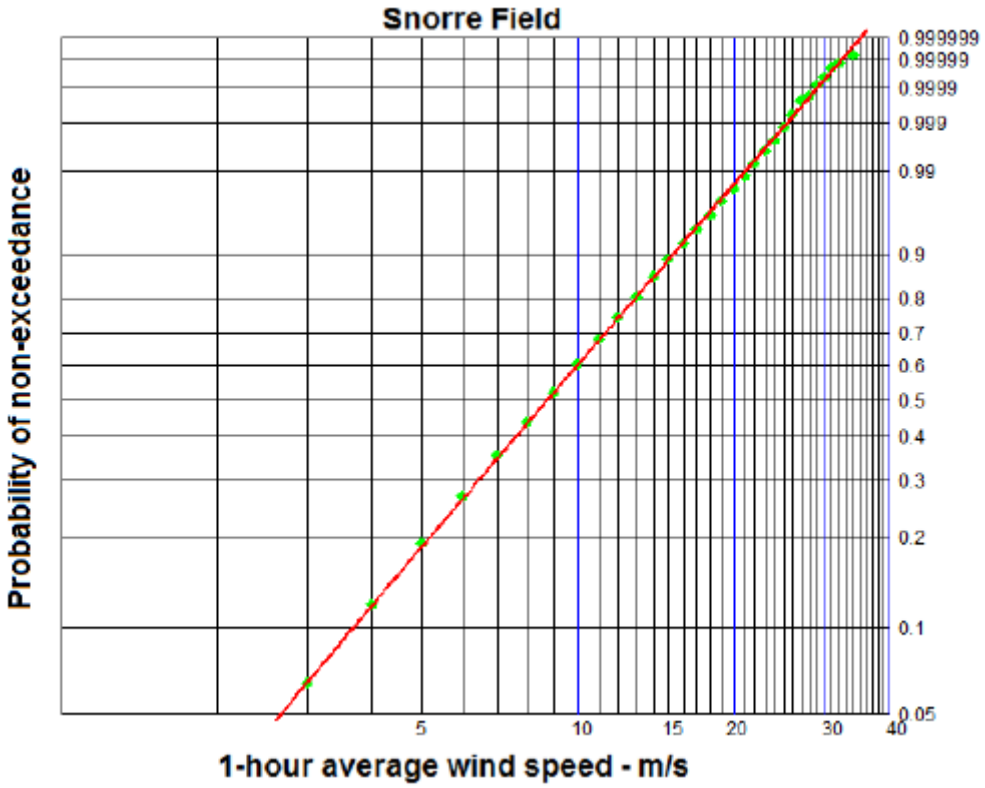

Figure A.1: Distribution of 1-hour mean wind speed at Snorre field, Equinor (2016).

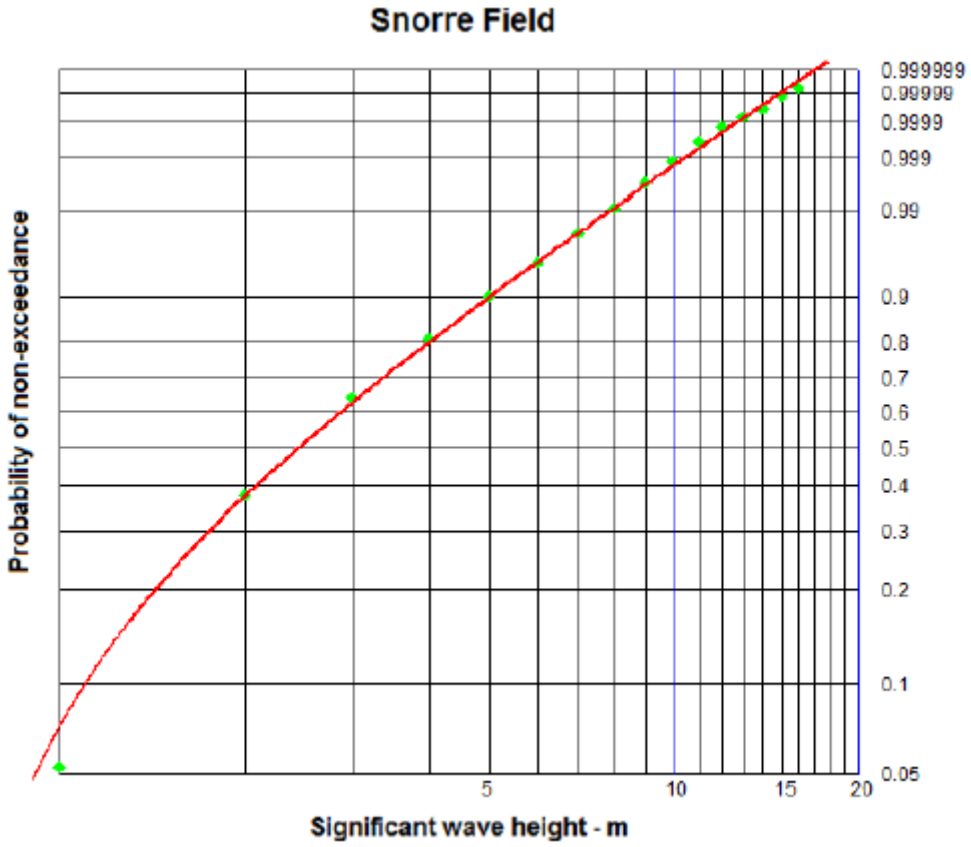

Figure A.2: Distribution of significant wave height at Snorre field, Equinor (2016).

Appendix B

Time domain simulation results

B.1 CPC-BW

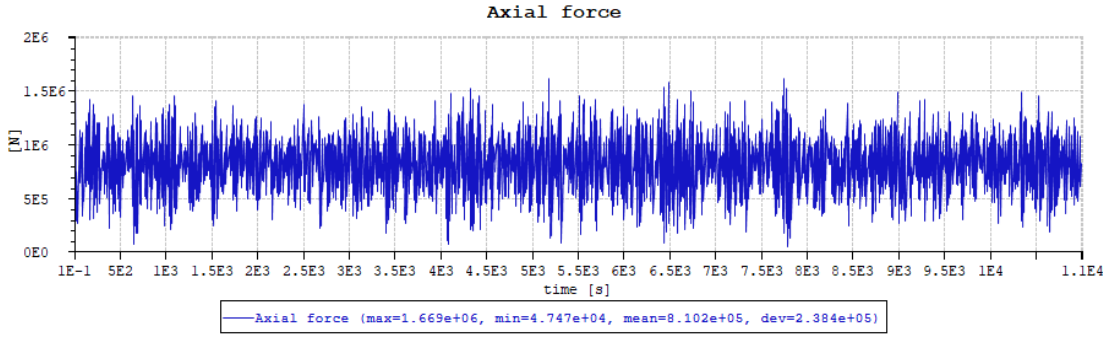

Figure B.1: Time series of the leeward mooring line tension at the anchor for the CPC-BW system in regime III.

Appendix C

Power and line force spectrum's

C.1 CWC

C.1.1 Regime I

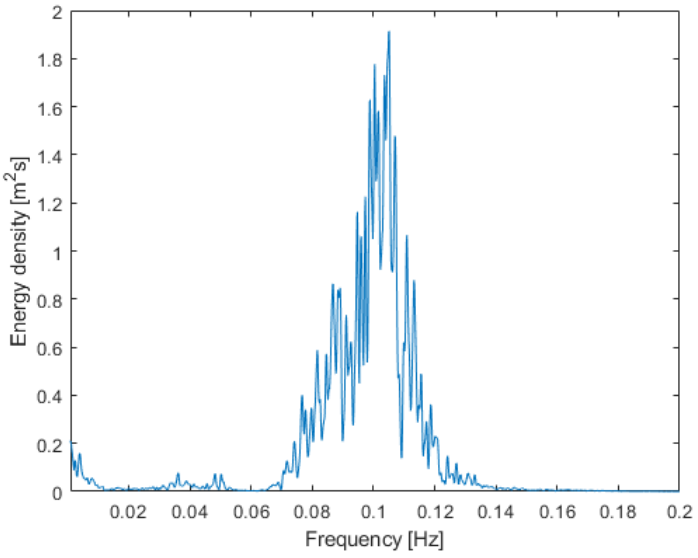

Figure C.1: Power spectrum of heave motion for CWC system in regime I.

C.1.2 Regime II

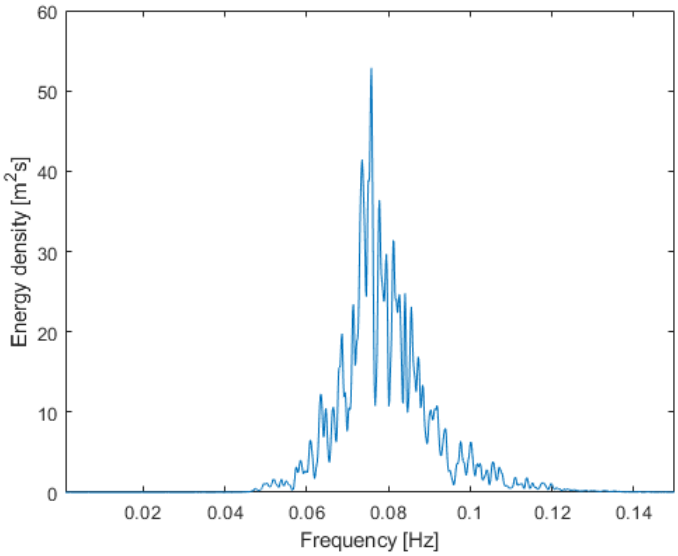

Figure C.2: Power spectrum of heave motion for CWC system in regime II.

C.2 CPC-T

C.2.1 Regime III

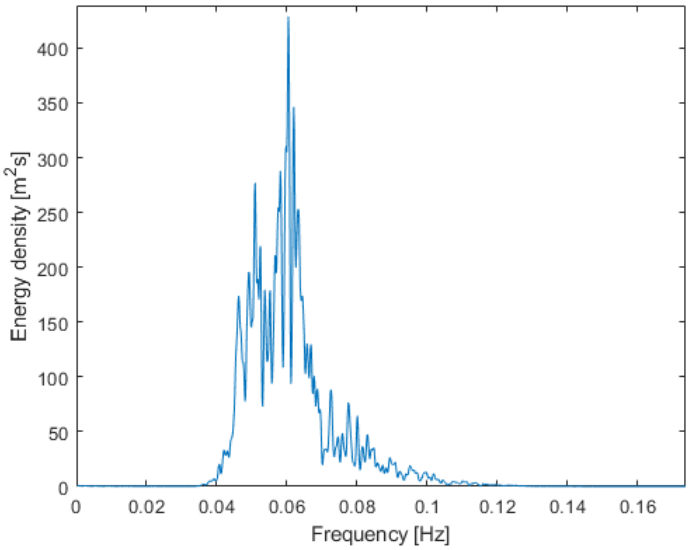

Figure C.3: Power spectrum of heave motion for CPC-T system in regime III.

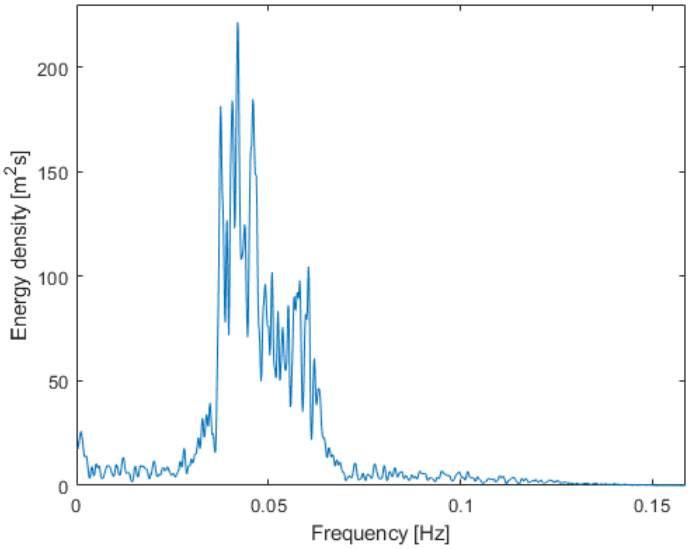

Figure C.4: Power spectrum of pitch motion for CPC-T system in regime III.

C.3 CPC-BW

C.3.1 Regime III

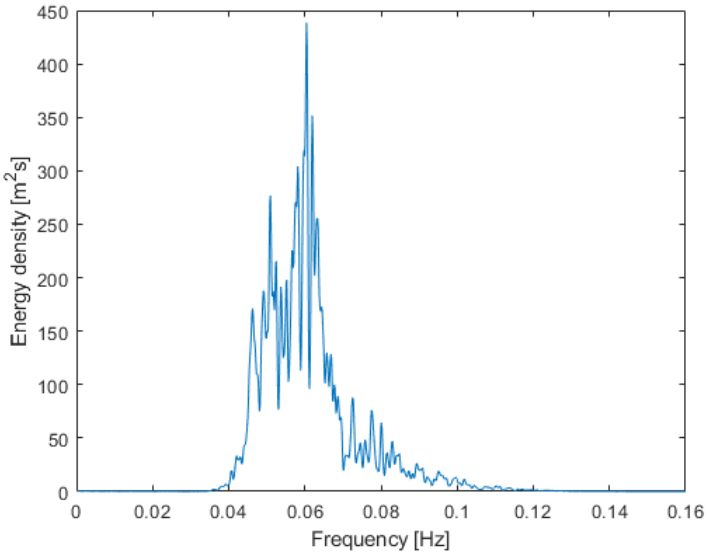

Figure C.5: Power spectrum of heave motion for CPC-BW system in regime III.

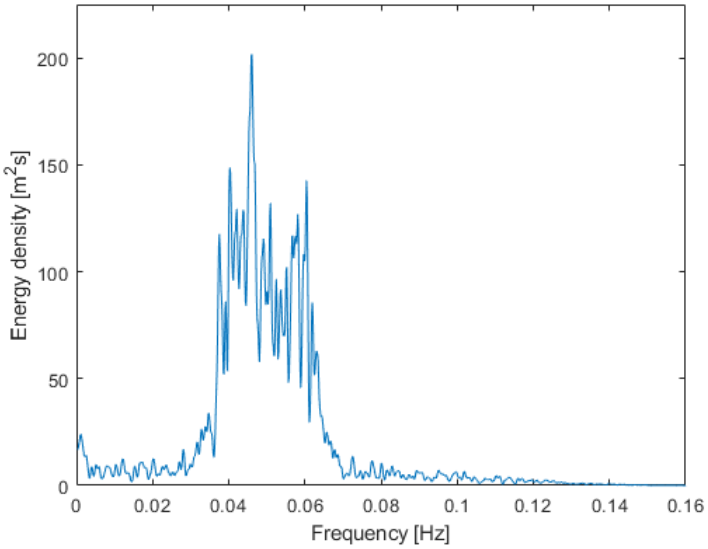

Figure C.6: Power spectrum of pitch motion for CPC-BW system in regime III.

C.4 CPC-BW-NL

C.4.1 Regime III

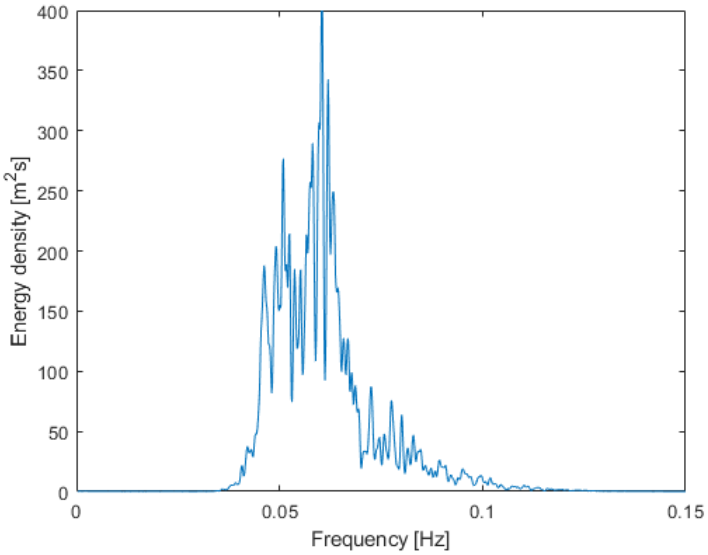

Figure C.7: Power spectrum of heave motion for CPC-BW-NL system in regime III.

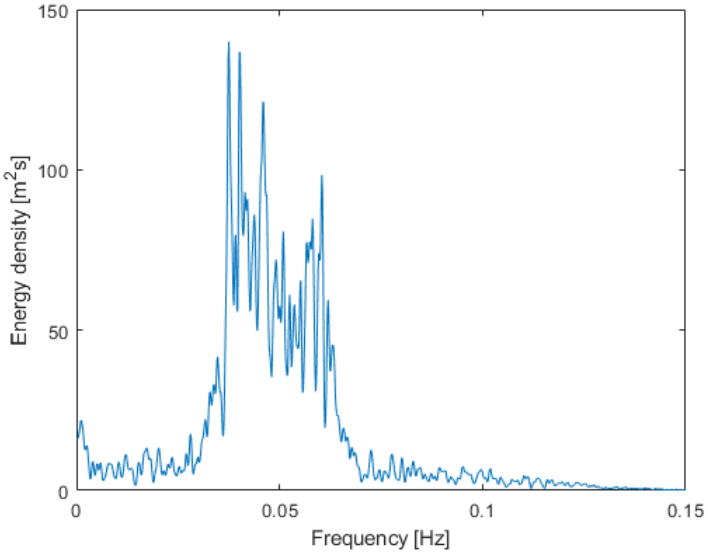

Figure C.8: Power spectrum of pitch motion for CPC-BW-NL system in regime III.

C.5 CNC-5-T

C.5.1 Regime III

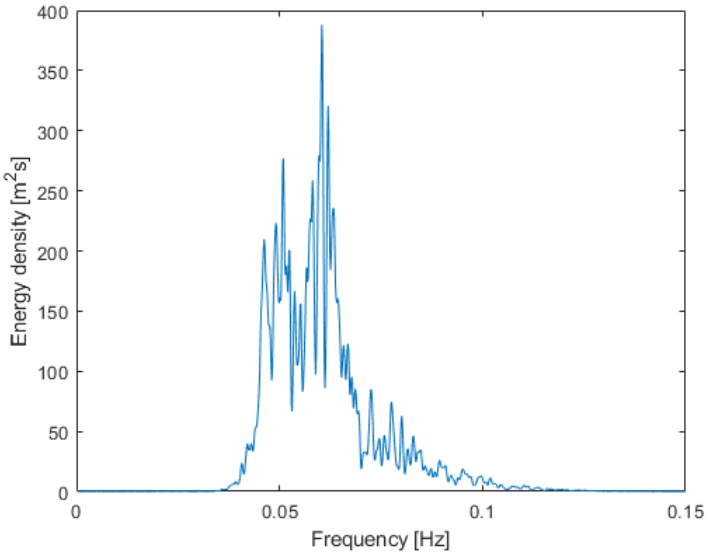

Figure C.9: Power spectrum of heave motion for CNC-5-T system in regime III.

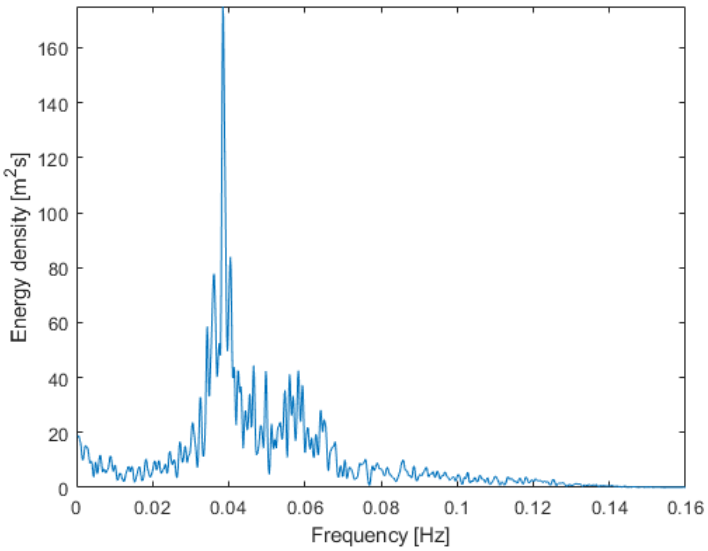

Figure C.10: Power spectrum of pitch motion for CNC-5-T system in regime III.

C.6 CNC-10-T

C.6.1 Regime III

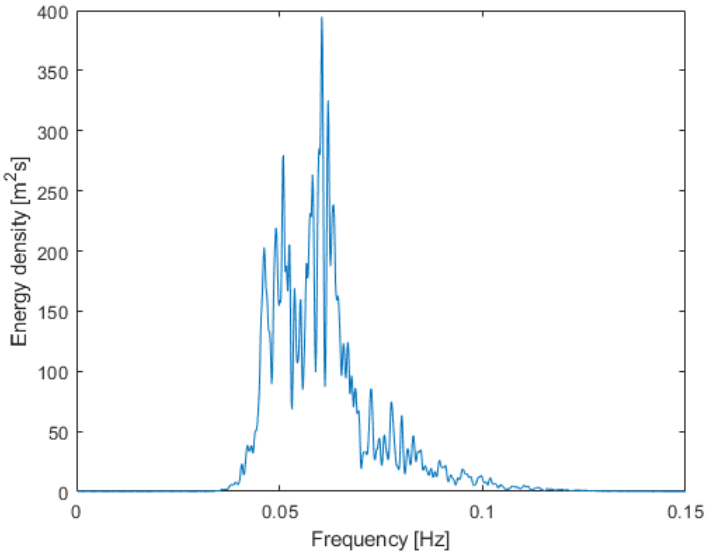

Figure C.11: Power spectrum of heave motion for CNC-10-T system in regime III.

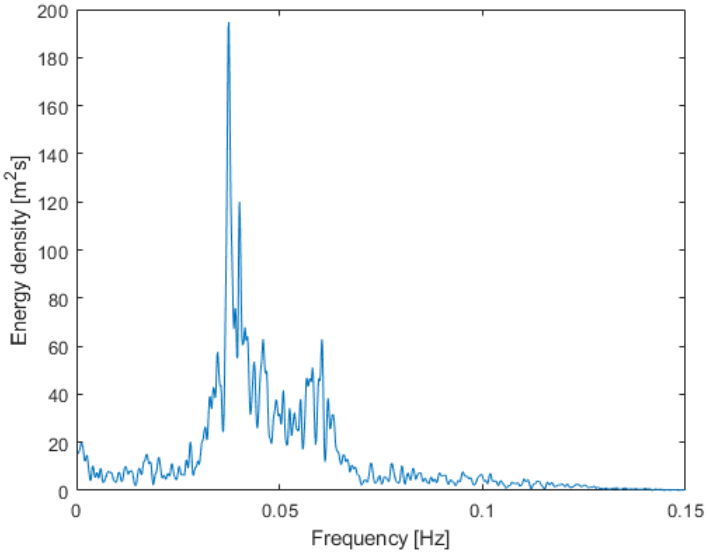

Figure C.12: Power spectrum of pitch motion for CNC-10-T system in regime III.

Appendix D

Material Properties

Superline Polyester (Permanent Mooring)

Nominal Diameter		MBL		Approximate Mass				Post installation Drift Stiffness		Intermediate Stiffness		Storm Stiffness	
				In Air		Submerged							
in	mm	kN	kips	kg/m	lbs/ft	kg/m	lb/ft	MN	10^3 kips	MN	10^3 kips	MN	10^3 kips
4 15/16	126	3924	882	10.0	6.7	2.5	1.7	51.0	11.5	105.9	23.8	109.9	24.7
5 1/2	139	4905	1102	12.1	8.1	3.0	2.0	63.8	14.3	132.4	29.8	137.3	30.9
5 15/16	151	6180	1389	14.4	9.7	3.6	2.4	80.3	18.1	166.9	37.5	173.0	38.9
6 1/4	158	6959	1565	15.9	10.7	4.0	2.7	90.5	20.3	187.9	42.3	194.9	43.8
6 5/8	168	7848	1764	18.0	12.1	4.5	3.0	102.0	22.9	211.9	47.6	219.7	49.4
6 15/16	177	8829	1984	19.9	13.4	5.0	3.4	114.8	25.8	238.4	53.6	247.2	55.6
7 1/4	185	9810	2205	21.9	14.7	5.5	3.7	127.5	28.7	264.9	59.5	274.7	61.7
7 15/16	201	10987	2469	25.8	17.3	6.5	4.3	142.8	32.1	296.6	66.7	307.6	69.1
8 3/8	213	12263	2756	28.9	19.4	7.2	4.9	159.4	35.8	331.1	74.4	343.4	77.2
8 3/4	223	13734	3086	31.8	21.4	8.0	5.4	178.5	40.1	370.8	83.3	384.6	86.4
9	229	14715	3307	33.6	22.6	8.4	5.7	191.3	43.0	397.3	89.3	412.0	92.6
9 1/2	241	15696	3527	37.2	25.0	9.3	6.3	204.0	45.9	423.8	95.2	439.5	98.8
9 3/4	247	16677	3748	39.2	26.3	9.8	6.6	216.8	48.7	450.3	101.2	467.0	104.9
10 1/8	257	17858	3968	42.4	28.5	10.6	7.1	232.2	51.6	482.2	107.1	500.0	111.1
10 3/8	263	18639	4189	44.4	29.8	11.1	7.5	242.3	54.5	503.3	113.1	521.9	117.3
10 9/16	268	19620	4409	46.4	31.2	11.6	7.8	255.1	57.3	529.7	119.0	549.4	123.5
10 13/16	274	20601	4630	48.5	32.6	12.1	8.2	267.8	60.2	556.2	125.0	576.8	129.6
11 1/16	281	21582	4850	50.7	34.1	12.7	8.5	280.6	63.1	582.7	131.0	604.3	135.8
11 1/4	286	22563	5071	52.6	35.3	13.2	8.8	293.3	65.9	609.2	136.9	631.8	142.0
11 7/16	291	23544	5291	54.7	36.8	13.7	9.2	306.1	68.8	635.7	142.9	659.2	148.1
11 5/8	296	24525	5512	56.7	38.1	14.2	9.5	318.8	71.7	662.2	148.8	686.7	154.3

Note: Tonnes = 1000kg Tons = 2000lbs
Figures shown are for guidance purposes only. For specific applications requirements please contact Bridon.

Figure D.1: Superline Polyester properties table developed by Bridon (2013).

Superline Nylon OCIMF 2000

Rope Diameter		Rope Circumference		Nominal Mass				Minimum breaking force (F min)					
				In Air		Submerged		New Dry			New Wet		
mm	in	mm	in	kg/m	lbs/ft	kg/m	lb/ft	kN	Tonnes	Tons	kN	Tonnes	Tons
80	3 1/8	251	10	4.2	2.8	0.41	0.27	1462	149	164	1344	137	151
88	3 4/8	277	11	5.2	3.5	0.50	0.34	1776	181	200	1628	166	183
96	3 6/8	302	12	6.1	4.1	0.59	0.40	2109	215	237	1942	198	218
104	4 1/8	327	13	7.0	4.7	0.68	0.45	2482	253	279	2276	232	256
112	4 3/8	352	14	8.3	5.6	0.80	0.54	2884	294	324	2649	270	298
120	4 3/4	377	15	9.5	6.4	0.92	0.62	3316	338	373	3041	310	342
128	5	402	16	10.4	7.0	1.00	0.68	3777	385	424	3463	353	389
136	5 3/8	427	17	11.7	7.9	1.13	0.76	4267	435	479	3914	399	440
144	5 5/8	452	18	13.2	8.9	1.27	0.86	4787	488	538	4395	448	494
152	6	478	19	14.6	9.8	1.41	0.95	5337	544	600	4905	500	551
160	6 2/8	503	20	16.2	10.9	1.56	1.05	5925	604	666	5435	554	611
168	6 5/8	528	21	17.8	12.0	1.72	1.16	6533	666	734	5994	611	674
176	6 7/8	553	22	19.8	13.3	1.91	1.28	7181	732	807	6592	672	741
184	7 2/8	578	23	22.2	14.9	2.14	1.44	7848	800	882	7210	735	810
192	7 4/8	603	24	24.1	16.2	2.33	1.56	8554	872	961	7858	801	883
200	7 7/8	628	25	26.1	17.5	2.52	1.69	9290	947	1044	8525	869	958
208	8 2/8	654	26	28.6	19.2	2.76	1.85	10055	1025	1130	9231	941	1037
216	8 4/8	679	27	30.5	20.5	2.94	1.98	10850	1106	1219	9957	1015	1119
224	8 7/8	704	28	32.5	21.8	3.14	2.10	11674	1190	1312	10722	1093	1205
232	9 1/8	729	29	35.4	23.8	3.42	2.30	12537	1278	1409	11507	1173	1293

Note: Tonnes = 1000kg Tons = 2000lbs
Figures shown are for guidance purposes only. For specific applications requirements please contact Bridon.

Figure D.2: Superline Nylon OCIMF 2000 properties table developed by Bridon (2013).

Emil Eikrem Rindarøy

Mooring Concepts for Floating Wind Turbines

NTNU
Norwegian University of
Science and Technology